

Measurement of D^* Meson with Two Jets in Photoproduction with the H1 Detector at HERA

Dissertation

zur Erlangung des Doktorgrades
des Fachbereichs Physik
der Universität Hamburg

vorgelegt von
ZLATKA STAYKOVA
aus Dobrich

Hamburg
2010

Gutachter der Dissertation:	Dr. Hannes Jung Prof. Dr. Johannes Haller
Gutachter der Disputation:	Dr. Hannes Jung Dr. Thomas Schörner-Sadenius
Datum der Disputation:	01.10.2010
Vorsitzender des Prüfungsausschusses:	Dr. Georg Steinbrück
Vorsitzender des Promotionsausschusses:	Prof. Dr. Joachim Bartels
MIN-Dekan der Fakultät:	Prof. Heinrich Graener
Leiter des Departments Physik:	Prof. Dr. Daniela Pfannkuche

Abstract

Photoproduction events containing a charmed meson $D^{*\pm}$ and two jets are investigated with the H1 detector using the HERA II data sample. The measurement is based on e^+p collisions during the period of 2006/2007 data taking and uses integrated luminosity of 113.14 pb^{-1} . The kinematic range of the measurement covers $100 \text{ GeV} < W_{\gamma p} < 285 \text{ GeV}$ for photon virtuality of $Q^2 < 2 \text{ GeV}^2$. The D^* mesons are reconstructed in the decay channel, $D^{*\pm} \rightarrow D^0\pi^\pm \rightarrow K^\mp\pi^\pm\pi^\pm$. Jets were reconstructed using the inclusive k_t algorithm and are selected if they have transverse momenta of $p_t(\text{jet}) > 3.5 \text{ GeV}$. One of the jets has to be associated with the D^* meson itself, such that the parent charmed quark can be tagged. The phase space of the measurement is limited within the central rapidity for the D^* meson and the D_{jet}^* , $|\eta| < 1.5$ while the second jet was measured within, $-1.5 < \eta < 2.9$. Single differential cross sections and double differential distributions were measured and compared to Leading Order Monte Carlo (MC) event generators, PYTHIA and CASCADE and with the Next-to-Leading order MC generator MC@NLO.

Kurzfassung

Die Messung in dieser Arbeit basiert auf Ereignissen, die ein $D^{*\pm}$ Meson und zwei Jets in Photoproduktion aufweisen. Es werden e^+p Kollisionsdaten analysiert, die mit dem H1 Detektor während der HERA II Phase in den Jahren 2006/2007 mit einer integrierten Luminosität von $113,14 \text{ pb}^{-1}$ aufgezeichnet wurden. Diese Analyse deckt den kinematischen Bereich $100 \text{ GeV} < W_{\gamma p} < 285 \text{ GeV}$ ab, wobei die Virtualität des Photons $Q^2 < 2 \text{ GeV}^2$ beträgt. Die D^* Mesonen werden im Zerfallskanal $D^{*\pm} \rightarrow D^0\pi^\pm \rightarrow K^\mp\pi^\pm\pi^\pm$ rekonstruiert. Die Jets wurden mit Hilfe des inklusiven k_t Algorithmus rekonstruiert und selektiert, falls ihr Transversalimpuls mindestens $p_t(\text{jet}) > 3.5 \text{ GeV}$ aufweist. Einer der beiden selektierten Jets sollte das D^* Meson tragen, um das ursprüngliche Charm Quark zu identifizieren. Der Phasenraum der Messung ist im Fall des D^* Mesons und seines assoziierten Jets D_{jet}^* auf den zentralen Rapiditätsbereich $|\eta| < 1.5$ beschränkt, während der zweite Jet im Bereich $-1.5 < \eta < 2.9$ gemessen wurde. In dieser Arbeit werden einfach differentielle Wirkungsquerschnitte sowie doppelt differentielle Verteilungen gemessen und mit Monte Carlo (MC) Generatoren in führender Ordnung, PYTHIA und CASCADE, sowie mit einem MC Generator höherer Ordnung, MC@NLO, verglichen.

“Deep in the fundamental heart of mind and Universe, said Slartibartfast, there is a reason.” Douglas Adams

To my family

Contents

Introduction	1
1 Theoretical Overview	3
1.1 Electron–Proton Scattering and Parton Model	3
1.1.1 DIS Kinematics	4
1.1.2 The Quark Parton Model	5
1.2 Quantum Chromodynamics	6
1.2.1 Running Strong Coupling and Parton Density Functions	6
1.2.2 Parton Evolution Models	9
1.2.3 Photoproduction	11
1.2.4 Heavy Quark Production	12
1.2.5 Hadronisation	13
1.2.6 Jet Production and Jet Algorithms	14
1.2.6.1 Cone Algorithms	14
1.2.6.2 Kt clustering algorithm	15
1.3 D^* and Jet Observables	16
1.4 Monte Carlo Event Generators	18
1.4.1 Leading Order Monte Carlo Event Generators (LO MC):	19
1.4.2 Monte Carlo at Next–to–leading Order– The MC@NLO:	20
1.4.3 Detector Simulation	21
2 The H1 Experiment at HERA	23
2.1 HERA	23
2.2 The H1 Detector	24
2.2.1 The Central Tracker	26
2.2.2 Calorimetry	29
2.2.3 The Luminosity System	31
2.2.4 The H1 Trigger	31
2.2.4.1 The Fast Track Trigger	34

3	Reconstruction and Selection of a D^* Meson	37
3.1	D^* meson properties	37
3.2	Reconstruction of D^* mesons	38
3.2.1	Selection of a D^* Candidate	38
3.2.2	Determination of the Number of Particles	40
4	Event Selection and Reconstruction	45
4.1	General Event Selection	45
4.2	Photoproduction Selection	45
4.3	Jet Selection and Reconstruction	46
4.4	Control Distributions	47
4.4.1	Reweighting the z -vertex distribution	48
4.4.2	Reweighting the $p_t(D^*)$ Distribution	49
4.4.3	Reweighting the $\Delta\varphi$ Distribution	49
4.4.4	Control Distributions	50
4.5	Purity and Detector resolution	56
4.5.1	Purity and Reconstruction Efficiency	58
4.5.2	Correlations and Detector Resolutions	59
5	Trigger Efficiency	65
5.1	Analysis Strategy	65
5.2	Trigger Efficiency Determination	68
5.2.1	Sub-trigger Definitions	69
5.2.2	Monitor Trigger Definitions	70
5.3	Trigger Efficiency Description	71
5.3.1	Reweighting in $\eta(D^*)$ for s53	74
6	Systematic Uncertainties	83
6.1	Uncorrelated Systematic Uncertainties	83
6.2	Correlated Systematic Uncertainties	85
6.3	Summary	87
7	Cross Section Determination and Results	91
7.1	$D^* + 2$ Jets Cross Section	91
7.2	Differential Cross Sections	92
7.3	Summary and Discussion	95
	Conclusions	103
	Bibliography	105

Introduction

In physics, scattering is the process when an object, a particle or a wave, is forced to deviate from its nominal trajectory. A typical daily example is when light is reflected from a flat surface. Scattering is one of the reasons why the human eye is able to see colours. A scattering is called *elastic* when the initial and final state of the process are the same objects, for example when a ball is reflected by the surface of a wall. In particle physics an early observation of a scattering process confirmed experimentally the existence of nucleus [1]. Later again in a scattering process, one of the fundamental particles in nature, the *proton* was discovered. Together with the neutrons and the electrons, they form the matter found in nature. From the early age the question what matter is formed from has been keeping the attention of the philosophers and scientists. For a long time these particles were considered to be *elementary*, meaning that they have no structure. Up to the present time, no evidence of an electron sub-structure has been found, supporting this assumption. Therefore, the electron is considered to be a point-like elementary particle, carrying electric charge and therefore interacting electro-magnetically. It belongs to a class of elementary particles called *leptons*¹. Conversely, the proton has a substructure which was first observed in scattering experiments. The proton consists of particles which have the general name *partons*. The partons that build most of the quantum numbers of the proton are called *valence quarks*. They are spin 1/2 particles carrying a fractional electric charge, and have a quantum number called *flavour-up, down, strange, charm, beauty and top*. A common way to test the structure of the proton is using the *Deep Inelastic Scattering* (DIS) process where a lepton is scattered off a parton in the proton with a very high energy transfer (normally referred to as Q^2) and the proton is dissociated.

The force that holds the quarks together in the proton is called the *Strong Interaction*. The strong interaction happens between objects carrying the charge of the field, *colour* and is mediated by the gauge bosons called *gluons* which also carry colour and thus may self interact. This fact has a deep consequence in the construction of the theory, such as a running strong coupling constant and the confinement of the partons². The theory that describes this interaction is called *Quantum Chromodynamics* (QCD). QCD can not be solved analytically,

¹The word comes from the Greek word $\lambda\epsilon\pi\tau\omicron\varsigma$ which means, *light, small*.

²The quarks and gluons are not observed as free particles, they are bounded in the hadrons.

but predictions can be made using perturbation theory. In this theory, an expansion series is performed in terms of the coupling of the QCD, the strong coupling $\alpha_S(Q^2)$. When the probing power Q^2 becomes small, then the coupling becomes large and the expansion series diverges. The charm quark with its mass of $m_c \sim 1.5 \text{ GeV}$ ³ provides a hard scale such that the strong coupling is small enough and perturbative QCD calculations are still reliable. This feature brings charm quarks and heavy quarks in general to the frontiers of the perturbative QCD theory. The fact that the gluon dominates charm production makes heavy quarks highly sensitive to the gluon content of the proton. For a full reconstruction of the hard partonic sub-process, jet algorithms can be applied. Jets are groups of highly collimated particles in the same direction and often are considered to reproduce the kinematics of the parent partons reasonably well. In this thesis a measurement of charm production in deep inelastic scattering is described.

At the DESY laboratory, Hamburg, Germany, the HERA electron-proton collider running at a centre-of-mass energy of $\sqrt{s} \approx 319 \text{ GeV}$ provided data to two general purpose detectors, H1 and ZEUS. Measurements of the photoproduction ($Q^2 \sim 0$) of D^* (composed of charm and down quarks) and jets with the H1 and ZEUS detectors [2, 3] have shown that the data are sensitive to different theoretical models which handle the higher order gluon radiation.

A measurement of D^* meson and two jets with the H1 detector will be presented in this work. Photoproduction events are analysed to obtain differential cross sections for D^* and two jets in a larger kinematic range with respect to a previous measurement at H1. Different quantities are defined and measured and finally compared to different models.

The thesis is organised as follows. In the first chapter a brief introduction to the theoretical aspects of QCD in general as well as heavy quark production and jet production are introduced. In section 1.4 the MC models used to compare the cross sections are introduced. In chapter 2 an overview of the experimental set up is provided. Chapter 3 describes the reconstruction technique and the selection criteria of the D^* meson. In chapter 4 the photoproduction event selection, jet selection and event reconstruction are described. In section 4.5 the detector response quantities are defined and discussed. In chapter 5 the trigger efficiency definitions and determination are discussed and in chapter 6 the systematic uncertainties considered in the measurement are presented. In chapter 7 the results of the measurement are shown and discussed.

³In this thesis the speed of light and the reduced Planck constant are $c = \hbar = 1$.

Chapter 1

Theoretical Overview

In this chapter the theoretical aspects of Quantum Chromodynamics (subsections 1.1.1–1.2.3), heavy quark (subsection 1.2.4) and jet production (subsection 1.2.6) are briefly introduced. The observables which are measured in the final differential cross sections are defined and described in section 1.3. The Monte Carlo models used in the thesis are described in section 1.4.

1.1 Electron–Proton Scattering and Parton Model

In Deep Inelastic Scattering (DIS) the interaction between the electron and proton is carried by the electroweak force. The mediators of the electroweak field are the neutral bosons, photons γ and Z^0 (in this case the interaction is labelled *neutral current* (NC)) and the charged bosons W^\pm (the interaction is labelled *charged current* (CC)). A Feynman diagram of the NC process is depicted in figure 1.1 (a). In the following some basic theoretical features of the NC DIS events will be described briefly.

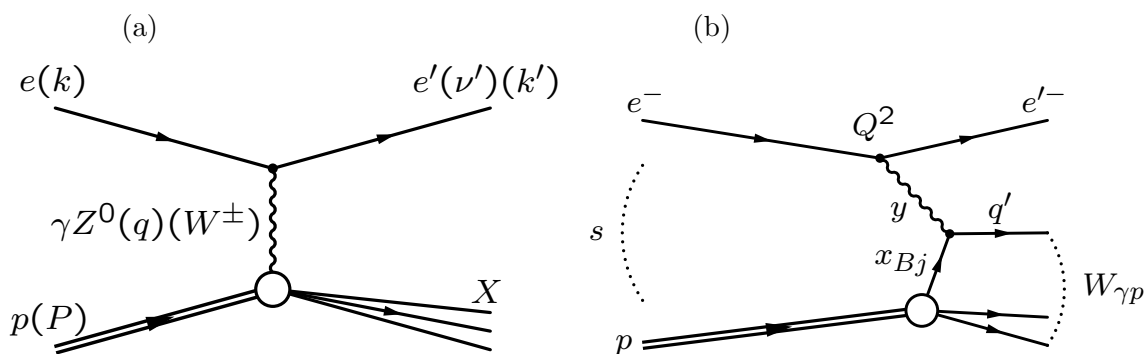


Figure 1.1: Feynman diagrams for a neutral current DIS event (a) and a QPM process where the kinematic variables are denoted.

1.1.1 DIS Kinematics

Using the four-vectors of the incoming $k = (E_e, \mathbf{k}_e)$, outgoing $k' = (E_{e'}, \mathbf{k}_{e'})$ electrons and the four vector of the incoming proton $P = (E_p, \mathbf{k}_p)$, four Lorentz invariant variables can be defined. They are usually used to describe the process and will be introduced in the following (see figure 1.1 (b)):

- $s = (k + P)^2$ is the centre-of-mass energy squared.
- The negative squared four-momentum transfer of the electron to the proton:

$$Q^2 \equiv -q^2 = -(k - k')^2 \quad (1.1)$$

where q is the four-momentum of the exchanged virtual boson. The squared momentum transfer may be considered as the invariant mass squared of the exchanged boson. It is often referred as the virtuality of the exchanged boson. If $Q^2 \ll 1000 \text{ GeV}^2$ processes with Z^0 and W^\pm exchange can be neglected due to their large masses ($M_W = 80.4 \text{ GeV}$, $M_Z = 91.2 \text{ GeV}$). Therefore contributions from Z^0 and W^\pm will be neglected in the following. When the virtuality of the exchanged boson becomes comparable with the proton mass m_p or smaller $Q^2 \lesssim m_p^2$, the photon is quasi real and the process is called *photoproduction*. The regime of low to medium virtuality $1 \text{ GeV}^2 \leq Q^2 \leq 100 \text{ GeV}^2$ is often called *low Q^2 DIS* process. When $Q^2 \gg m_p^2$ the process is called DIS and Q^2 is referred as a resolution power.

- The inelasticity y :

$$y = \frac{P \cdot q}{P \cdot k}. \quad (1.2)$$

At high centre-of-mass energies when the proton and electron masses can be neglected, it can be interpreted as the fractional energy loss of the electron as seen from the proton rest frame ($y = 1 - \frac{E'_e}{E_e}$). This quantity lies in the interval $(0, 1)$.

- The longitudinal momentum fraction of the proton carried by the struck quark, the Bjorken variable x_{Bj} :

$$x_{Bj} = \frac{Q^2}{2P \cdot k} \quad (1.3)$$

- The invariant mass of the photon-proton system:

$$W^2 = (P + q)^2. \quad (1.4)$$

Inelastic processes are classified with $W_{\gamma p}^2 \gg m_p^2$.

Neglecting the masses of the electron and proton these variables are related with:

$$Q^2 = xys \quad (1.5)$$

$$W^2 = ys - Q^2. \quad (1.6)$$

In the regime of photoproduction for the invariant mass of the hadronic¹ final state (HFS)² the last equation can be rewritten as $W^2 = y \cdot s$

At fixed values of the centre-of-mass energy, s any two of these variables, e.g the x_{Bj} and Q^2 , are independent and can be calculated from the kinematics of the scattered electron.

1.1.2 The Quark Parton Model

In the *quark parton model* (QPM) the proton consists of free partons. At large momentum transfer the virtual photon interacts with one of these partons. In a frame where the proton has a large momentum, such that the proton and partons masses can be neglected, *the infinite momentum frame*, each of the parton's momenta is $v = (\vec{v}_T, xP)$ where P is the proton momentum. In this frame the partons are considered as free particles. A very nice introduction to the theoretical aspects of QPM is given in [4].

The inclusive double differential cross section for $ep \rightarrow e' + X$ can be written as:

$$\frac{d\sigma(e^\pm p \rightarrow e^\pm X)}{dx dQ^2} = \frac{4\pi\alpha_{em}^2}{xQ^4} \cdot (xy^2 F_1(x, Q^2) + (1-y)F_2(x, Q^2)) \quad (1.7)$$

where α_{em} is the fine structure constant, and F_1 and F_2 are the structure functions of the proton. They can be parametrised in terms of *parton density functions* (PDF) $f(x, Q^2)$ as

$$F_2(x, Q^2) = x \sum_q e_q^2 (f_q(x, Q^2) + f_{\bar{q}}(x, Q^2))$$

where the e_q is the charge of the parton. The PDF can be interpreted as the probability to find a parton carrying fractional momentum of the proton's longitudinal momentum x at a given scale Q^2 . In QPM, the structure function is independent on the scale Q^2 , $F_i(x, Q^2) \approx F_i(x)$. This phenomena is known as the Bjorken scaling and states that the structure function depends only on the longitudinal momentum fraction of the parton regardless the scale Q^2 . Taking into account the 1/2 spin nature of the quarks and the fact that longitudinally polarised photons do not interact with spin 1/2 particles, the Gallan Gross relation validates:

$$F_2 = 2xF_1(x)$$

¹Hadrons is the general name of the baryons (three quark or anti-quark states) and the mesons (quark anti-quark bounded states). They are the particles in nature which interact strongly. The word comes from Greek and it means stout, thick.

²HFS objects are everything in the event except the scattered electron.

The structure function $F_2(Q^2, x)$ is measured from the reduced inclusive NC cross sections³. The H1 and ZEUS collaborations provided precise combined measurement of F_2 [5]. The reduced cross section can be seen in figure 1.2. The top graphics in the figure presents the reduced cross section as a function of x in different bins of Q^2 . On the lower plot the reduced cross section is shown as a function of Q^2 for different values of x . It can be seen that for relatively high values of x the reduced cross section is almost independent on the Q^2 which is the experimental prove of the Bjorken scaling.

The parton model encountered great success in early DIS experiments at small Q^2 and moderate values of x . At small values of x the structure function shows a dependency on the scale Q^2 (see the upper corner of the lower plot in figure 1.2), a phenomena known as *scaling violations*. It was shown experimentally that only half of the proton's momentum is carried by the quarks [6]. This leads to a need of improvement of the QPM definitions. The missing pieces are found to be the *gluons*, which leads to quantum chromodynamics.

1.2 Quantum Chromodynamics

Quantum Chromodynamics (QCD) is the theory describing the interactions between *colour charged* quarks exchanging *gluons*. It is the interaction holding the nucleons together in the atomic nucleus. The quarks are elementary particles with fractional electric charge carrying one type of colour: red, blue or green. Colour was introduced as a quantum number in order to explain the Δ^{++} and Ω^- baryons existence which consists of three up quarks (or three strange quarks for the Ω^- baryon) with the same spin and satisfying the Pauli principle for fermions. The coloured partons are combined in colourless hadrons. The symmetry group of the strong interactions is the non-Abelian $SU_c(3)$. This group has eight generators which leads to the existence of eight fundamental fields which couple with the quarks and can also change their colours. These fields are called *gluons*. As a direct consequence of the non commutativity of the symmetry group, the gluons carry also colour and therefore interact within each other. Coloured objects are not observed in nature. This phenomena is known as *colour confinement*.

1.2.1 Running Strong Coupling and Parton Density Functions

In addition to the loop diagrams which were already introduced in QED, where the photon splits into a quark-antiquark pair, in QCD the self interaction of the gluons leads to the existence of gluon loops. These loops lead to extra divergences. They are normally treated with a renormalisation procedure. Mathematically this is introducing an arbitrary scale μ_r which absorbs the divergency in the coupling. A common choice for μ_r is the largest virtuality in the process, in the case of high Q^2 DIS this it is the photon virtuality $\mu_r^2 = Q^2$. In the

³Neglecting the longitudinal structure function and contributions from Z^0 , $\sigma_r^{NC}(Q^2, x) \approx F_2(Q^2, x)$ for details see [5]

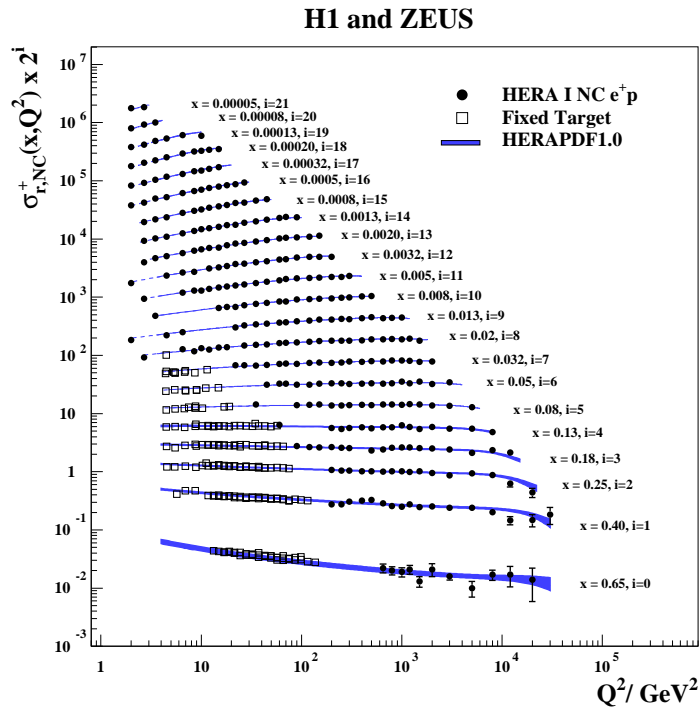
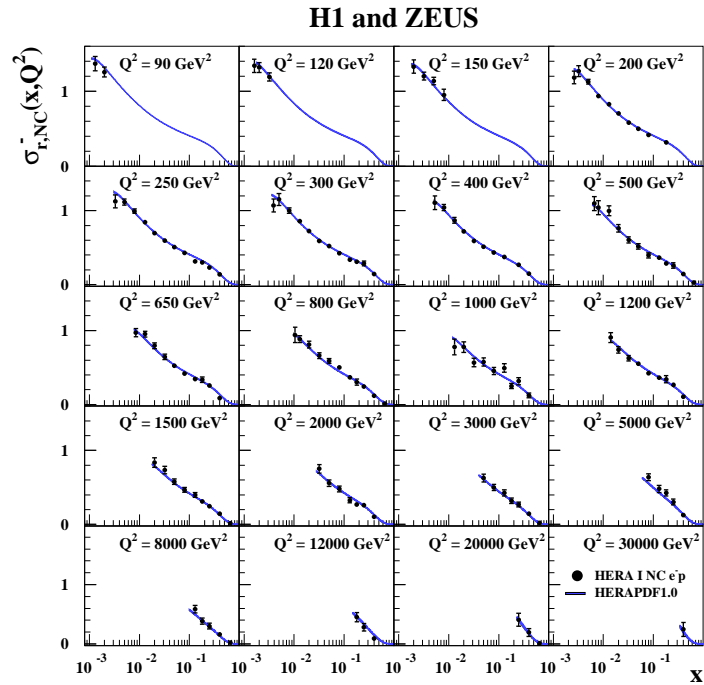


Figure 1.2: The reduced NC cross section. The figures were taken from [5].

case of photoproduction this is the transverse momentum square of the quark $\mu_r^2 = p_\perp^2$. The lowest order expression for α_s is:

$$\alpha_s(\mu^2) = \frac{12\pi}{(33 - n_f) \ln(\mu^2/\Lambda_{\text{QCD}}^2)} \quad (1.8)$$

where n_f is the number of active flavours and the constant Λ_{QCD} is the threshold of the perturbative calculation and was determined experimentally to be few 100 MeV. The strong coupling constant is decreasing with increasing the energy: $\lim_{Q^2 \rightarrow \text{inf}} \alpha_s(Q^2) = 0$. This feature leads to the phenomena known as *asymptotic freedom* [7]. This feature was nicely confirmed experimentally and results on precision measurements of α_s are shown by the H1 and ZEUS collaborations [8]. The running of the strong coupling can be seen in figure 1.4. An interpretation of the asymptotic freedom is that at large energies the quarks and gluons behave as semi-free particles.

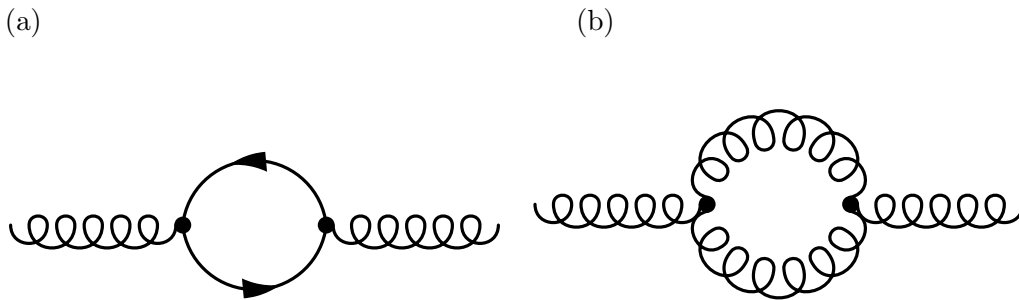


Figure 1.3: Fundamental QCD loops, fermion loop (a) and gluon loop (b).

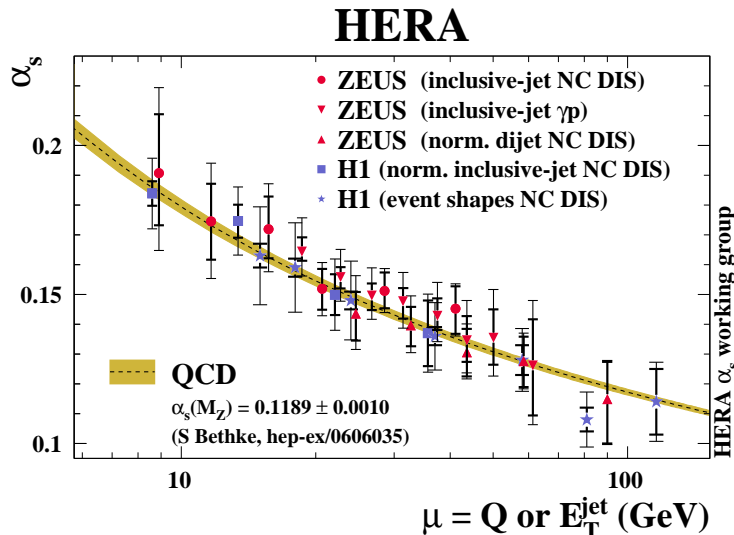


Figure 1.4: The running of the strong coupling as measured by the H1 experiment (blue markers) and ZEUS experiment (red markers). The figure was taken from [8].

In DIS the parton might emit soft gluons (scaling violations). These emissions of soft

gluons lead to divergence too. They are treated when introducing a cut of scale μ_f known as a factorisation scale. Below that scale the gluon emissions are absorbed into the parton density functions $f(x, \mu_f^2)$ and above that the perturbative calculations give reliable results. With analogy to the renormalisation scale, a common choice for the factorisation scale is the highest virtuality in the process— Q^2 for DIS and p_\perp for photoproduction.

According to the factorisation theorem [9] the total ep cross section can be written as a convolution of hard partonic cross section and soft non-perturbative parton density functions (PDF):

$$\sigma(ep \rightarrow eX) \sim f(x, \mu_f^2) \otimes \hat{\sigma}(s, \alpha_s(\mu_r), \mu_r, \mu_f) \quad (1.9)$$

where s is the centre-of-mass energy square, $f(x, \mu_f^2)$ are universal and independent on the process. $\hat{\sigma}$ is fully calculable according to the Feynman rules. The PDFs are not predicted by pQCD but their scale dependence can be calculated in QCD. Once the PDFs are known at a starting scale $f(x, \mu_0)$ they can be evolved up to the factorisation scale μ_f . The evolution of the PDFs includes processes like gluon radiation, gluon splitting and pair creation, which might happen more than once. A schematic picture of such gluon radiations and splittings is shown in figure 1.5 (a). The $f(x, \mu_0)$ is measured experimentally. Three models exist for the evolution and have the common name *evolution equations*. In the following they will be introduced briefly.

1.2.2 Parton Evolution Models

- **DGLAP**⁴ [10, 11, 12, 13]

The scale dependence of the PDFs is described by the following equations for the quark $f(x, \mu_f^2)$ and gluon $g(x, \mu_f^2)$ densities:

$$\frac{\partial f(x, \mu_f^2)}{\partial \mu_f^2} = \frac{\alpha_s(\mu_f^2)}{2\pi} \int_x^1 \frac{dz}{z} \left(P_{qq}(z) f\left(\frac{x}{z}, \mu_f^2\right) + P_{qg}(z) g\left(\frac{x}{z}, \mu_f^2\right) \right) \quad (1.10)$$

$$\frac{\partial g(x, \mu_f^2)}{\partial \mu_f^2} = \frac{\alpha_s(\mu_f^2)}{2\pi} \int_x^1 \frac{dz}{z} \left(P_{gq}(z) g\left(\frac{x}{z}, \mu_f^2\right) + P_{gg}(z) f\left(\frac{x}{z}, \mu_f^2\right) \right). \quad (1.11)$$

The P_{ab} are the DGLAP splitting functions and give the probability that a parton b with a longitudinal momentum x , emits a parton a carrying $(1-z)x$ fraction of b and continues with zx . The four DGLAP splitting functions are shown in figure 1.5 (b). In DGLAP the successive emitted partons are strongly ordered in terms of virtualities for the parton, where

⁴Dokshitzer, Gribov, Lipatov Altarelli and Parisi

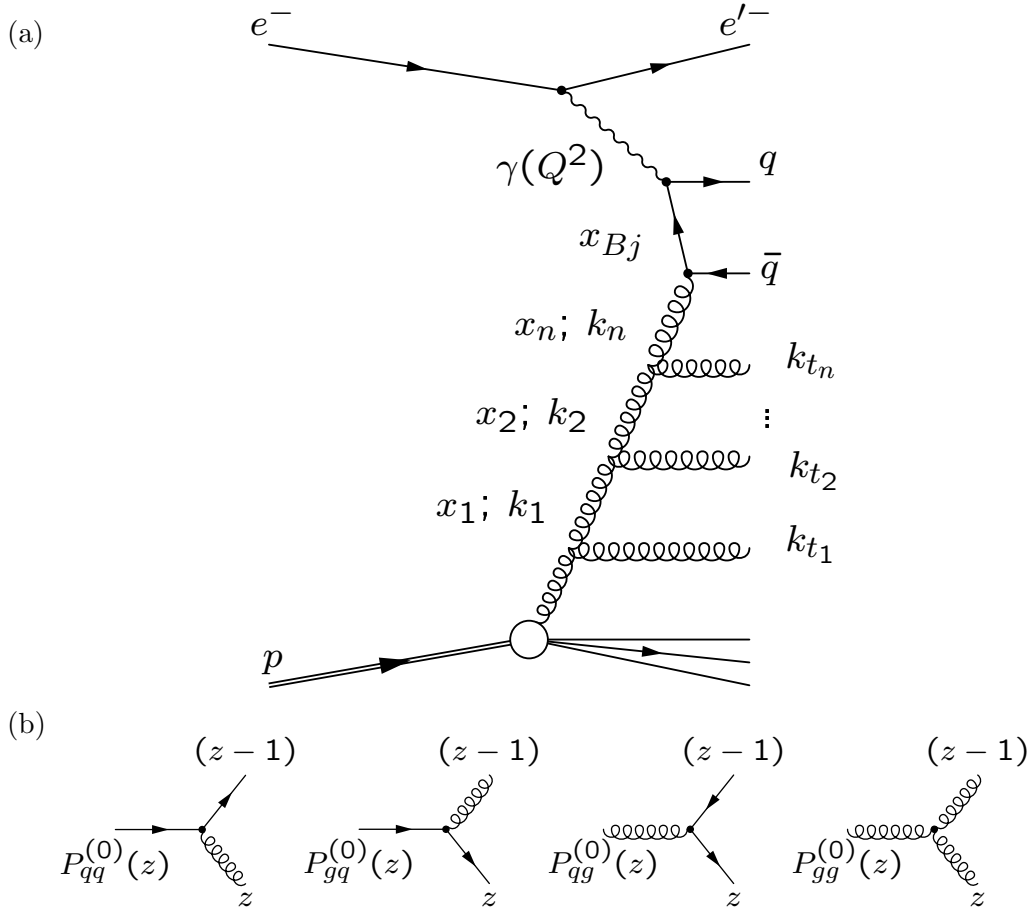


Figure 1.5: A Feynman diagram for gluon evolution (a). The virtualities and the longitudinal momentum fractions of the partons are indicated. The different DGLAP splitting functions (b).

$$\mu_0^2 \ll k_{t_1}^2 \ll \dots \ll k_{t_{n-1}}^2 \ll \mu_f^2$$

Here the choice of the factorisation scale μ_f^2 depends on the process. In the case of high Q^2 DIS this is the photon virtuality Q^2 ; and in the case of photoproduction the transverse momentum of the quarks in the hard partonic cross section. The calculation of the splitting functions and accordingly the hard cross section is done with on-shell partons⁵.

Since in this approximation the dependence of the PDFs on the virtualities of the partons is neglected, brings the name of the approximation, *collinear factorisation*.

The DGLAP approach predicts the scaling violations of F_2 down to very small values for x_{Bj} which is a great success for the model. However, at small values of x the gluon

⁵The virtualities of the partons are neglected.

splitting function is $P_{gg} \sim \frac{1}{z}$ which leads to a steep rise of the gluon densities. Although the structure functions are described perfectly by this approximation measurements of final states, e.g jets in large rapidity separation are not described [14, 15].

- **BFKL**⁶ [16, 17]

This approximation is valid only at small values of x and thus only gluon densities are taken into account. The ordering is performed in terms of x (figure 1.5):

$$x_0 \gg x_1 \gg \dots \gg x_{n-1} \gg x_n$$

The x_i values are limited below from the x_{Bj} . The parton density depends on the transverse momentum of the gluon $\mathcal{F}(x, k_t)$ and has the name *unintegrated parton density functions*, (uPDF). This leads to presence of a virtuality of the incoming gluon in the hard interaction, and thus the calculation is done off-shell. This ansatz has the name *k_t factorisation*.

- **CCFM**⁷ [18, 19, 20, 21]

The bridge between the DGLAP, applicable at high Q^2 and moderate values of x and BFKL, applicable for moderate values of Q^2 and small x is provided by the CCFM approximation. This ansatz can not be distinguished between DGLAP and BFKL in the appropriate corners of the phase space (see figure 1.6). Again only gluon densities are considered in this approximation and they also become dependent on the factorisation scale $\mathcal{A}(x, k_t^2, \mu_f^2)$. The successive ordering of the gluons is done in terms of radiation angle θ with respect to the longitudinal direction. The partons are treated off-shell in the calculation of the hard partonic cross section. In CCFM also k_t factorisation is applied.

1.2.3 Photoproduction

Events are classified as photoproduction events when the virtuality of the photon $Q^2 \approx 0$. The life time of the photon is directly related with the photon virtuality by $\tau_\gamma \sim 1/Q^2$ which means that the life time of these photons is significant. Therefore the electron beam can be considered as a source of quasi-real photons and the ep collision can be considered as γp collision. These photons are parameterised by the so called *photon flux* which is a function of the inelasticity and the virtuality of the photon $f(y, Q^2)$. The photon flux is calculated according to Weizsaecker-Williams Approximation [22, 23]. Another important consequence of the relatively long life-time of the photons in the regime of photoproduction is that the photon can fluctuate into a hadronic system and then interact with the proton.

⁶Balitsky, Fadin, Kuraev and Lipatov

⁷Catani, Ciafaloni, Fiorani and Marchesini

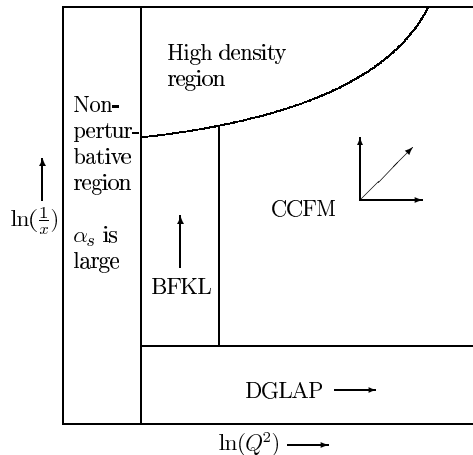


Figure 1.6: Applicable regions of the DGLAP, BFKL and CCFM evolution approaches.

These processes are called *resolved photoproduction*. When the photon interacts as a pointlike particle with the proton, the process is called *direct photoproduction*. In general the resolved photons can belong to two types, when they are bound in quark–anti quark state, so called *vector meson dominance model* [24, 25, 26] and *Anomalous photons* [27, 28] where the photon is not observed in a bound quark state.

The ep cross section is proportional to $1/Q^4$ therefore events with photoproduction dominate the total cross section. The first measurements using at H1 and ZEUS detectors at HERA were using photoproduction data samples [29, 30]

Similar to the proton, the photon has structure functions which are measured by different experiments, and the partons from the photon are also treated in terms of evolution equations [4, 31].

1.2.4 Heavy Quark Production

Heavy quarks are called those quarks which mass is above the parameter $m_Q > \Lambda_{\text{QCD}}$. These are the charm quark $m_c \approx 1.5 \text{ GeV}$, the beauty quark $m_b \approx 4.5 \text{ GeV}$ and the top quark $m_t \approx 170 \text{ GeV}$. Their mass can be used as a hard scale in the regime of photoproduction. This feature makes them highly interesting observables to test pQCD. The mass of the top quark is beyond the energy provided by the HERA collider and therefore in the following heavy quarks will mean both, charm and beauty quarks. The dominant production process for heavy quarks is the boson gluon fusion (BGF). The most important Feynman diagrams for heavy quark production are illustrated in figure 1.7.

There are in general two approaches for calculating heavy quark production and they are distinguished by the way the heavy quark is treated, massless or massive. These approaches will be briefly described in the following:

Massive approach: In this approach only light flavours and gluons are active in the

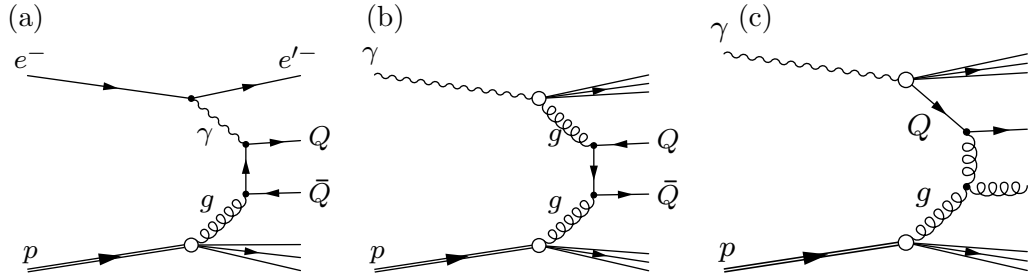


Figure 1.7: The most important Feynman diagrams for heavy quark production in ep interactions. Figure (a) illustrates direct photoproduction, (b) and (c) represent the resolved contribution. (b) is the hadron like, (c) is the charm excitation process.

proton or photon pdfs and the heavy quark PDFs vanish $f_Q(x, Q^2) = 0$. Heavy quarks are produced only in diagrams like in figure 1.7 (a) and (b). This approach is applicable for not too large p_t^c . For very large p_t , gluon emission and gluon splitting in the propagator becomes significant and this leads to divergences.

Massless approach: [32] In this approach the masses of the heavy quarks are neglected and they can be produced also from the photon or proton pdfs. In this approach processes like charm excitation (figure 1.7 (c)) are also included. As soon as the transverse momentum of the heavy quark approaches the quark mass, the calculations diverge and therefore this calculation is expected to work only at high transverse momenta.

1.2.5 Hadronisation

The process of transition between coloured partons to colourless hadrons is called *hadronisation*. This transition happens at a scale of ~ 1 GeV. At this scale the strong coupling is relatively large and no perturbative calculations can be applied. Instead phenomenological models are normally used. Here a brief description of the two models used in the presented study are introduced:

- **Lund String Model** [33, 34]:

The basic idea in the Lund string model, is that the quark-antiquark pairs are bound via one-dimensional coloured flux tubes called *strings*. The potential energy of the string increases with the distance linearly $F \propto r$. When the energy of the string is large enough to create a quark pair, the string "breaks". At the ends of the two strings new quark-anti quarks are created. On the other hand if the new pair has energy enough, it can split into another pair and so on. At the end, these quark anti-quark pairs are combined into hadrons according to fragmentation functions:

$$\mathcal{D}_q^h(z) = \frac{1}{z} (1-z)^a \exp(-bm_t^2/z)$$

where $m_t = m + p_x + p_y$ is the transverse mass of the parton and z is the longitudinal momentum fraction of the parton carried by the hadron. a and b are free parameters. For heavy quarks fragmentation the choice of parameters in the presented study was done according to the Bowler parametrisation [35].

- **Cluster Fragmentation** [36, 37]:

The cluster fragmentation uses the feature that the mass and spatial distributions of colour singlet quark anti-quark pairs have universal form. The colour singlet pairs are called clusters. The gluons at the end of the parton showers are forced to split into quark anti-quark pairs. The majority of clusters decay into two hadrons which in most of the cases is driven only by flavour conservation: $Cl(q_1\bar{q}_2) \rightarrow H_1 + H_2$, such that $H_1 = q_1\bar{x}$ and $H_2 = \bar{q}_2x$ where x and \bar{x} is a quark and a anti-quark. A nice introduction to the cluster fragmentation model is given in [38].

1.2.6 Jet Production and Jet Algorithms

Jets are called objects which in general are a flow or a group of particles collimated in the same direction. There is no unique definition of the term jet but it depends on the algorithm used to group the particles. In general there are two types of algorithms: clustering algorithms where the particles are grouped in transverse momentum and cone algorithms where particles are grouped in a cone around a high energetic particle. Jet algorithms also separated into exclusive and inclusive. Inclusive jet algorithms are those which include all particles in the final state in the content of a jet, while in the exclusive single particles might be not included necessarily in the content of a jet. A good jet algorithm is the one which produces kinematics close to the kinematics of the originating quark; they are required to be *infrared* and *collinear* safe⁸. In the following two examples of jet finding procedures will be introduced.

1.2.6.1 Cone Algorithms

The cone is with a predefined radius of R_0 in the $\eta - \varphi$ space. The choice of R_0 is normally defined by the direction of a highly energetic particle which is considered as a seed. Around that axis particles are added to the cone four vector until the cone axis doesn't change. The latter condition can be expressed with:

$$R(p_{i,cone}, v) = 0, \quad p_{i,cone} = \sum_i p_i \Theta(R_0 - R(p_i, v)) \quad (1.12)$$

where v is the four vector of the cone, R is the distance in $\eta - \varphi$ plane, $R = \sqrt{(\eta_i - \eta_v)^2 + (\phi_i - \phi_v)^2}$, Θ is the theta function. Normally a cut on the minimum en-

⁸Infrared safety avoids divergences due to soft gluon emissions and collinear safety is avoiding parton emissions with infinitely small angles. This means that the final jet four vector is not influent by such emissions.

ergy of the seed is applied. This makes the algorithm collinear unsafe. On the other hand when considering all particles as seeds, leads to infrared unsafety of the algorithm. Recently a new seedless infrared safe cone algorithm was introduced in [39]. The cone algorithms are normally preferred in pp collisions where the number of final state particles is a very large number which leads to slow convergence of the clustering algorithms.

1.2.6.2 Kt clustering algorithm

The k_{\perp} algorithm [40] combines proto-jets, if they are close enough in (η, ϕ) -space, the distances are defined with their transverse momenta p_t . The idea is that proto-jets which are close are joined and form new proto-jet.

The inclusive k_t algorithm can be applied in the following steps:

1. For each proto-jet i define:

$$d_i = p_{\perp}^2$$

and for each pairs of proto-jets :

$$d_{ij} = \min(E_{\perp,i}^2, E_{\perp,j}^2) \frac{(\eta_i - \eta_j)^2 + (\phi_i - \phi_j)^2}{R_0^2}$$

with R_0 being a parameter of the algorithm which is of the order of 1.

2. Find the smallest of all the d_i and d_{ij} and label it with d_{min}
3. If d_{min} is d_{ij} , then cluster proto-jets i and j are clustered into new proto-jet k , with the kinematic quantities:

$$\begin{aligned} p_{\perp,k} &= p_{\perp,i} + p_{\perp,j} \\ \eta_k &= \frac{p_{\perp,i} \cdot \eta_i + p_{\perp,j} \cdot \eta_j}{p_{\perp,k}} \\ \phi_k &= \frac{p_{\perp,i} \cdot \phi_i + p_{\perp,j} \cdot \phi_j}{p_{\perp,k}} \end{aligned}$$

4. If d_{min} is d_i , then the proto-jet i is removed from the list of proto-jets and is considered as jet.
5. The procedure continues until there are no proto-jets left in the list.

In the clustering algorithm the *recombination scheme* defines how particles are combined and how the new four vector is formed from the four vectors of the clustered particles. In short few of the recombination schemes will be listed. Details for the different schemes can be found in [41].

- In the E recombination scheme the particle four vectors are simply added. The resulting four vector of the jet is massive and has $E_{\perp,jet}^2 \neq p_{t,jet}^2$.
- The p_t scheme, transverse momenta are added, while the angles of the combined objects are varied: $\varphi_{new} = (p_t^1 \varphi^1 + p_t^2 \varphi^2)/(p_t^1 + p_t^2)$. The resulting jets are massless: $E_{jet}^2 = p_{jet}^2$

1.3 D^* and Jet Observables

The *charm quark* is the lightest among the heavy quarks and it was observed for the first time in 1974 [42, 43]. It decays mainly weakly to a muon and a muon neutrino or via the strong interaction to a charmed meson D^* . The reconstruction of D^* mesons is very widely used way to tag a charm quark in an event. Most often the reconstruction is done via the so called *Golden Decay Channel*. In this channel the final states are only three charged particles. This leads to a lot of advantages, for details please follow chapter 3.

In addition to the D^* , also jets can be selected since the jets are expected to inherit better the kinematic properties of the parent partons. The measurement of different observables constructed from the four vectors of the D^* meson (or the jet associated to the D^*) and the jets in the event (or the other jets) give important information on the production mechanism of the heavy quarks. Tagging the second charm quark encounters statistical limitations because of the small branching fraction of the chosen channel (see chapter 3). Instead a more inclusive approach could be used. The second hard parton in the event is tagged by the presence of a jet. Such way the full kinematics of the hard parton pair (quark in the case of BGF process and gluon in the case of charm excitation see figures 1.7 (a) and (c)) might be reconstructed. In order to ensure that the D^* and the jet originate from different partons, the D_{jet}^* is also identified (see section 4.3). Using the kinematics of the D_{jet}^* and the second hardest jet in the event the following quantities can be defined. The definitions of the different observables and their interpretation will be described briefly:

- **The azimuthal angular difference between the jets $\Delta\varphi$**

The angular separation between the jets in the transverse plane $\Delta\varphi$ is sensitive to higher order parton emissions. If the jets are balanced in p_t , they are well separated in the transverse plane and the angular difference between them is close to 180° (see figure 1.8). In this case higher harder parton radiation is not likely. As soon as a third hard parton occurs also in the partonic ladder, the incoming gluon has transverse momentum and smaller $\Delta\varphi$ values are possible. This variable is defined with the following formula:

$$\Delta\varphi = |\varphi(D_{jet}^*) - \varphi(\text{Other jet})| \quad (1.13)$$

- **The average transverse momentum of the di-jet pair p_t^{jj}**

Similar to the azimuthal angle difference $\Delta\varphi$ the average transverse momentum of the

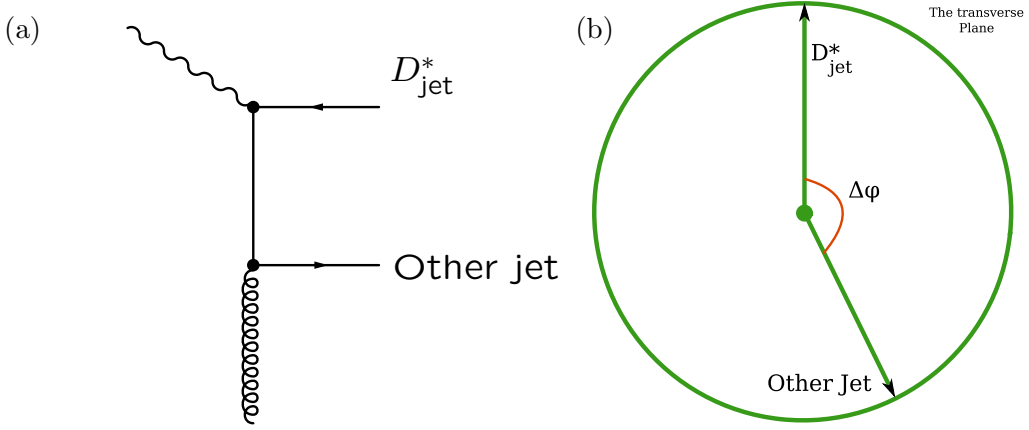


Figure 1.8: A Feynman diagram production of the D_{jet}^* and the Other jet (a). The transverse plane and the azimuthal angle difference between the D_{jet}^* and the Other jet (b).

di-jet pair, p_t^{jj} is sensitive to the kinematics of the incoming gluon or to higher parton emissions. If the pair is balanced in transverse momentum then $p_t^{\text{jj}} \approx 0$. If further parton emission occurs or the incoming gluon has a transverse momentum then $p_t^{\text{jj}} > 0$. It is reconstructed using the formula:

$$p_t^{\text{jj}} = V_t, V = (v_1 + v_2) \quad (1.14)$$

where $v_{1/2}$ are the four-vectors of the jets.

- **The longitudinal momentum fraction of the photon carried by the jets x_γ**

This quantity is used to separate direct and resolved processes. It is defined as:

$$x_\gamma = \frac{E_t^1 \exp(-y_1) + E_t^2 \exp(-y_2)}{2E_\gamma} \quad (1.15)$$

where $E_t^{1,2}$ and $y^{1,2}$ are the transverse energies and rapidities of the outgoing partons. E_γ is the photon energy where for photoproduction events it is directly related to the beam energy and the inelasticity according to:

$$E_\gamma = yE_e. \quad (1.16)$$

Using momentum conservation one obtains (for details see [44]):

$$x_\gamma = \frac{\sum_{i=1,2} (E_i - p_z^i)}{2yE_e} \quad (1.17)$$

where E_i, p_z^i are the energy and z components of the jet four vectors. Direct processes are events where most of the photon energy is carried by the jets, i.e $x_\gamma \geq 0.75$. Resolved processes are considered when a small fraction of the photon energy is taken by the jets,

i.e $x_\gamma < 0.75$

- **The invariant mass of the remnant M_X**

The remnant mass M_X is defined as:

$$M_X^2 = (P + q - (v_1 + v_2))^2 \quad (1.18)$$

where P is the four vector of the initial proton, q is the four vector of the photon, and $v_{1,2}$ are the four vectors of the jets. The kinematics of the photon were reconstructed using the relation (1.16): $v_\gamma = (yE_e, 0, 0, -yE_e)$. For events where the jets carry most of the initial energy, (the proton and photon energies) M_X would be small. For events where further partons are radiated from the proton or the photon side, the M_X is shifted towards large values [45] (see figure 1.9) and carries information on the full kinematics of the incoming parton. By definition this quantity lies in the interval $(0, W_{\gamma p})$.

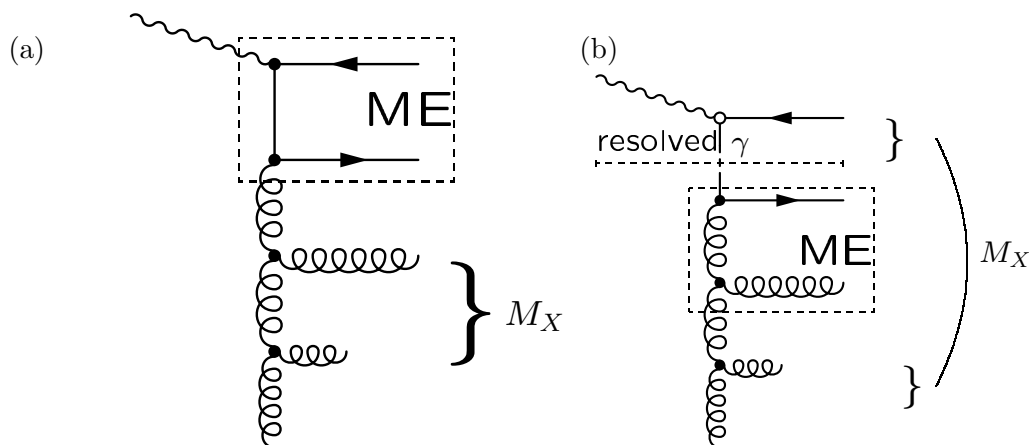


Figure 1.9: The invariant mass of the remnant M_X in the case of direct photo production (a) and resolved photon case (b).

1.4 Monte Carlo Event Generators

Event generators are computer programs which simulate high-energetic collisions between particles, in particular ep deep inelastic scattering process. They use the Monte Carlo (MC) technique for solving unsolvable analytically differential or integral equations. At the end they provide QCD calculations which can be directly compared to a measurement. Moreover, the output of the programs can be fed in a detector simulation programs and such way detector effects can be studied. A nice introduction to MC technique and principles is given in [46]. In the following section a brief introduction to the MC programs used for this measurement will be introduced.

An illustration of the basic phases in a MC generator is shown in figure 1.10. The event

generation starts with the calculation of the matrix elements (ME) for the current process. After that the initial state parton showers (ISPS) which are done according to the schemes described in subsection 1.2.2 and the final state parton showers (FSPS) are applied. At the end the partons are transformed into hadrons according to different hadronisation models. In this work several MC generators were used in the following they will be introduced and their basic parameters will be given.

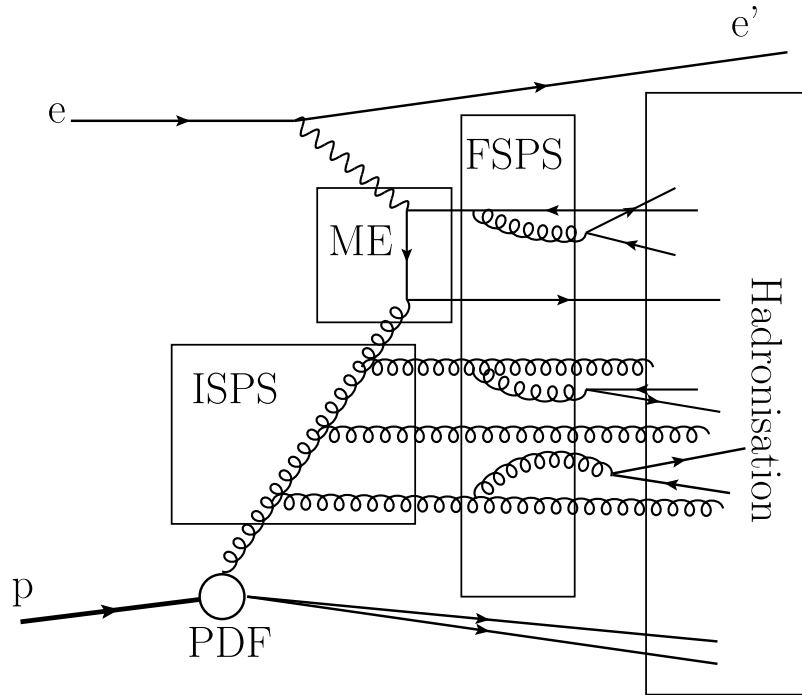


Figure 1.10: The different phases in used in a MC generator.

1.4.1 Leading Order Monte Carlo Event Generators (LO MC):

In this measurement two Leading Order Monte Carlo (LO MC) programs are used: PYTHIA 6.2 [47] and CASCADE [48, 49]. Both generators were used for estimating the detector response (see section 1.4.3) and at the end were compared to the data cross sections. The two models use the Lund string model for the hadronisation phase (discussed in 1.2.5). The heavy quarks fragment into heavy hadrons according to the Bowler parametrisation. The treatment of the final state parton showers in CASCADE was done as implemented in PYTHIA. The basic difference between the generators is in matrix elements calculation and in the initial state parton showers implementation.

The PYTHIA generator treats the parton showers according to the DGLAP evolution equations and calculates the matrix elements on-shell in the collinear factorisation ansatz. The renormalisation and factorisation scales were set $\mu_f^2 = \mu_r^2 = m_c^2 + \frac{(p_{t,c}^2 + p_{t,e}^2)}{2}$. The gener-

ator was ran in two modes, named in the following PYTHIA *massive* and PYTHIA *massless*. The basic difference between the two modes is that in the massive calculation two separate processes for heavy quark production, boson gluon fusion and charm excitation (figure 1.7 (a) and (c)) were generated. For the calculations of the ME for the BGF process were calculated with massive charm quarks while for the resolved component case the mass of the heavy quark was neglected. Afterwards the two samples were mixed according to the luminosity and the final cross section was obtained. Here the proton PDF were chosen to be the CTEQ6M NLO [50, 51] with photon PDF from SAS 2D LO [52]. This set of PYTHIA was used only for comparison to the cross section. In the second mode of PYTHIA, (PYTHIA *massless*) the generator was ran in a fully inclusive mode with massless quarks. Here the proton PDFs were chosen to be CTEQ6LO [50] and the GRVG-LO [53] photon PDFs.

In CASCADE the matrix elements are calculated off-shell applying k_t factorisation. The initial state parton showers are done according to the CCFM evolution equation where only gluons are considered. Only direct charm production is explicitly considered, but as shown in [54] some features of charm excitation process are implicitly taken into account. The uPDFs were chosen to be *set A0* [55]. The renormalisation scales was set to $\mu_r^2 = 4m_c^2 + p_t^2$. The factorisation scale is $\mu_f^2 = \hat{s} + Q_t^2$ where Q_t is the vectorial sum of the transverse momenta of the $c\bar{c}$ pair. \hat{s} stands for the invariant mass square of the pair.

For the three samples the charm and beauty masses were set to $m_c = 1.5 \text{ GeV}$ and $m_b = 4.75 \text{ GeV}$ and the threshold scale to $\Lambda_{QCD} = 0.25 \text{ GeV}$. The heavy quarks fragment according to the Bowler parameterisation.

Both, PYTHIA *massless* and CASCADE were used to correct the data to hadron level.

1.4.2 Monte Carlo at Next-to-leading Order– The MC@NLO:

The MC@NLO [56] is a full next-to-leading order matrix elements supplemented with parton showers. Details on the matching between the PS and the ME is given in [56].

The calculation of the matrix elements is done in the collinear factorisation ansatz, as implemented in the FMNR program [57]. A introduction to the program can be found in [58] and [59]. The parton showering is with angular ordering as implemented in the HERWIG [60] MC generator. The hadronisation of the final state quarks is done according to the cluster fragmentation procedure. In this calculation resolved photons are also taken into account using the GRV photon pdfs [53]. The proton PDFs were CTEQ6 [50]. The renormalisation and factorisation scales were chosen to be $\mu_r^2 = \mu_f^2 = \frac{m_t^2(Q) + m_t^2(\bar{Q})}{2}$ with $m_c = 1.5 \text{ GeV}$ and the transverse mass m_t is $m_t^2 = p_t^2(c) + m_c^2$. The uncertainty of the calculation was estimates when the two scales were varied with a factor of 2 up and down such that $0.5 < \frac{\mu_r}{\mu_f} < 2$ which results in 6 different sets of predictions. The upper and the lower predictions among these six samples were taken as uncertainty. The calculation was provided by [56].

1.4.3 Detector Simulation

The events produced by the MC event generators are passed through a full detector simulation. For simulating the detector response from the interactions between the particles and the detector material, a dedicated software program `h1sim` based on the GEANT program [61] is used. After that the signals are reconstructed into tracks, jets and etc with the same software program, `h1rec` which is used to reconstruct the data events. In that step many factors, like beam background conditions are taken into account according to the corresponding data taking period. This allows calculating detector efficiencies, acceptance etc and therefore the data can be corrected afterwards to *hadron level* (for detailed explanation for the correction procedures follow the sections 4.4, 4.5 and 7.1).

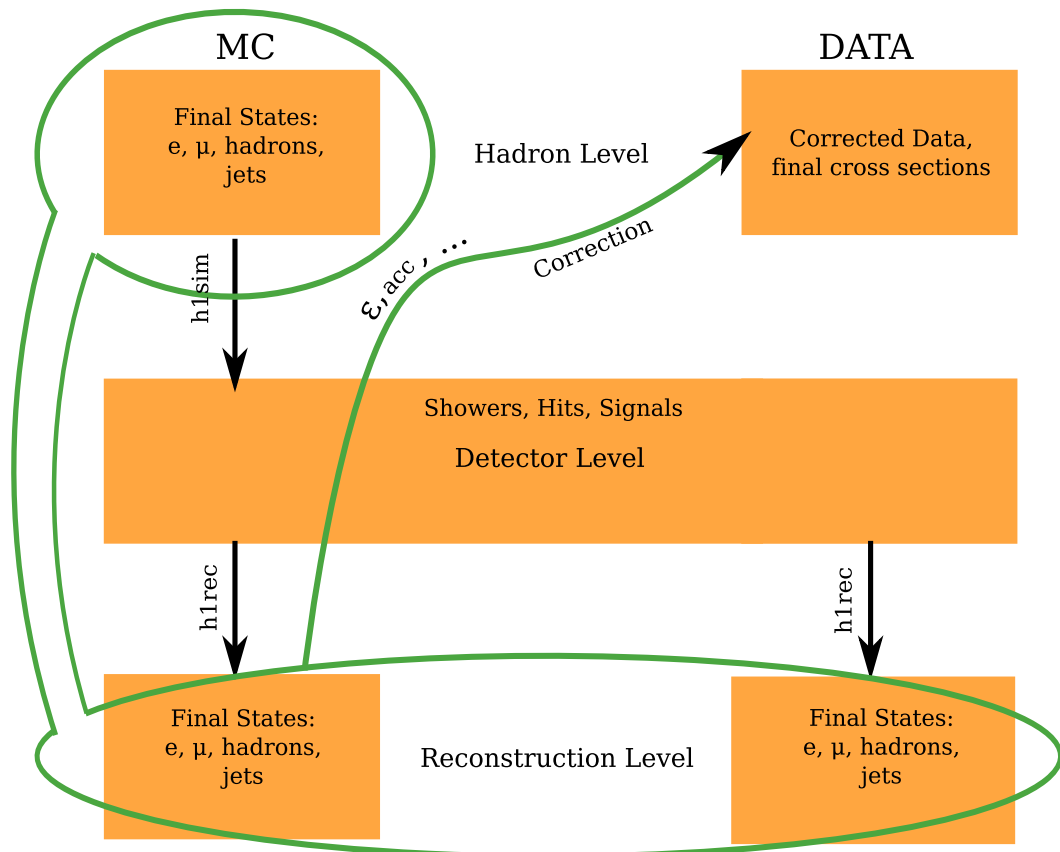


Figure 1.11: An illustration on the correction to hadron level data procedures with the help of MC event generator. Different stages of simulation and reconstruction are labelled.

Chapter 2

The H1 Experiment at HERA

2.1 HERA

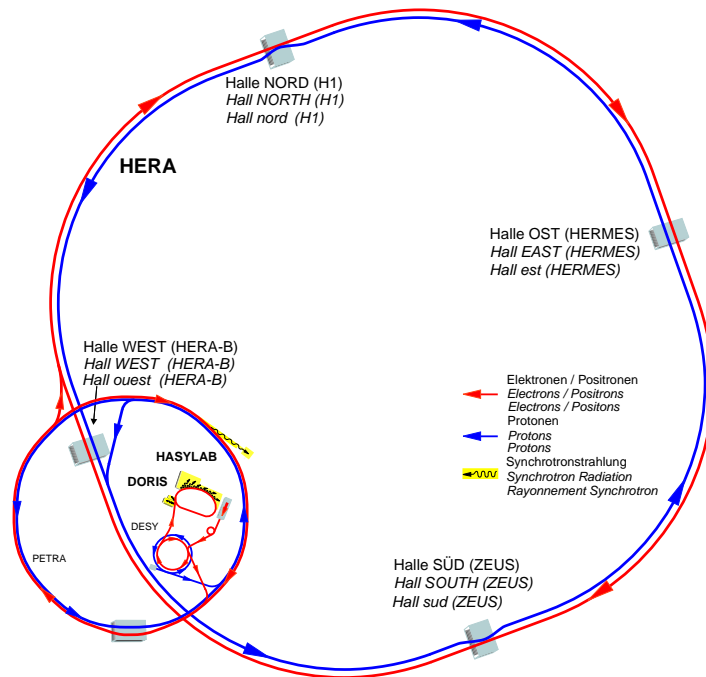


Figure 2.1: The HERA accelerator together with locations of the four experiments. Hall north– H1, hall east– HERMES, hall south– ZEUS and hall west– HERA–B. The red arrows or clockwise marks the direction of the electrons and blue arrows or anti–clockwise marks the direction of the protons.

The HERA accelerator [62, 63] was the only one worldwide providing colliding beams of electrons¹ and protons at high energies. It is located at the DESY laboratory, Hamburg, Germany and it operated in the years 1992–2007. The beams energies were 27.6 GeV and 920 GeV for the electrons and protons respectively. The beams collided in two interaction

¹And positrons too. In the following no difference in the current text is made if not mentioned explicitly.

points where the two detectors H1 [64] and ZEUS [65] were located. The H1 and ZEUS detectors were multipurpose detectors with almost full solid angle coverage of 4π . The two collider experiments study mainly the structure functions of the protons, jet production and α_s measurement, heavy quarks and diffraction. There were two fixed target experiments, HERMES [66] where beams of electrons collided with a gas target. The main focus of the research program of this experiment is the spin structure of the proton. The second fixed target experiment was the HERA-B experiment [67] where proton beams collided with wire target. The experiment had the purpose to study the CP violation in beauty production. A schematic picture of the accelerator together with the interaction points of the experiments is shown in figure 2.1.

The HERA collider had a circumference of ≈ 6.3 km long. It consisted of separate rings for electrons and for protons. The electrons and protons were pre-accelerated in the PETRA accelerator and injected in HERA with an energy of 12 GeV and 40 GeV, respectively. The beams consisted of 174 colliding bunches. The electron beam had a current of 50 mA while the proton beam 100 mA. The bunch crossing timing was 96 ns corresponding to 10.4 MHz bunch crossing rate. In addition there were also *pilot bunches* which had no colliding partner and were used for background studies. Until the end of the HERA operation a integrated luminosity of about 500 pb for each of the collider experiments was provided. In the year 2000 the accelerator was

upgraded for higher luminosity which defines two periods, HERA I and HERA II before and after the upgrade. In the last period of operation the proton energies were lowered to 460 GeV and 570 GeV, *low* and *medium* energy data taking periods. These data were used to study the longitudinal structure function of the proton [68]. Particularly the integrated luminosity for the three data taking periods of the H1 experiment is shown in figure 2.2.

2.2 The H1 Detector

The H1 detector [69] was about $12 \times 15 \times 10$ m big and had a weight of 2800 tons. The main purposes of the experiment were: precision measurements of the scattered electron; hadronic energy measurements and muon identification. The concept of the detector developed around

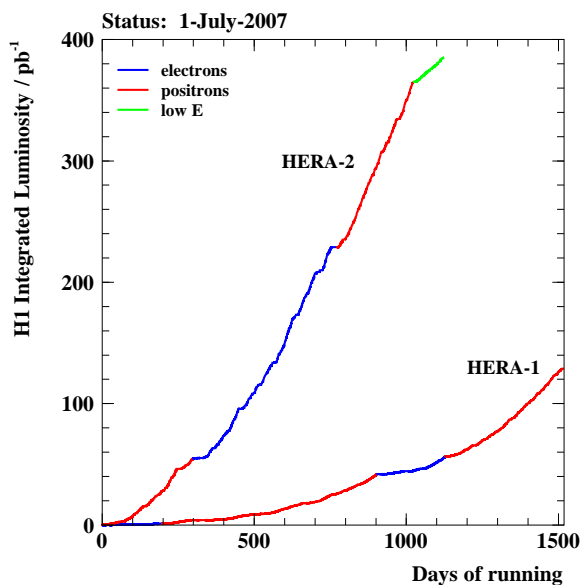


Figure 2.2: The H1 integrated luminosity as a function of time.

HERA Experiment H1

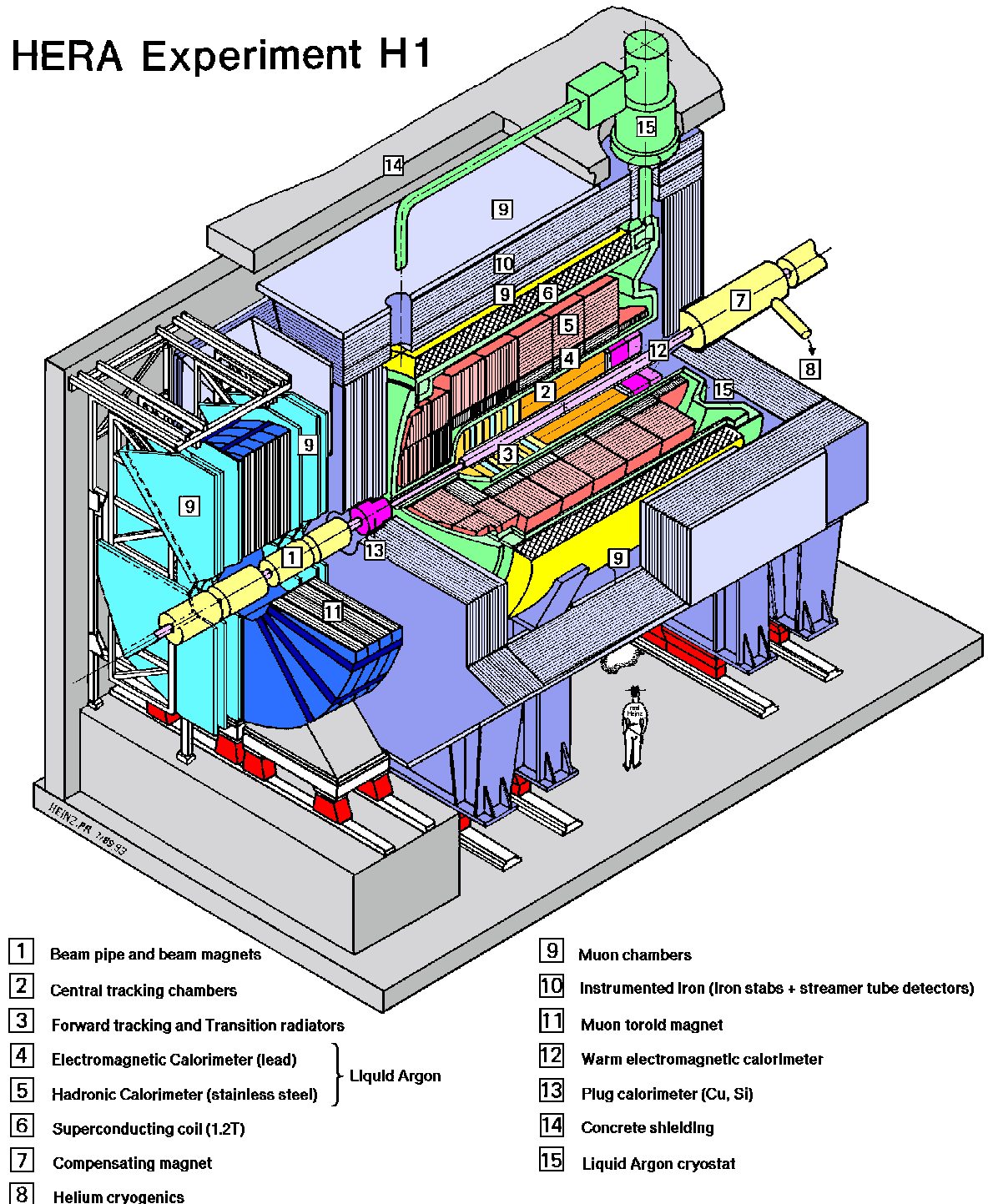


Figure 2.3: The H1 detector.

these three key points. A schematic view of the H1 detector is shown in figure 2.3. In the figure the main components of the detector are marked with numbers and in the following the most important ones will be described. The beam pipe (1) is surrounded by the tracking devices,

the central tracker (2) and the forward tracker (3). The trackers are surrounded by the Liquid Argon Calorimeter (LAr), which consists of an electromagnetic part (4) and hadronic part (5). The trackers and calorimeter are surrounded by a superconducting coil providing a 1.15T magnetic field (6). For the muon measurement, the muon chambers are used (9). Further improvement for the muon measurement and leaking energy of high energetic hadrons from the LAr is provided by the instrumented iron (10). Two additional calorimeters are located in the forward direction, the plug calorimeter (13) and in the backward direction, the SpaCal calorimeter (12).

The positive z direction of the H1 coordinate system is defined by the direction of the incoming proton². The x axis points to the centre of the accelerator and perpendicular to the ground surface pointing up is the y direction. The polar angle θ ³ is defined as the angle between the z axis and the origin of the trajectory of a particle. The azimuthal angle φ is defined in the transverse xy plane and is zero at the direction of the x axis.

2.2.1 The Central Tracker

For the presented measurement in this thesis a precise measurement of tracks is needed. Therefore the tracking system of the H1 detector will be described in details. It provides spatial information of the charged particles and triggering information. A detailed view of the tracking devices of H1 is shown in figure 2.4. Since this measurement is restricted to the central region only the components of the central tracking device (CTD) will be described. From the beam pipe to the outer region it consists of Central Silicon Tracker (CST), Central Inner Proportional (CIP) chamber, Central Jet Chamber 1 (CJC1), Central Outer z chamber (COZ), Central Jet Chamber (CJC2). The backward and forward silicon trackers and the forward tracking device provide improvement of the track reconstruction in the corresponding directions but they are not used in the current measurement.

- **The CJsCs [70]**

The CJC chambers are drift chambers with active length in the z direction of about 2.2 m. The angular coverage of the system is $20^\circ < \theta < 160^\circ$. Thirty cells with 24 wires each form the CJC1 while the CJC2 has sixty cells with 32 wires each.

When a charged particle traverses the volume of the CJC chambers it ionises the gas content of the chambers. The ion–electron pairs drift to the wires and by measuring the drift time reconstruction of single hits is achieved with a spatial resolution of $170 \mu\text{m}$ in the $r\varphi$ plane. The longitudinal resolution of the chambers is not so good (of about 22 mm), the z component of the track is measured with the charge division method. Finally the track uncertainty measurement was achieved to be $\sigma(p_t)/p_t \simeq 0.005p_t/\text{GeV} \oplus 0.015$ [71].

²The incoming proton direction also defines the forward direction.

³The polar angle of a particle is related to the *pseudo rapidity* $\eta = -\ln \tan(\theta)$ of a particle.

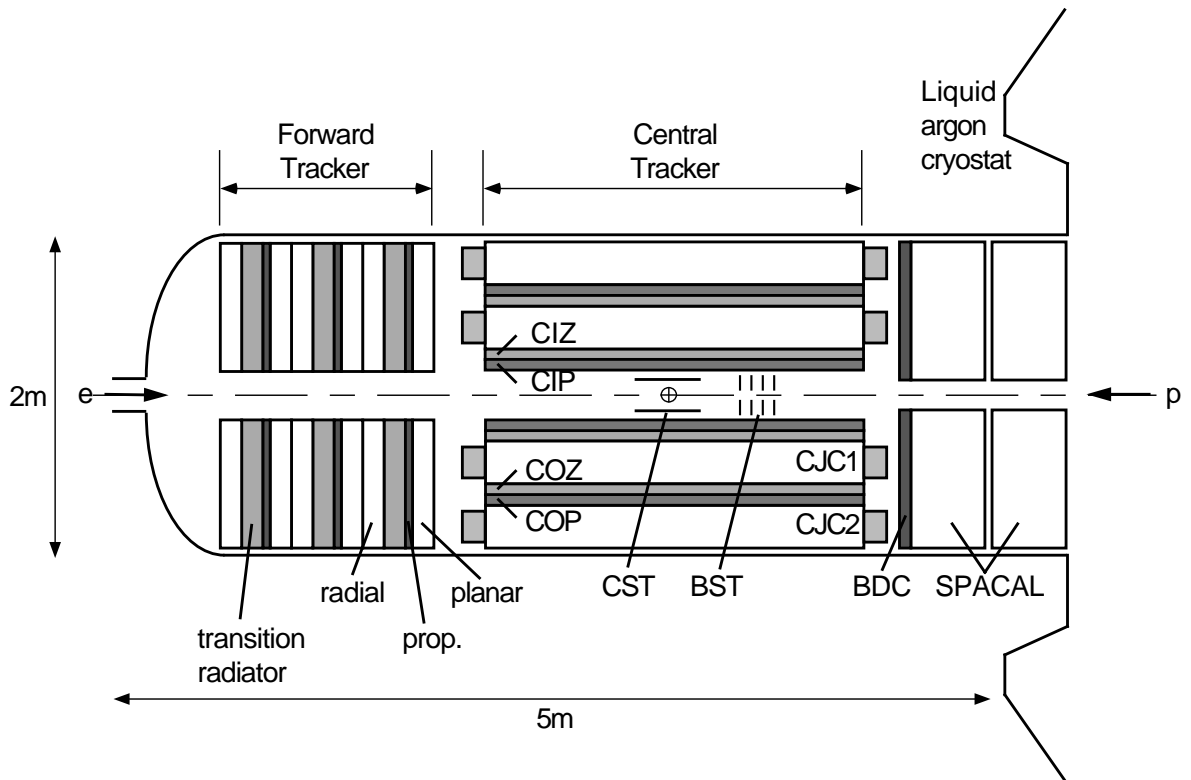


Figure 2.4: The tracking system of the H1 detector.

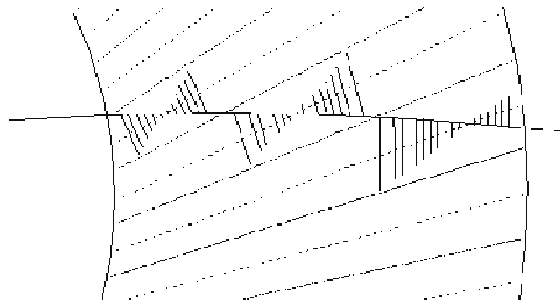


Figure 2.5: A track traversing the CJC2 volume. Hits and mirror hits are also shown.

Due to the magnetic field the charged particles curve. To compensate for this effect the cells are tilted by about 30° with respect to the radial direction. Such way the electrons drift perpendicular to the tracks. This leads to optimal track reconstruction. When reconstructing the hits, there is an ambiguity which side of the wire the hits occurred—left or right. This effect is called mirror tracks. Due to the tilt of the wires the mirror tracks do not occur in a neighbouring cell and therefore are easy to identify (see figure 2.5). Moreover tracks with high momentum ($p_t > 400 \text{ MeV}$) cross the sense wire's plane at least once in the CJC1 and CJC2, such way the time when the particle passed by the wire is shorter than 0.5 ns. This allows differentiating tracks from different bunch

crossings.

- **The CST** [72]

The vertex detector, the Central Silicon Tracker (CST) consists of two layers located around the beam pipe at a distance of 5 cm and 10 cm respectively. The two layers were 36 cm long which means $30^\circ < \theta < 150^\circ$ angular coverage. It provides precise information about charged particles originating from the interaction point and such helping the event vertex reconstruction. It also improves the spatial CJC resolution to about $40 \mu\text{m}$ for tracks pointing at the interaction vertex. Along the z axis the track are measured with a resolution of about $70 \mu\text{m}$.

- **The CIP** [73, 74]

The CIP is a multiwire proportional chamber with wires parallel to the beam pipe located between the CST and the CJC1 tracking devices. It is about 2 m long leading to an angular coverage of $11^\circ < \theta < 169^\circ$. It has 1.5 cm spatial resolution along the z axis. Due to its fast response of about 75 ns it provides triggering information with particular purpose of vertex reconstruction and can be used to distinguish proton induced background events.

- **The COZ**

Precise measurement of the tracks in the z direction is provided by the COZ drift chamber placed between the two CJC chambers. It has angular acceptance of $25^\circ < \theta < 155^\circ$. The wires are placed parallel to the beam pipe and provides a resolution along the z axis of about $350 \mu\text{m}$.

Some remarks on track reconstruction

The magnetic field along the z axis makes charged particles curve. A simplified picture of a track in the transverse plane is shown in figure 2.6 left. Five parameters define the trajectory of the track.

- The curvature of a track κ is related to the transverse momentum p_t of a track and the z component of the magnetic field:

$$p_t[\text{GeV}] = -Q[e] \cdot 0.3B_z[\text{B}] \cdot \frac{1}{\kappa[\text{m}^{-1}]}$$

where Q is the charge of the particle and B_z is the longitudinal component of the magnetic field.

- The distance of the closest approach d_{ca} is defined by the smallest distance between the track and the zero of the coordinate system in the transverse plane $r\varphi$ (see figure 2.6 (a)).

- The azimuthal angle φ is defined by the intersection of the tangent of the track at the d_{ca} and the x axis of the coordinate system (see figure 2.6 (a)).
- The polar angle θ between the intersection of the tangent and the z direction.
- The z_0 is the distance of the track at the d_{ca} and the z axis (see figure 2.6 (b)).

These parameters are obtained with a complicated fit procedure described in details in [75].

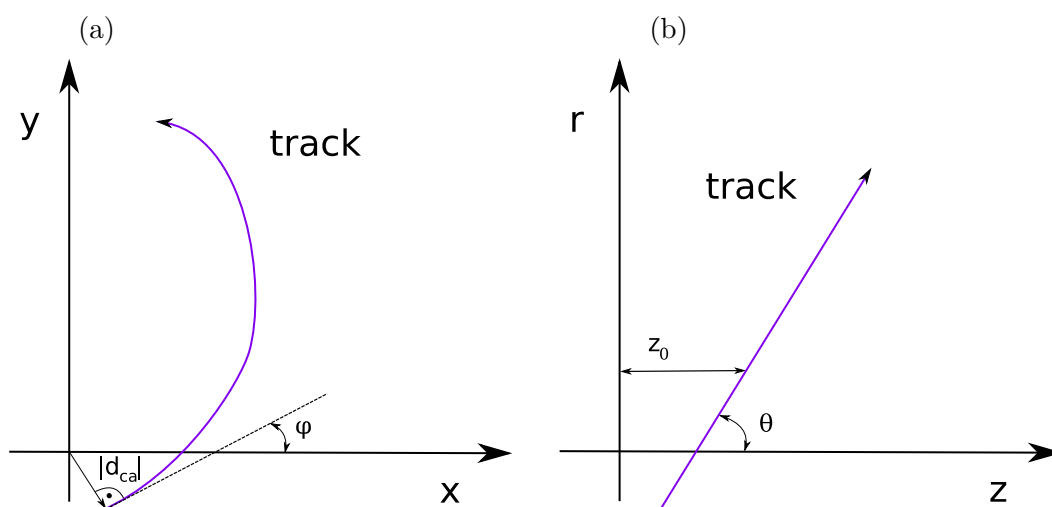


Figure 2.6: Projection of a track in the xy plane (left) and in the rz plane (right). Different track quantities are noted.

2.2.2 Calorimetry

For measuring the energy of the particles H1 has a complex calorimeter system. It has two main goals: precise energy measurement of the scattered electron at medium and high virtuality Q^2 ; precise measurement of charged and neutral hadrons for jet finding which is of particular interest for the current measurement. In photoproduction the scattered electron escapes the main detector volume and the calorimetry is used for a scattered electron veto. The components of the calorimeter used in this measurement are the Liquid Argon (LAr) calorimeter which is the main calorimeter of the detector and the backward Spaghetti Calorimeter (SpaCal). In figure 2.7 the main calorimeter components are shown. The green area presents the electromagnetic (EM) parts of the calorimeters and the orange area presents the hadronic (Had) part. The Labels are placed in the corresponding positions for the main calorimeters. The blue area presents the instrumented iron which is a system providing measurement of high energetic particles leaking out of the LAr. The SpaCal is presented by the green areas.

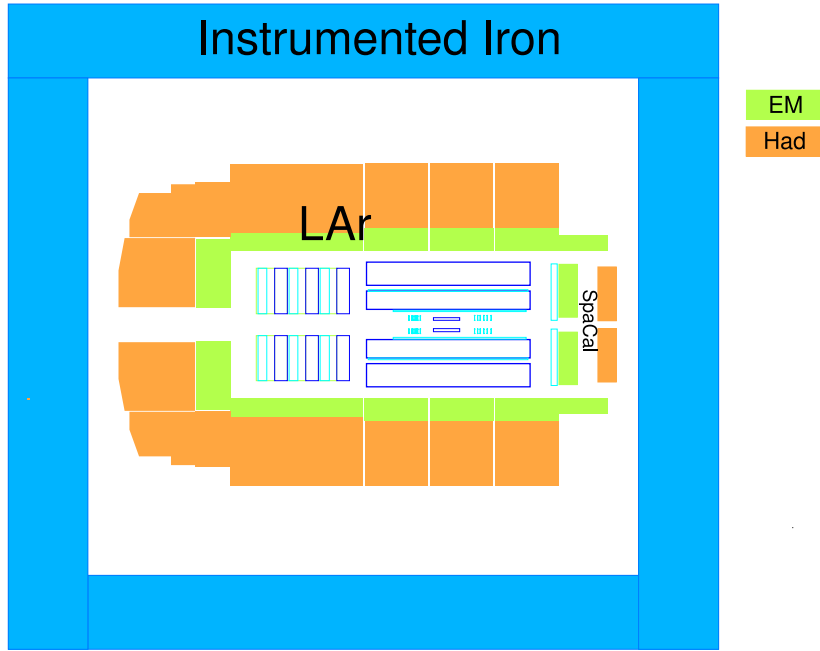


Figure 2.7: A longitudinal view of the H1 calorimeter systems. The electromagnetic part of the calorimeters are presented with green area while the hadronic parts are shown in orange colour.

- **LAr Calorimeter** [76]

The LAr calorimeter provides energy information for neutral and charged particles in the angular acceptance of $4^\circ < \theta < 153^\circ$ and it provides measurement of the scattered electron for high virtuality Q^2 . It consists of two parts: the inner electromagnetic part (ECAL) with lead absorbers and the outer hadronic part (HCAL) with steel absorbers. The active medium of the calorimeter is liquid argon. The calorimeter is divided into eight wheels along the z axis, each consisting of eight octants in the transverse plane. In order to obtain isotropic resolution in all directions the absorber plates were oriented such that the angle between the incoming particle from the nominal interaction point and the plates is always larger than 45° . Therefore the plates were placed perpendicular to the beam pipe in the forward direction while in the central region they were installed parallel to the beam pipe. In beam test measurements [77] the resolutions for the ECAL and HCAL were determined to be:

$$\frac{\sigma(E_e)}{E_e} \approx \frac{1}{\sqrt{E_e}[\text{GeV}]} \oplus 1\% \text{ for ECAL} \quad (2.1)$$

$$\frac{\sigma(E_\pi)}{E_\pi} \approx \frac{0.55}{\sqrt{E_\pi}[\text{GeV}]} \oplus 2\% \text{ for HCAL} \quad (2.2)$$

- **SpaCal Calorimeter** [78]

The SpaCal is placed in the backward region of the H1 detector and provides energy

measurement of particles in the angular range of $153^\circ < \theta < 174.5^\circ$. It has the main purpose to measure precisely the energy of the scattered electron at medium values of Q^2 . It consists of two parts, electromagnetic and hadronic. The calorimeter consists of scintillating fibres as active material and of lead plates as absorbers.

Further detector components

The time-of-flight (TOF) system consists of several scintillating detectors located at different points near the beam pipe around the H1 detector. With its time resolution of 2–4 ns it can be synchronised with the HERA clock and therefore is able to distinguish proton background events.

2.2.3 The Luminosity System

The luminosity measurement [79] is based on the measurement of the elastic Bethe–Heitler process [80] ($ep \rightarrow ep\gamma$) which is very precisely calculable in QED. The system is located at $z = -101.8\text{m}$ where the produced photons from the upper reaction are detected. It is sampling calorimeter consisting of silica fibres and tungsten absorbers. The scattered electron from the reaction is measured by an *electron tagger* placed closer to the interaction point at $z = -6\text{m}$ and used to confirm the presence of the scattered electron from the upper reaction.

2.2.4 The H1 Trigger

The bunch crossing rate of about 10 MHz was the input event rate for the H1 detector, whereas the typical ep event rate is expected to occur about 1 kHz. Therefore non ep background events occur about 10^4 times more frequently than an ep events. The main sources of background are interactions of the proton beam with the remnant particles from gases in the non ideal vacuum of the beam pipe or with the beam pipe itself as well as from synchrotron radiation from the electron bunch. In addition, for optimal dead time below 10% the maximum readout rate of the H1 detector is limited to 50 Hz. The H1 trigger was designed to select ep events among the huge amount of background, as well as rare processes which are of particular interest. The information from all sub-detectors is collected in a Central Trigger (CT) and then the decision is taken if the event is kept or not. Details on the design of the H1 trigger are given in [81] and [82].

The H1 trigger works in four levels, where on each level the rates are gradually reduced while the decision time increases. For each bunch crossing, every sub-detector system which delivers trigger information, provides dedicated logical bits which are synchronised with the HERA clock. These bits are called *trigger elements* (TE). These TE are combined via logical expressions and form for each level a *sub-trigger* (ST). A schematic view of the structure of the H1 trigger is shown in figure 2.8. In the following the four levels of the H1 trigger will be briefly discussed:

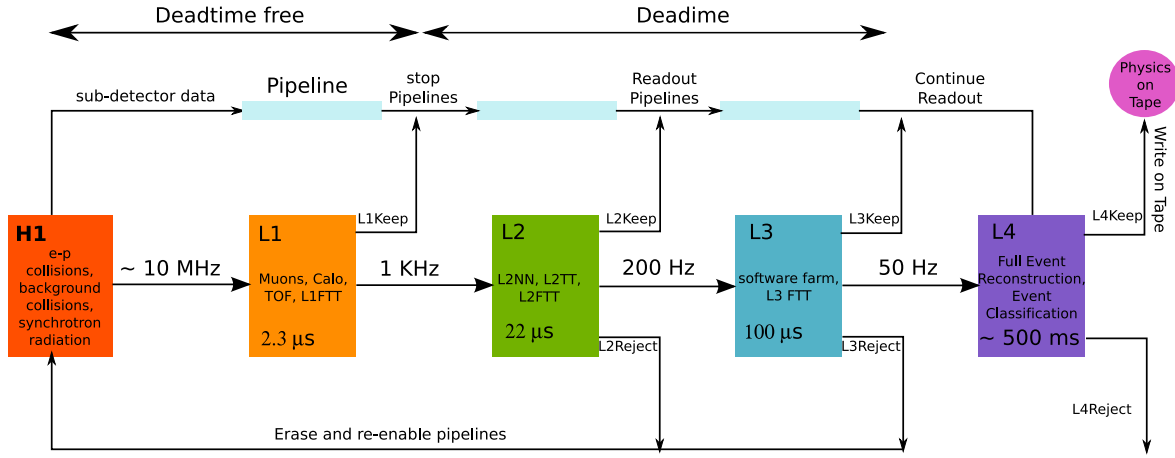


Figure 2.8: A schematic view of the H1 trigger together with the four trigger levels and their properties. Figure inspired by [83]

- **Level 1**

The time for decision for the first level L1, is about $2.3\mu s$, where the rate is reduced to maximum of $\approx 1\text{ kHz}$. The events were stored in a pipe line, such that on this level the data collection continues and the detector is free of dead time. Dead time is the time needed for the detector to read out the event during which it is not possible to record another event. A typical source of dead time is the digitisation of the analog signals in the data acquisition process. In total 256 TE are formed from the information of the sub-systems used for triggering. The CT combines them into 128 L1 sub-triggers (ST). Every ST may have an integer positive number called *prescale factor* ($PF = n$). According to this number only every n th event where the ST is active, is recorded. This leads to two types of the 128 ST, raw trigger bit $L1^{raw}$, which is the decision from the ST itself and the actual trigger bit $L1^{ac}$, after applying the prescale factors. The event is kept if at least one of the actual L1 ST is active,

$$L1Keep = \sum_{i=0}^{127} L1_i^{ac}.$$

- **Level 2**

Once there is a positive decision on level 1, $L1Keep > 0$, the pipeline is frozen, no further event can be recorded and dead time starts. The time for decision at this level is significantly larger than for L1, $22\mu s$ and the rate reduction is from 1 kHz to 200 Hz. The task for the L2 was to validate the L1 decision with help of three additional independent systems: the neural net trigger (L2NN) [84] providing 16 L2 TE, the topological trigger (L2TT) [85] providing 16 TE and the fast track trigger (FTT) [86] providing 24 TE. The FTT was heavily used in the analysis presented here,

therefore a detailed description will be given in a separate section 2.2.4.1. All the L2 TE are combined into 96 L2 ST. The actual bits for this level $L2^{ac}$ are calculated from a L2 validation vector $V2$ and the raw L2 bit, $L2_i^{ac} = V2_i \cdot L2_i^{raw}$, ($i = 0, 95$). The vector $V2$ is calculated from the L1-L2 verification matrix (M^{12}) and the L1 actual bit,

$$V2_j^{ac} = \sum_{i=0}^{127} M_{ij}^{12} L1_i^{ac}.$$

A positive L2 decision is taken and the readout of the H1 detector begins if at least one of 96 L2 actual ST bit is positive:

$$L2Keep = \sum_{i=0}^{95} L2_i^{ac}.$$

- **Level 3**

The third level of the H1 trigger system was enabled only after the inclusion of the FTT within the CT hardware in 2005. It was designed to calculate invariant masses based on track information, such to identify exclusive states like, J/Ψ and D^* mesons and to combine track information with information from other sub-detectors to identify muons and low transverse momentum electrons, down to $p_t^{electron} \approx 1.2$ GeV. The identification of the J/Ψ and D^* mesons is based on dedicated algorithms executed on a software farm. Electrons and muons are identified by matching L1 trigger information with an information delivered by the calorimeter based trigger [87] and information from the muon systems, respectively. The time for decision was $130\mu s$ and the rate reduction goes from 200 Hz to 50 Hz. There were in total 48 L3 FTT TE. After a positive $L3^{raw}$, the calculation of the L3 validation vector, $V3$ is performed, where:

$$V3_j = \sum_{i=0}^{127} M_{ij}^{13} L1L2_i^{ac}.$$

where M^{13} is the L1-L3 verification matrix. Then the actual L3 bit is formed:

$$L3_j^{ac} = V3_j L3_j^{raw}$$

In analogy, the event is kept if at least one of the $L3^{ac}$ is positive:

$$L3Keep = \sum_{i=0}^{47} L3_i^{ac}.$$

- **Level 4**

On the fourth level, a complete event reconstruction is performed and the event is classified with help of dedicated software and does not contribute to the dead time.

The rate reduction goes from 50 Hz to 10 Hz. On the basis of this classification the events were kept or rejected.

During HERA operation, the H1 detector collected as much data as possible while still keeping the dead time below 10%. As long as the L4 input rates were below 50 Hz, no further dead time was accumulated due to the CT. Below 50 Hz the dead time is a linear function of the L4 input rates, above this threshold a strong rise of the dead time is observed (see figure 2.9). To keep the event rates at this level, and in the same time collect as much data as possible is a highly non trivial task. For that reason prescale factors were introduced. They were not kept fixed and an auto prescale strategy was introduced. The Prescale factors for the different sub triggers were calculated from a 1000 events data sample such that the input rate of 50 Hz and less than 10% dead time was achieved. Details on the autoprescale strategy of H1 is given in [88].

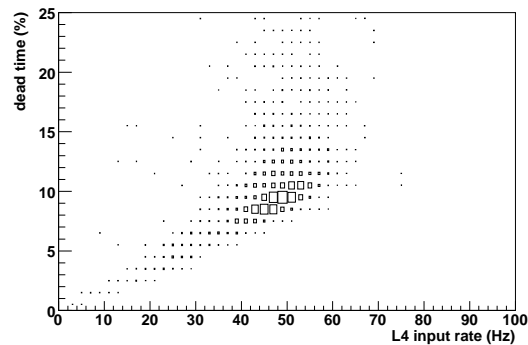


Figure 2.9: The dead time correlated to the L4 input rates. Figure taken from [88]

2.2.4.1 The Fast Track Trigger

The Fast Track Trigger (FTT) was designed to handle the high input rates from HERAII upgrade. The FTT reconstructs tracks using information from the Central Jet Chambers (CJC1 and CJC2) and provides trigger information to the CT on the first three levels. In the following a brief description of the principle of the FTT will be given.

The FTT uses 12 out of 56 wire layers of the CJs. They are grouped in four groups, such that the first three layers are in CJC1 and the fourth one is in the CJC2 (see figure 2.10). Due to the short time available for a decision on the L1 the FTT provides only two dimensional information while at L2, where the time for decision is significantly longer, three dimensional fits and tracks are reconstructed. On the third level, the FTT uses software algorithms for calculating invariant masses, links information from other components of the detector, like the muon system or the LAr and is able to identify muons and electrons.

- **FTT L1**

Wires of the same drift cell and the same trigger layer form a *trigger cell*. In the time available on the first trigger level, ($2.3\mu s$) the analogue pulses of the CJs are digitised at a frequency of 80 MHz and analysed with the fast *Qt* algorithm. This algorithm provides the closest distance of the hit to the wire with the ambiguity on which side

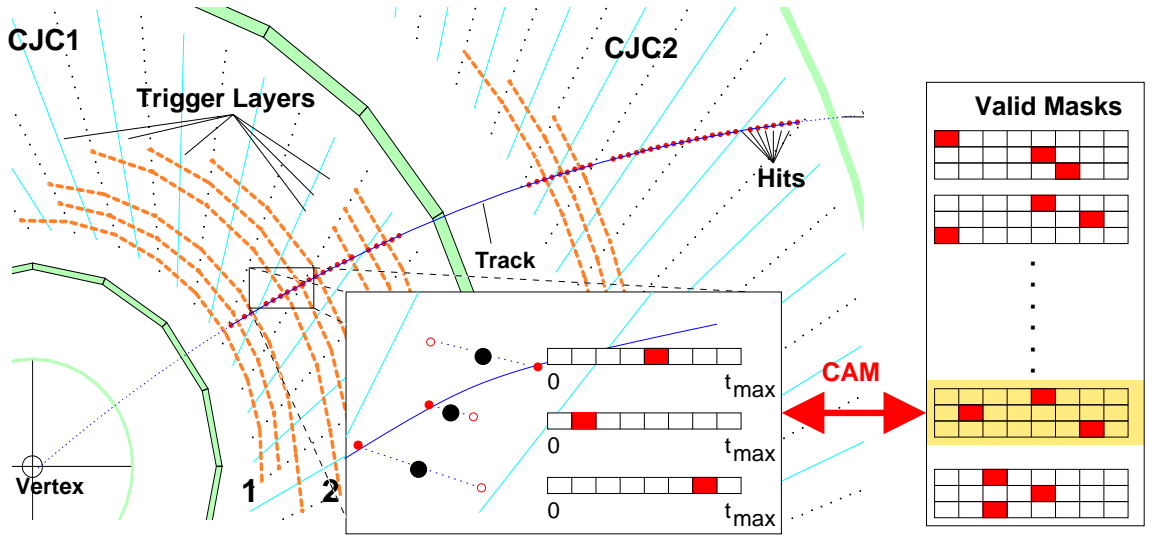


Figure 2.10: Radial view of the CJs of the H1 tracker together with the trigger layers used by the FTT. The figure was taken from [89].

of the wire the hit occurred, left or right (see figure 2.10). Different combinations are collected from each trigger cell and are compared to template of combinations, called trigger masks. If the combination of these “couples” is valid then the hits are considered as a potential track. The charged inverse momentum κ of the track and the azimuthal angle of the track is then known from the mask itself. This information is filled into a two dimensional $\kappa - \varphi$ histogram containing of 16×60 bins for each of the trigger layers. If a coincidence of at least two layers is found then the hits are considered as a track. For the time available the L1 FTT provides track multiplicities with certain p_t thresholds. Details on the L1 FTT are given in [90].

- **FTT L2**

At L2 the time for decision is significantly larger than at L1, therefore more precise information about the tracks can be used. This level is used for validating the information from level 1. The procedure is repeated but with finer binning of the $\kappa - \varphi$ histogram. The number of bins is 60×640 in the $\kappa - \varphi$ plane. Again a track candidate is validated if at least two out of the four layers verify the position of a track in the $\kappa - \varphi$ histogram. In addition, a fit within the $\kappa - \varphi$ plane and the $\kappa - z$ plane is performed and hence a three dimensional information about the track is obtained.

- **FTT L3**

If the event satisfies the track requirements on the second level it is transferred to third FTT level. At this stage information from the LAr calorimeter and the muon systems are also available. Tracks with proper charge combinations are combined and invariant masses of D^* and J/ψ meson candidates are calculated. The identification of a D^*

candidate decaying in the golden decay channel with the Δm method, described in section 3.2.1 of this thesis, is also used on the trigger level. At the end the event is accepted by L3 if the D^* candidates satisfies certain selection criteria relevant for the measurement of a D^* meson. A detailed description of the L3 FTT is given in [91].

Within the H1 detector simulation software, a dedicated program simulating the trigger elements and sub-triggers of the FTT system was implemented. This program is called `fttemu` [92, 91] and is used in the present study.

Chapter 3

Reconstruction and Selection of a D^* Meson

In this chapter an introduction to the properties of the charm meson D^* as well as basic reconstruction techniques are presented.

3.1 D^* meson properties

Around 25% of the charm quarks fragment into a $D^{*\pm}$ meson¹, which is an excited state of the meson D^\pm meson with quantum numbers of $I(J^P) = \frac{1}{2}(1^-)$, where I is the isospin, J total angular momentum and P is the parity. It has a mass of $m(D^*) = 2010.27 \pm 0.17 \text{ MeV}$ [93] and full width of $\Gamma = 96 \pm 22 \text{ keV}$. It was first observed in 1977 with the SPEAR detector at SLAC in e^+e^- collisions at centre-of-mass energies of $\sqrt{s} = 4.03 \text{ GeV}$ [94]. It decays via the strong interaction into a $D^{\pm,0}$ meson dominantly together with a pion. The three known decay modes of the D^* meson are listed at table 3.1. The first one, $D^* \rightarrow D^0\pi$ which is also the one with the highest branching ratio, was chosen in this analysis. The mass difference between the D^* and the D^0 mesons ($m(D^*) - m(D^0) = 145.42 \pm 0.01 \text{ MeV}$) is close to the mass of the pion ($m(\pi) = 139.98 \text{ MeV}$). Therefore, the pion from this decay mode usually has a very low momentum and is thus denoted as a *slow pion*, π_{slow} .

Furthermore, in 54.7% of the cases the D^0 meson decays mainly to $K + \text{anything}$. Important decay modes of the D^0 relevant for this measurement are summarised in table 3.2

¹In the following D^* will refer to both D^{*+} and D^{*-} if not specified explicitly.

Channel	Branching Ratio
$D^0\pi^\pm$	$(67.7 \pm 0.5)\%$
$D^\pm\pi^0$	$(30.7 \pm 0.5)\%$
$D^\pm\gamma$	$(1.6 \pm 0.4)\%$

Table 3.1: The decay channels for D^* meson as listed in [93]

Channel	Branching Ratio
$K^\pm \pi^\mp$	$(3.89 \pm 0.05)\%$
$K^\pm \pi^\mp \pi^0$	$(13.9 \pm 0.5)\%$
$K^\pm \rho^\mp$	$(10.8 \pm 0.7)\%$
$K^\pm \pi^\mp \pi^\mp \pi^\pm$	$(8.1 \pm 0.2)\%$
$K^\pm l^\mp \nu_l$	$(6.89 \pm 0.14)\%$

Table 3.2: The decay channels for D^0 meson as listed in [93]

3.2 Reconstruction of D^* mesons

A particular channel of the D^0 decays modes is when a D^0 decays into a charged kaon and pion: $D^0 \rightarrow \pi^\pm K^\mp$. It has a relatively small branching fraction, but the final state contains only two charged particles which are easy to detect in the central tracking device.

In a summary, the D^* meson is reconstructed via the so called *Golden decay channel* where

$$D^{*\pm} \rightarrow D^0 \pi_{slow}^\pm \rightarrow (K^\mp \pi^\pm) \pi_{slow}^\pm \quad (3.1)$$

with a branching fraction of:

$$\mathcal{BR}(D^* \rightarrow K \pi \pi_{slow}) = \mathcal{BR}(D^* \rightarrow D^0 \pi_{slow}) \cdot \mathcal{BR}(D^0 \rightarrow K \pi) = (2.63 \pm 0.5)\% \quad (3.2)$$

It has only three charged particles in the final state, which imply lower combinatorial background² with respect to other channels. Another advantage is the limited phase space for the π_{slow} which further reduces the background.

3.2.1 Selection of a D^* Candidate

As motivated above, the Golden Decay channel (equation (3.1)) was used in this measurement. In the following the experimental procedure of reconstruction of the D^* is described.

The tracks of the decay particles $K \pi \pi_{slow}$ are well measured in the central part of the tracking device of H1. The measurement of a D^* meson proceeds in the following steps. At first, two oppositely charged tracks, fulfilling the angular and momentum requirements (see table 3.3) of the K and π candidates, are chosen. A four-momentum of these particle candidates is formed from the momentum as measured in the tracker and the nominal mass values as taken from [93] for the K and π . The invariant mass of the two tracks is calculated and if it is within 80 MeV around the nominal D^0 mass $m_{D^0} = 1864.84 \pm 0.17$ MeV the two tracks are considered as K and π candidates from the decay of a D^0 . The four vector of

²In this thesis, *combinatorial background* refers to random combinations of particles which fulfil the charge and momentum requirements and fall in the mass range.

the D^0 is formed and the procedure is continued with a selection of a successful π_{slow} . A track with the same charge as the π from the D^0 decay is selected within the momentum and angular requirements. The nominal pion mass is assigned and the four vector of the pion candidate is created in a similar procedure as the one for the K and π from the D^0 decay. The invariant mass difference

$$\Delta m = m(K\pi\pi_{slow}) - m(K\pi) \quad (3.3)$$

is determined. If the Δm is below 170 MeV the three tracks are considered as the $K\pi\pi$ candidates of a D^* meson. The four vectors of the D^* and D^0 are defined from the momentum measurement of the decay particles. The Δm distribution (see figure 3.2 top) has a sharp threshold at the pion mass and peaks at the nominal mass difference between the D^* and the D^0 . It has a large contribution from non-resonant background satisfying the selection criteria of the $K\pi\pi$ candidates but which are not originating from a D^* decay. These are normally referred as combinatorial background.

The procedure described above is applied for each of the three tracks fulfilling the charge, momentum and *track quality* requirements.

Successful K , π and π_{slow} candidates are tracks reconstructed in the CJC1 and CJC2 angular acceptance $|\eta| < 1.73$. In order to ensure satisfactory track quality criteria cuts on the starting radius of the tracks and its radial length were applied. Explicitly this cut is at $R_{start} < 50$ cm and it implies that the first track hits were measured in CJC1. The radial length of the track was required to be at least 5 cm in order to ensure enough number of hits in the chambers.

Finally a successful D^* candidate has a transverse momentum of $p_t > 2.1$ and a pseudo-rapidity within the acceptance of the CJC's $|\eta(D^*)| < 1.5$.

At low transverse momentum and forward rapidities the combinatorial background rises very strongly and it becomes very difficult to obtain a D^* signal from the Δm distribution. In order to reduce this background a cut on the momentum fraction of the total transverse momentum of the event carried by the D^* , f , which is defined as

$$f = \frac{p_t(D^*)}{\sum_i E_i \cdot \sin\theta_i} \quad (3.4)$$

was applied. E_i and θ_i are the energy and polar angle of the HFS particles respectively. In order to reduce contributions from the proton remnant particles, the particles were required to have $\theta > 10^\circ$. The effect from this cut has been studied in detail in [95] and here the recommended value of 0.13 was used. Events with $f > 0.13$ means that the D^* carries significant part of the total transverse momentum in the event. This leads to background suppression especially at small $p_t(D^*)$. In addition the transverse momentum sum of the K and π was required to be above 2.2 GeV.

All cuts applied on the $K\pi\pi_{slow}$ and the D^* candidate are summarised in table 3.3.

D^* and Decay Products Cuts
$p_t(K) > 500 \text{ MeV}$ $p_t(\pi) > 300 \text{ MeV}$ $p_t(\pi_{slow}) > 120 \text{ MeV}$
$ \eta < 1.73$ $R_{start} < 50 \text{ cm}$ $R_{length} > 5 \text{ cm}$ $ m(K\pi) - m(D^0) < 80 \text{ MeV}$
$p_t(D^*) > 2.1 \text{ GeV}$ $ \eta(D^*) < 1.5$ $f \geq 0.13$ $p_t(K) + p_t(\pi) > 2.2 \text{ GeV}$

Table 3.3: Table summarising the cuts applied on the D^* decay products and the D^* itself.

3.2.2 Determination of the Number of Particles

The number of D^* particles is obtained from a fit to the Δm distribution. The function of the fit consists of a sum of two functions – one for the background and one for the signal.

Previous detailed studies of the shape and properties of the Δm distribution within the H1 collaboration [91, 96] showed that a best choice for the signal part is the asymmetric *Crystal Ball* (CB) function [97]. This function is a Gauss function for the left part, where the Δm has a threshold defined by the pion mass and it has an exponential function for the asymmetric tail towards larger Δm values. This asymmetry is driven by the fact that there are non Gaussian tails from the topology of the decay which are heavily suppressed towards smaller Δm values due to the sharp threshold at the pion mass. The asymmetry of the function is governed by the parameter α which determines the distance from the mean of the distribution in terms of σ where the Gaussian function changes to exponential. The smaller α is, the stronger the tail is.

For visualisation purpose the CB function is shown in figure 3.1 using the default values for $\sigma = 0.0008 \text{ GeV}$ and $\mu = 0.145 \text{ GeV}$, with one of the two asymmetric parameters varied while the other one was kept fixed. The resulting curves can be seen in figure 3.1. It shows that for really large absolute values of α the function is not distinguishable from a Gauss, while for small absolute values the asymmetry of the function is clearly visible.

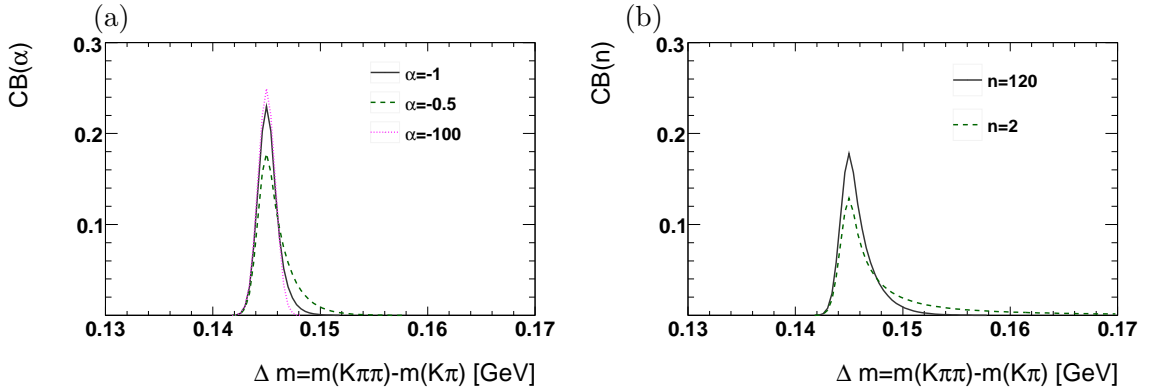


Figure 3.1: The CB function drawn for fixed values for the width and the mean, and different values for α when $n = 120$ is fixed (a) and fixed $\alpha = -0.5$ and different values for n (b).

The analytical expression of the CB formula is:

$$\text{CB}(\Delta m) = \text{bw} \cdot \frac{N(D^*)}{N_{\text{NORM}}} \cdot \begin{cases} \exp\left(-\frac{1}{2}\left(\frac{\Delta m - \mu}{\sigma}\right)^2\right) & \text{if } \frac{\Delta m - \mu}{\sigma} \leq -\alpha \\ \frac{\left(\frac{n}{|\alpha|}\right)^n \exp\left(-\frac{1}{2}\alpha^2\right)}{\left(\frac{n}{|\alpha|} - |\alpha| + \frac{\Delta m - \mu}{\sigma}\right)^n} & \text{if } \frac{\Delta m - \mu}{\sigma} > -\alpha \end{cases} \quad (3.5)$$

where the $N(D^*)$ is the number of D^* mesons, bw is the bin width of the Δm distribution, σ is the *width* of the Gaussian part of the function and μ is the *mean* value of the Δm distribution. In order to determine the number of particles the proper normalisation of the function has to be known. The CB function is not integrable analytically, but it involves sophisticated superposition of the CB function parameters and the Gauss error function erf. The expression for the integral used in this analysis was directly taken from [98].

The analytic formula for the background function is:

$$\text{BG}(\Delta m) = \text{bw} \cdot U_{\text{bg}} \cdot (\Delta m - m_{\pi})^{U_{\text{exp}}} \cdot (1 - U_{\text{corr}} \Delta m^2) \quad (3.6)$$

which was first introduced in [59]. The parameters of the function are the following: U_{BG} is a normalisation factor, U_{exp} is the power factor which is typically around 0.5. The U_{corr} is a correction factor for the far edges of the background at the border of the measurement $\Delta m \approx 170$ MeV.

A common choice for the background function in previous H1 measurements is the *Granet parametrisation* which was also studied in this measurement. The inclusive Δm fits give compatible results with the function defined in (3.6). It has one more parameter than (3.6) and therefore in fitting differential distributions of low statistics the convergence of the fits is slightly better when using the function (3.6). Therefore function (3.6) is the preferred in this analysis.

In figure 3.2 the Δm distribution in data after the full event and jet selection³. The black markers represent the measured data and the green solid line is the fit result. The fit results to a $3936 \pm 113 D^*$ mesons with a $\chi^2/ndf = 31/54$. The fit is very well reproducing the shape of the data.

Treatment of the MC Sample

The MC samples used in this measurement were the so-called signal MC where only charm quarks are generated. Events were kept if there is a D^* decaying in the golden decay channel (3.1). This leads to very small combinatorial background. For consistency the fit function for the data and MC was kept the same. The inclusive 2-jet MC Δm distribution together with the fit can be seen in figure 3.2 below. The fit result is not as good as for the data $\chi^2/ndf = 359/54$ but this is due to the fact that the combinatorial background in the MC is very small in comparison to the signal.

Treatment of the Parameters in the Differential Fits

For the limited statistics of the measurement or due to very large combinatorial backgrounds and small signals (e.g towards small p_t or forward rapidity) and due to the large number of free parameters the fits in the differential distributions often diverge. Therefore some of the fit parameters were fixed. In an extensive study in previous H1 analysis [96] it was recommended to keep the n parameter fixed to value of $n = 120$. After that, the inclusive 2-jet Δm distribution was fitted with all other parameters free (see figure 3.2). The value for α was obtained and then kept fixed for the differential distributions. For the unsuccessful fits, the width σ was also fixed to a value obtained from a simultaneous fit to the same bin and distribution from the MC sample multiplied with a factor derived from the ratio of $\sigma_{\text{data}}/\sigma_{\text{MC}}$.

³The selection criteria on the events and the jets are given in the next chapter, 4.

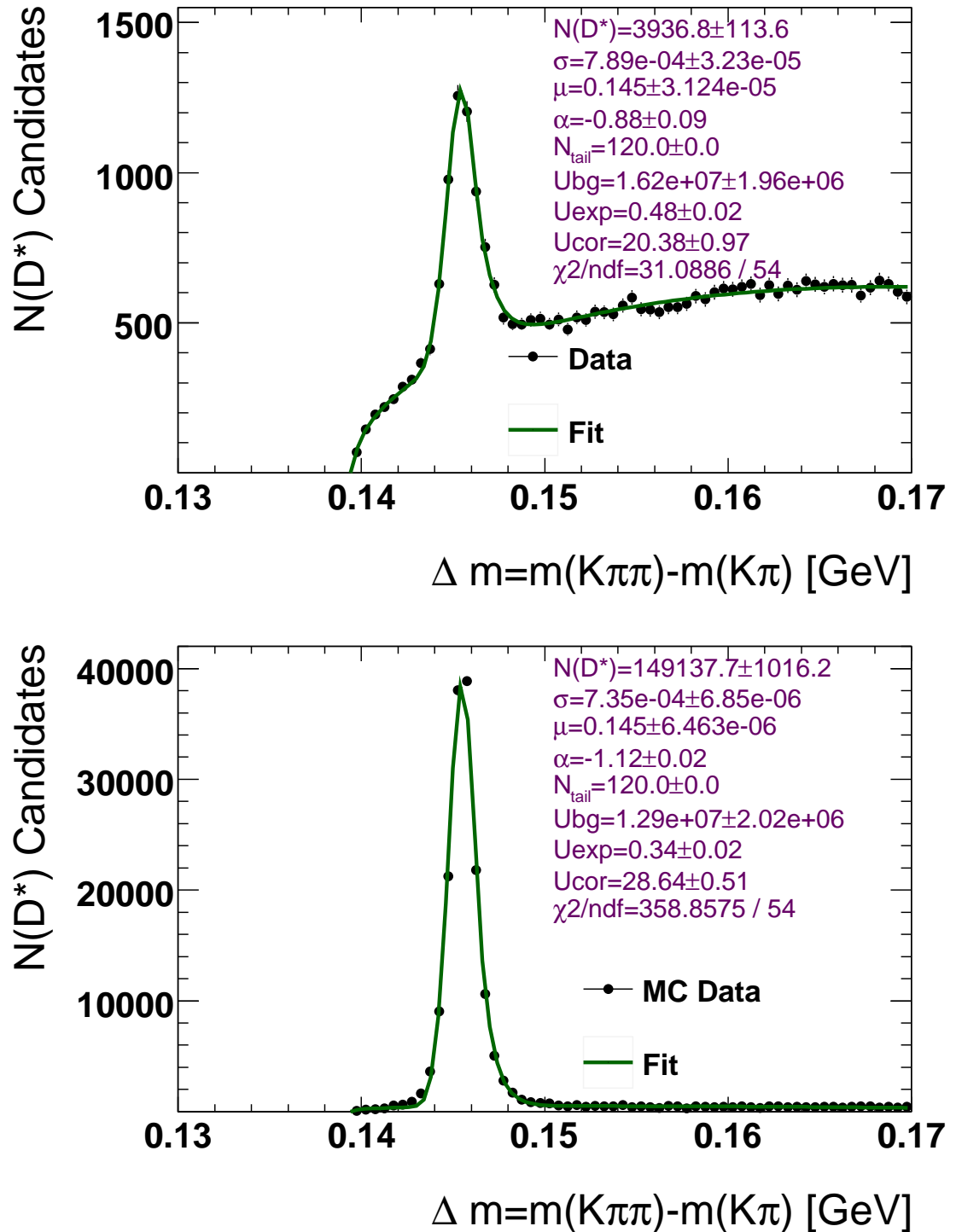


Figure 3.2: The inclusive D^* and di-jet Δm distribution within all photoproduction and trigger selection cuts. The upper plot represents the data sample and the lower plot represents the MC sample. The data points (or MC data points) are represented by black markers, the fit is drawn with a green solid line.

Chapter 4

Event Selection and Reconstruction

In the first part of this chapter the photoproduction event selection (sections 4.1,4.2) as well as the jet selection (section 4.3) is described. The second part of this chapter is devoted to description the data by the detector simulated Monte Carlo (MC) samples (section 4.4) and detector response quantities like relations from hadron to reconstruction level, resolutions and purities (section 4.5). This measurement is using the `root` package [99] and the `h1oo` framework [100].

4.1 General Event Selection

The measurement is based on the data sample of H1 collected in the e^+ 2006/2007 HERA II running period. At H1 there is a classification of the running periods as *good*, *medium* or *bad*. Bad runs are those runs when important detector components like the CJC, luminosity system etc were not operating. Components which are relevant for the measurement are required to be switched on and included in the readout, namely: CJC1, CJC2, LAr, TOF, CIP, Lumisystem, SpaCal. Since this measurement is performed with the Fast Track Trigger (FTT)¹, only runs after the commissioning of the FTT are taken into account, namely after run number 477240. This leads to integrated luminosity of 113.14 pb^{-1} .

4.2 Photoproduction Selection

As described in section 1.2.3 in photoproduction the invariant mass of the exchanged photon Q^2 is very small (quasi real photons). The electron is scattered at very large polar angles and escapes detection from the main H1 detector volume trough the beam pipe. After the HERA II upgrade of the SpaCal system, the acceptance of this component is smaller leading to larger minimum Q^2 , $Q_{\text{SpaCal}}^2 \approx 2 \text{ GeV}^2$. Hence photoproduction events can be identified

¹Selection of the sub-triggers used in this analysis as well as the trigger efficiency determination is discussed in a later chapter 5

by a veto requirement that no electron is identified in the SpaCal calorimeter. An electron is defined as an electromagnetic cluster with energy larger than 8 GeV and a radius of 4 cm.

Since in photoproduction no electron is detected all event variables are reconstructed from the four vectors of all Hadronic Final State particles (HFS) using the *Jacquet-Blondel* method² [101]. The inelasticity y of the event:

$$y_{\text{JB}} = \frac{1}{2E_e} \cdot \sum (E^i - p_z^i) \quad (4.1)$$

where the E_e is the energy of the incident electron, E^i and p_z^i are the energy and z component of the three vector of each HFS particle. However some of the HFS objects also escape detection through the beam pipe, especially in the forward direction. In [101] was shown that for these particles the energies and longitudinal component of the momenta are of the same order $E \approx p_z$ and therefore contribute only little to the y_h . This measurement is restricted to $0.1 < y_h < 0.8$ which corresponds to $100 \text{ GeV} < W_{\gamma p} < 285 \text{ GeV}$ (see equation (1.6)). When selecting events with $y_h > 0.1$ events with particles going in the extreme forward region are excluded from the measurement, and sufficient reconstruction of the HFS objects and y_h is provided. Since the initial $E - p_z$ of the event is $2 \cdot E_e \approx 55 \text{ GeV}$ events with very large y_h are with large Q^2 . Therefore the upper limit of the y_h is restricting contributions from DIS events.

In order to suppress backgrounds from interactions in the beam pipe or interactions with particles in the remaining gas in the beam pipe a cut on the interaction vertex is applied $|z_{\text{vtx}}| < 35 \text{ cm}$

All cuts defining the reconstruction level photoproduction criteria are summarised in table 4.1.

Photoproduction Event Selection Cuts
$Q^2 < 2 \text{ GeV}$
$0.1 < y_h < 0.8$
$E_e < 8 \text{ GeV}$
$ z_{\text{vtx}} < 35 \text{ cm}$

Table 4.1: A table summarising the photoproduction event selection.

4.3 Jet Selection and Reconstruction

As an input to the jet finding the calibrated hadronic final state (HFS) objects found according to the Hadroo2 [102] algorithm were used. Full particles kinematics are reconstructed from combined information by the tracking and calorimeter systems such that double counting of energies is avoided, and best precision is achieved. Afterwards the particles four vectors were

²This method is also known as the hadron method and will be referred as such in the following.

calibrated according to [103] and fed in the jet finding algorithm. The jets were reconstructed using the inclusive k_t algorithm as implemented in the FastJet package [104]. The finder is ran in the laboratory frame using the energy recombination scheme such that the jets are massive (see section 1.2.6).

As the decay products of the D^* are of very low energies, especially the slow pion which is produced at the mass threshold, the tracks produced by them are curling in the magnetic field of the H1 detector. Very frequently it happens that these particles end up in another jet, not the one which was produced by the original charm quark, which fragmented in the D^* meson. In order to be able to identify the jet which originates from the D^* , the four vectors of the decay products K , π and π_{slow} were removed from the list of final state particles and were replaced with the one of the D^* . The jet where the D^* was found to be in is labelled as a D_{jet}^* . The angular phase space of the D^* jet is restricted to that one of the D^* meson, $|\eta(D_{jet}^*)| < 1.5$. In addition to the D_{jet}^* a second jet with the same transverse momentum is required. The angular acceptance of the second jet is opened up to the limits of the H1 detector $-1.5 < \eta(\text{Other jet}) < 2.9$. *The other jet* is defined as the highest p_t non D^* jet in the event. A *di-jet* event is the one with a D_{jet}^* and another jet with $p_t > 3.5$ GeV with an invariant mass $M_{jj} > 6$ GeV. For each D^* candidate the jet finding is repeated. All jet selection cuts are summarised in table 4.2.

Di-jet Selection Cuts
$p_t(\text{jet}) > 3.5 \text{ GeV}$
$ \eta(D_{jet}^*) < 1.5$
$-1.5 < \eta(\text{Other jet}) < 2.9$
$M_{jj} > 6 \text{ GeV}$

Table 4.2: A table with the di-jet selection criteria.

4.4 Control Distributions

For the correction of the data to hadron level a reconstruction level Monte Carlo (MC) sample is used (see section 7.1). In order to obtain reliable results for the cross section, a good description of the data with a MC simulation passed through the full detector simulation is necessary. Inefficiencies or a wrong description of the data could have two possible reasons: the input from the MC generators or the detector simulation could be wrong or insufficient. The first one is solved by a *reweighting procedure* where the MC is artificially shifted to fit the data. The second one is treated when a cut is applied and the inefficient region is excluded from the measurement.

In the reweighting procedure, one assumes that the general information on that particular quantity from the generator itself is not fully sufficient. Therefore weights are calculated from

the ratio data/MC distribution. The event weight w is then calculated from the hadron level value of that quantity:

$$f(x) = \frac{\text{data}}{\text{MC}_{\text{rec}}}, \quad w = f(x_{\text{had}}) \quad (4.2)$$

4.4.1 Reweighting the z -vertex distribution

In order to reconstruct the proper event quantities the precise position of the interaction point is needed. The xy position of the interaction vertex varies within few microns. The z coordinate depends on the beam settings of the accelerator and it is approximately a normal distribution with a width of ≈ 10 cm around zero. On generator level this position is always at zero. Thus during the detector simulation an artificial *smearing procedure* for this position is applied. In figure 4.1 the position of the interaction vertex z_{vtx} as seen in data³ (black markers) is compared to the simulated value (dotted line) as obtained from the MC (in this case PYTHIA massless⁴). It can be seen that the distribution in MC is broader than in data. In order to correct for this discrepancy in the MC a *reweighting* function derived from the ratio of data and MC is applied to both reconstruction and hadron level in the derivation of the correction factors. The weight of the event is calculated from the simulated value $z_{\text{vtx,gen}}$. The function is derived from a fit using polynomial function of third order (shown on figure 4.1 (b)). The resulting z_{vtx} distribution is shown in figure 4.1 (a) with the solid blue line. It can be seen that the description of the data with the weighted MC sample is very good.

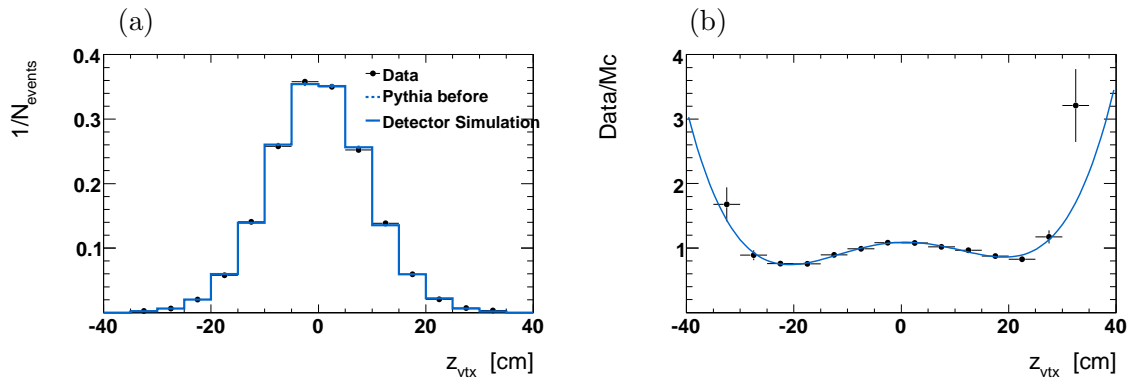


Figure 4.1: The z_{vtx} distribution as seen in data (black markers) and MC simulation (dotted line) shown on (a). The ratio data/MC and reweighting function applied to the MC samples (b) as a function of the z_{vtx} . The resulting reweighted z_{vtx} distribution can be seen on (a) with a solid line

³The vertex position of the interaction point is not expected to depend on a presence of a jet in the event. Therefore this procedure is determined from the inclusive D^* samples.

⁴For the final cross section determination both generators PYTHIA massless and CASCADE were used. However the z_{vtx} distributions and description of the data are identical for both generators. Therefore here only the PYTHIA massless case is shown.

4.4.2 Reweighting the $p_t(D^*)$ Distribution

The p_t distribution of the D^* is an essential quantity. In order to obtain reliable results a good description of the data is required. The decreasing tracking reconstruction efficiency towards low transverse momentum causes large correction factors. Therefore small discrepancies can have large effect on the final cross section. In addition the p_t spectrum is a steeply falling distribution following an exponential function, and migration effects can be sizable. As the raw MC description of the data is very poor as can be seen on figure 4.2 (a) and (c) for PYTHIA and CASCADE respectively (see dashed lines), a reweighting procedure is also needed. The function in use is an exponent plus a constant term and is displayed on figure 4.2 (b) and (d) for the two generators. The resulting MC description is satisfactory and can be seen on figure 4.2 (a) and (c) displayed with the solid line.

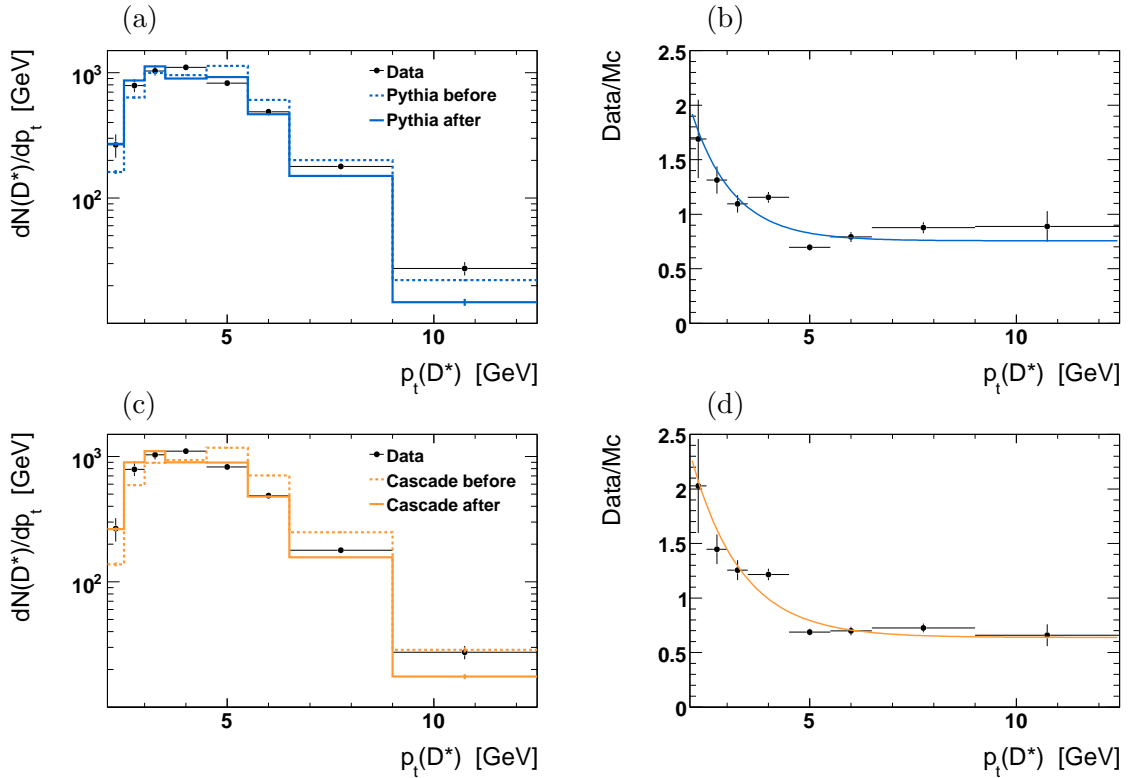


Figure 4.2: The $p_t(D^*)$ distribution compared to unweighted MC samples PYTHIA and CASCADE (dotted lines (a) and (c)) and reweighted in $p_t(D^*)$ samples with solid line. On the left hand side ((b) and (d)) the weighting functions are shown.

4.4.3 Reweighting the $\Delta\varphi$ Distribution

For the correction of the data to hadron level, both MC generators PYTHIA and CASCADE were used. As shown in section 1.3 the azimuthal angle difference between the jets is expected to be highly sensitive to the input of the generator. Therefore these two generators are

expected to give different results. However in order to reduce the systematic uncertainty due to the model (see section 6.2) the difference between the two MC has to be small. For example the reconstruction efficiency as a function of $\Delta\varphi$ in the case when the jets are separated in rapidity $|\Delta\eta| > 1.5$, is shown on figure 4.3 (a) for both MC samples, PYTHIA with the blue line, and CASCADE with the orange one. It can be seen that towards small $\Delta\varphi$ the difference between the two efficiencies varies within 15% which would lead to large model dependence. In addition none of the MC samples provides a reasonable description of the data, as can be seen in figure 4.3 (b). In that figure the $\Delta\varphi$ control distribution is compared to both generators. It can be seen that PYTHIA underestimates the data at small $\Delta\varphi$ and overshoots the data at large $\Delta\varphi$. In contrast CASCADE overshoots the data in small values of $\Delta\varphi$ and is smaller than the data at large $\Delta\varphi$. Therefore a reweighting procedure is also introduced in this quantity. The ratio data/MC is parametrised with polynomial of the second order for both cases. In figure 4.4 the function used, is shown for PYTHIA (b) and for CASCADE on (d). The two reweighting functions are very different for both generators. However, the resulting MC curves are very similar and give satisfactory description of the data. They can be seen on the same figure (a) and (c) represented by the solid line.

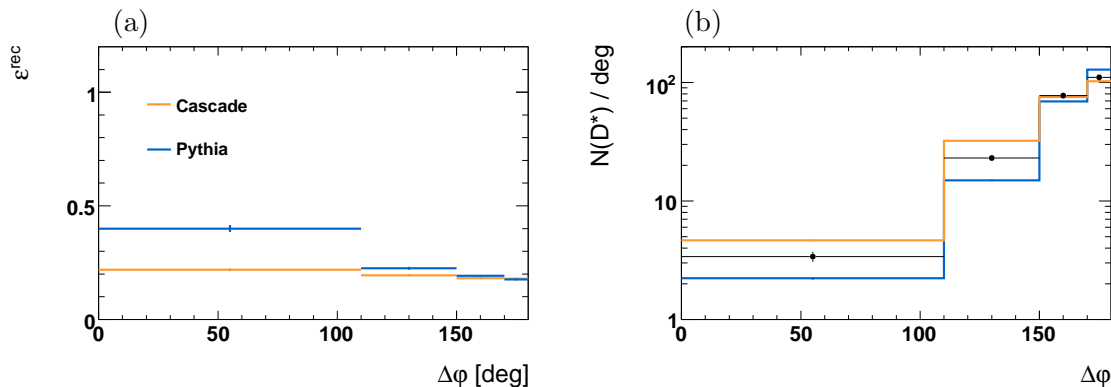


Figure 4.3: The reconstruction efficiency (left) and control distribution (right) as a function of $\Delta\varphi$ as obtained by PYTHIA (blue) and CASCADE (orange).

4.4.4 Control Distributions

After all the reweighting procedures described above, the control distributions for each of the quantities, which are relevant for the analysis has to be checked. In the following the control distributions will be shown. The number of D^* is extracted from the data as described in section 3.2.2. The data points always have weight 1, $w_{\text{data}} = 1$. The distributions are normalised to the bin widths. After that the MC samples are normalised to the number of entries as in the data, and normalised to the bin widths too if not stated explicitly.

- D^* Decay products

In order to check the implementation of the detector simulation for the Central Jet

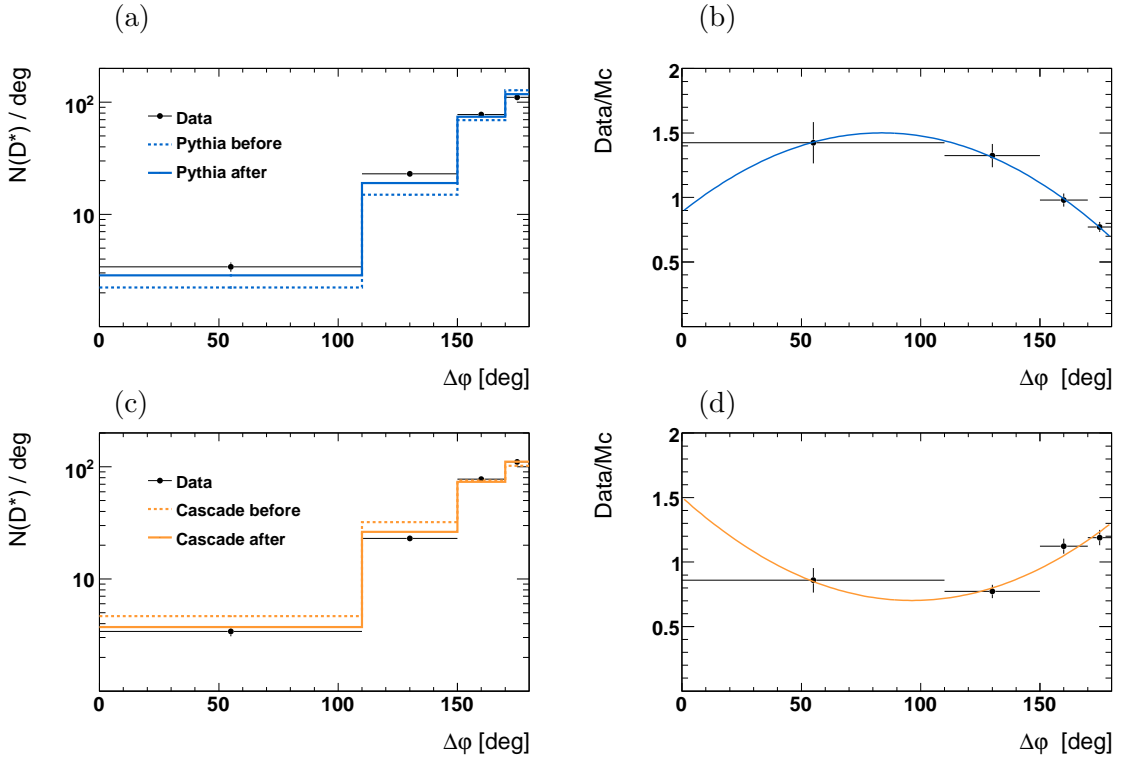


Figure 4.4: The $\Delta\phi$ distribution compared to MC samples PYTHIA and CASCADE. The unweighted ones are shown with a dotted line, the results after reweighting are shown with the solid line. On the left hand side ((b) and (d)) the weighting functions are shown.

Chambers (CJC) or the dead material description, the transverse momenta as well as the rapidity description of the decay particles have to be checked. In figure 4.5 (a), (c) and (e) the transverse momentum of the tracks of the K , π and π_{slow} are displayed. It can be seen that they are very well described by both MC. In figure 4.5 (b), (d) and (f) the pseudo rapidities of the particles are presented. Again no significant discrepancies are observed. In figure 4.6 the radial length R_l (left column) and the polar angle θ (right column) of the K , π and π_{slow} tracks are presented. The radial length of a track is the length of a track in the transverse plane. As can be seen on the figure, not all tracks are measured over the full CJC radial length. Some tracks stop at the border between the CJC1 and CJC2 at around 30 cm. This is especially the case for the π_{slow} since it has a very low momenta and is curling strongly in the magnetic field of the detector. Also secondary interactions of the track with the material between the chambers causes shorter tracks. In general this quantity is well modelled by the detector simulation. No significant discrepancies between data and MC in the case of the polar angle of the tracks is observed ((b), (d) and (f)). The number of D^* for these distributions is determined with a fit. In order to receive reliable fit results the statistics has to be reasonable which limits the number of bins for these distributions.

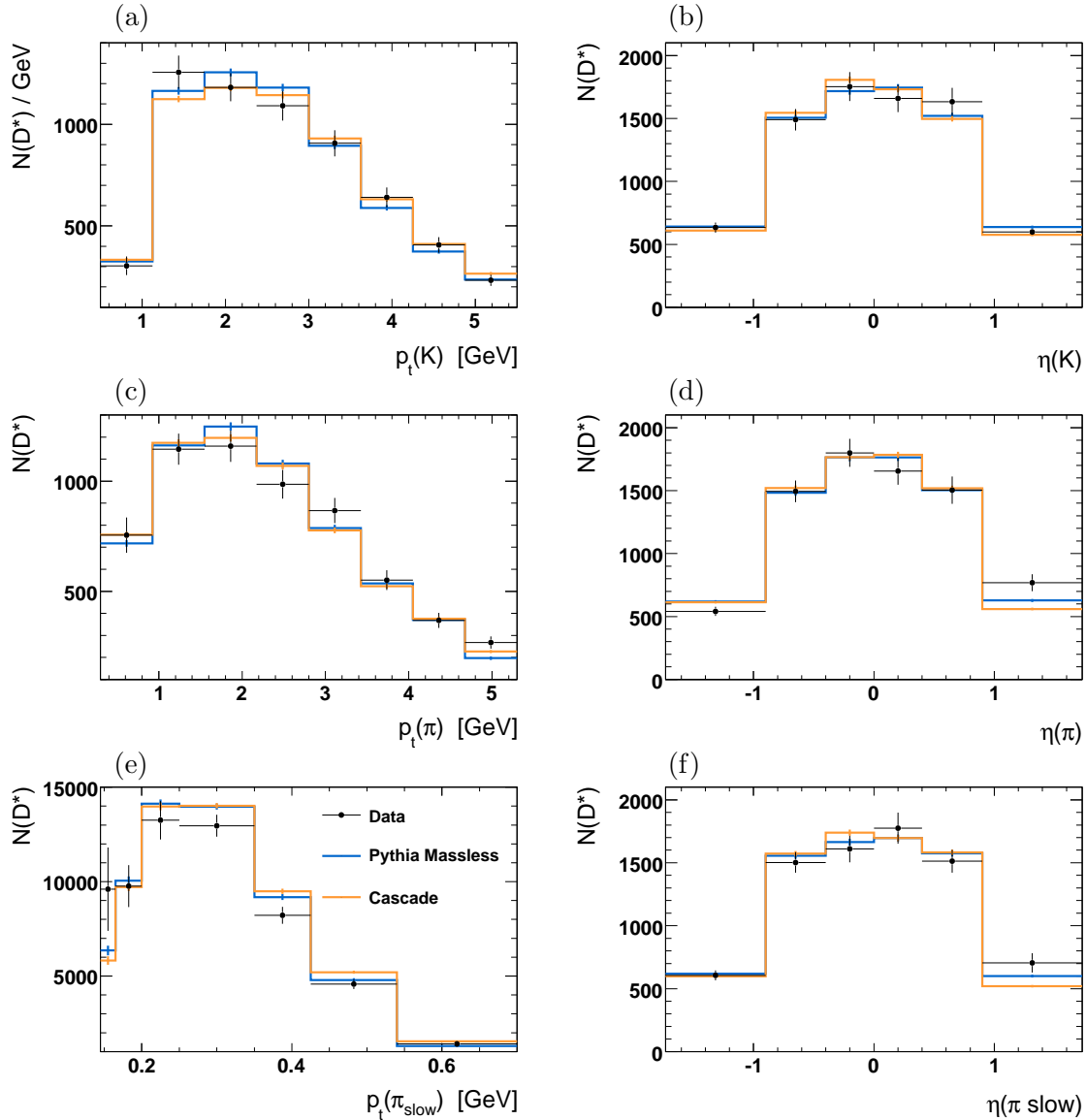


Figure 4.5: The control distributions of the kinematic variables p_t and η for the D^* decay products, K , π and π_{slow} . Data (black markers) are compared to simulations from PYTHIA massless (blue line) and CASCADE (orange line)

- **General D^* and Event Observables**

The $p_t(D^*)$ and $\eta(D^*)$ spectra are shown in figure 4.7 (a) and (b) respectively. The $W_{\gamma p}$ of the event as seen in data is compared to PYTHIA massless and CASCADE and shown in figure 4.7 (c). The sum of the tracks–transverse momenta E_T^{sum} (see chapter 5), is displayed in figure 4.7 (d). And finally the quantity f used to suppress combinatorial backgrounds is shown in 4.7 (e). No significant discrepancies between the data and MC is observed in any of these quantities. This is trivial for the transverse momentum of the D^* because of the reweighting procedure described above.

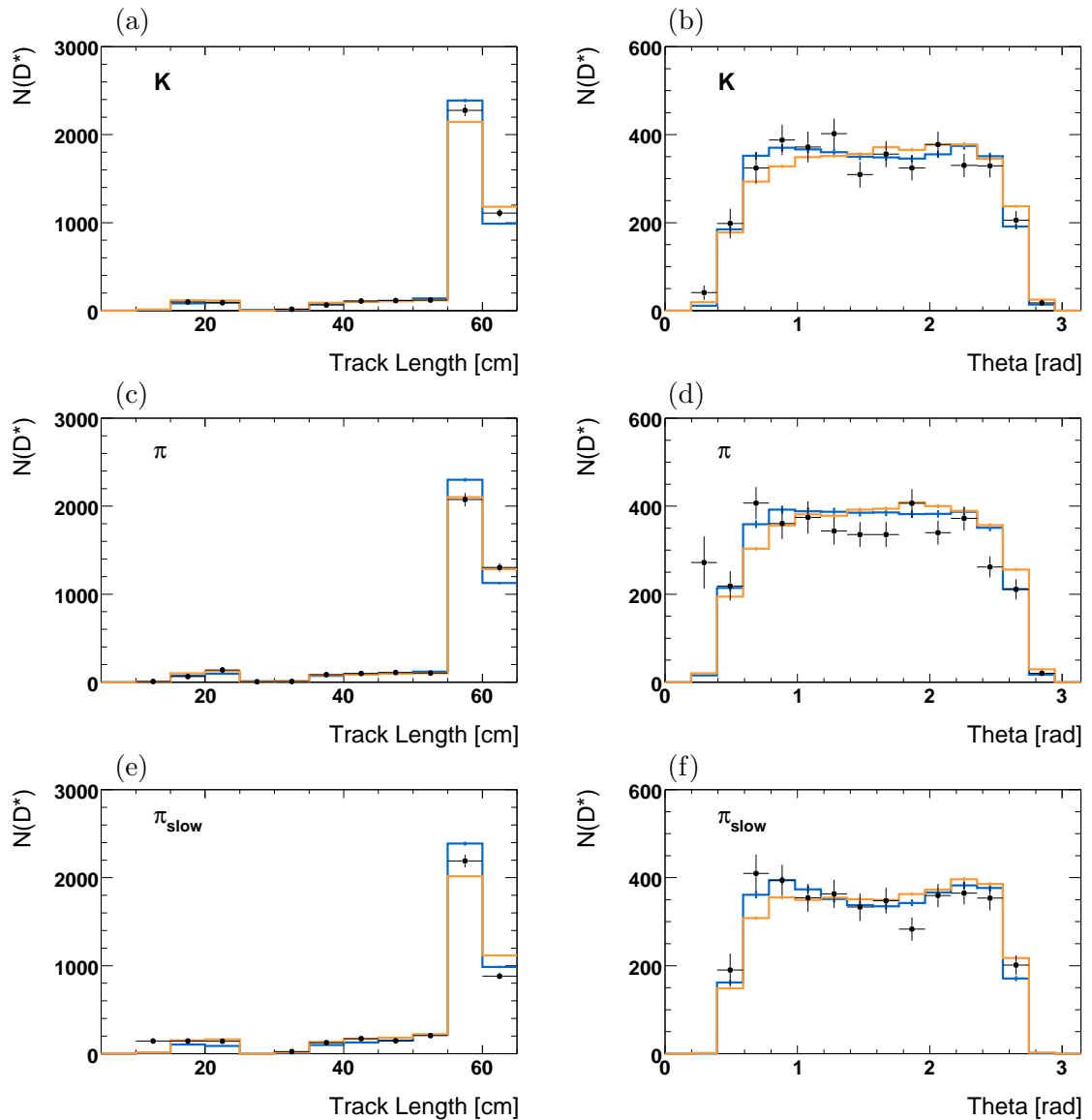


Figure 4.6: The control distributions of track quantities, Radial length (left column) and θ (right column) for the D^* decay products, K , π and π_{slow} . Data (black markers) are compared to simulations from PYTHIA massless (blue line) and CASCADE (orange line)

• Jets Kinematics

In figure 4.8 the jets transverse momenta and rapidities are shown. On (a) and (c) the p_t spectra of the jets can be seen. The $p_t(D_{jet}^*)$ spectrum is much flatter than the $p_t(\text{Other jet})$ which indicates that in most of the cases the D_{jet}^* is often the leading jet in the event. The data are very well described by the two MC. In figure 4.8 (b) and (d) the pseudo rapidities of the jets are shown. The shape of the $\eta(D_{jet}^*)$ follows the pseudo rapidity distribution of the D^* meson itself (figure 4.7 (b)) as expected, while the shape of $\eta(\text{Other jet})$ is significantly different. It rises towards forward η with a

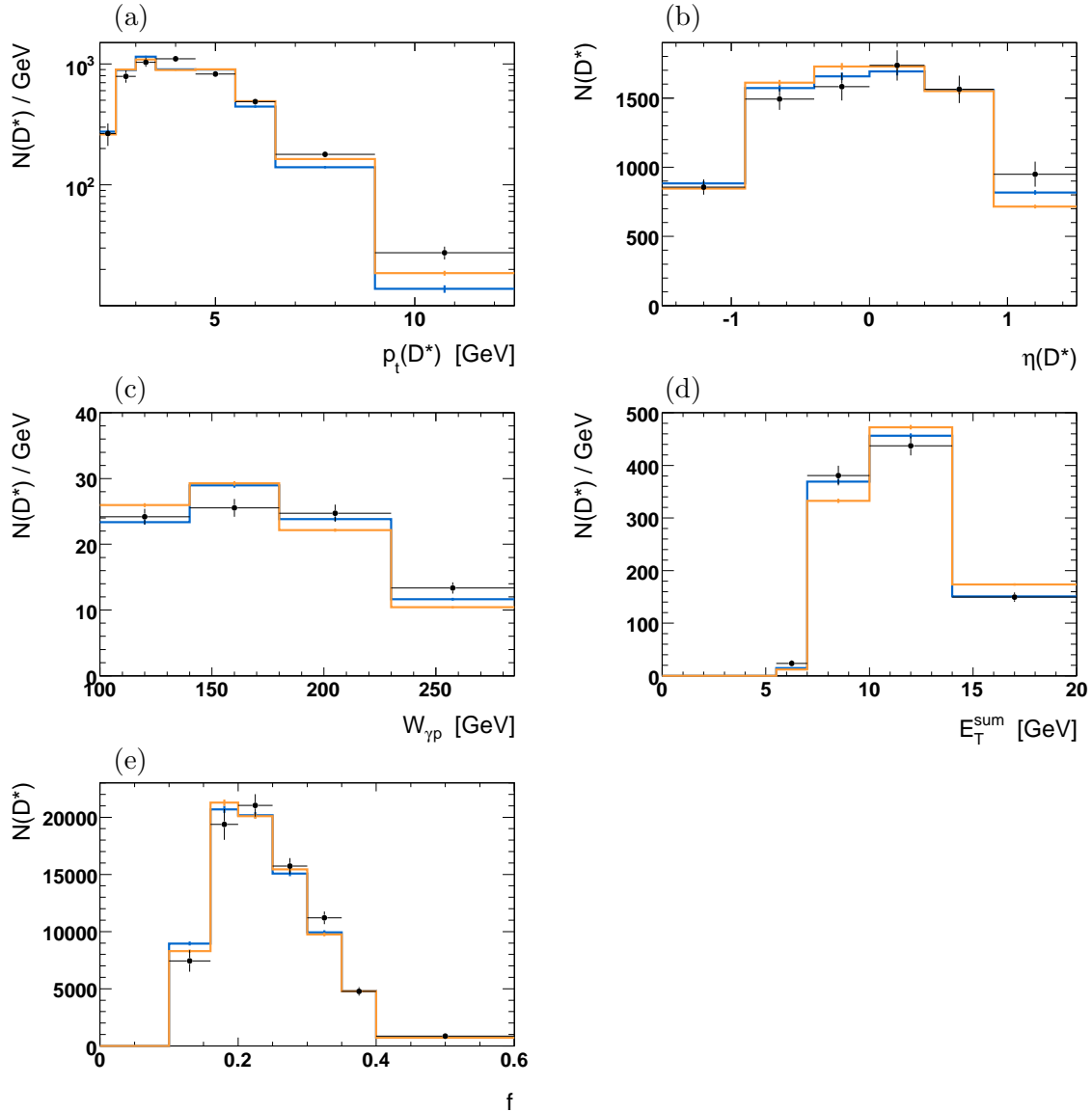


Figure 4.7: The control plots of the D^* , p_t (a) and η (b), $W_{\gamma p}$ (c), E_T^{sum} (d) of the tracks and the f (e) quantity. Data (black markers) are compared to simulations from PYTHIA massless (blue line) and CASCADE (orange line)

peak at around 1.5. The description of the MC in the most forward bin, $2.2 < \eta < 2.9$ is slightly worse than for the rest of the distributions. Still the description is satisfactory enough.

- **Jet Profiles**

Common variables to check are the *jet profiles*. These variables allow to study the topology of the $D^* + \text{jet}$ events and to investigate the energy flow inside and close to the jet axis. They also give an estimate how well the HFS objects are modelled in the

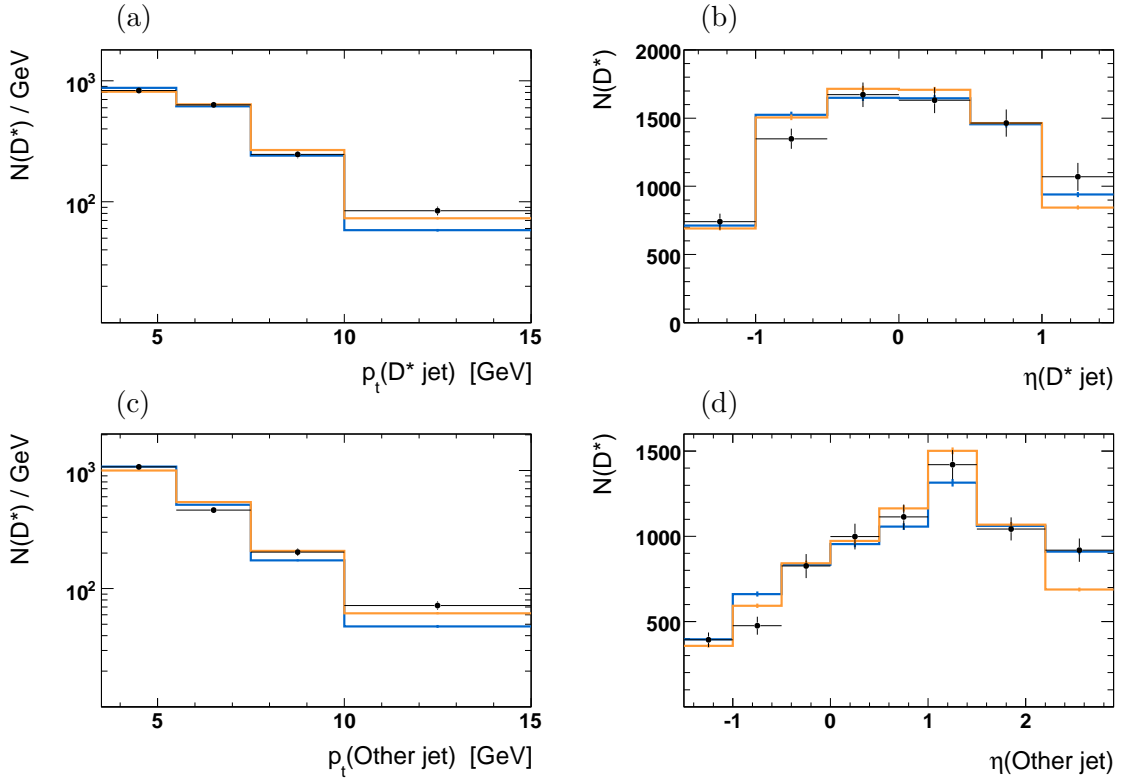


Figure 4.8: The D_{jet}^* p_t (a) and η (b), as well as the Other jet p_t (c) and η (d) control distributions. Data (black markers) are compared to simulations from PYTHIA massless (blue line) and CASCADE (orange line).

detector simulation. The jet profiles give the transverse energy flow with respect to the jet axis, in the azimuthal or the rapidity distance. Each particle enters the histogram with a weight $1/E_{T(\text{HFS particle})}$. The distributions are normalised to 1.

The jet profile in η is obtained from all particles within the slice in $\Delta\varphi < 1$ and is shown in figure 4.9 (a). The peak at 0 shows directly the particles belonging to the jet with a large tail towards the forward direction with a plateau going to maximum rapidity of 2, which are the particles belonging to the second jet in the event.

For the $\Delta\varphi(\text{jet-HFS})$ only particles which are close to the jet axis in rapidity are taken into account ($|\Delta\eta(\text{jet-HFS particle})| < 1$) and is displayed in figure 4.9 (b). The peak around zero shows the particles belonging to the jet. There are also two peaks at $\pm\pi$ which are the particles belonging to the second jet in the event.

Both distributions are well described by the simulations.

- **General Observables**

At last all the observables (see section 1.3) measured in the differential cross sections have to be checked. In figure 4.10 (a) the rapidity separation between the Other jet and

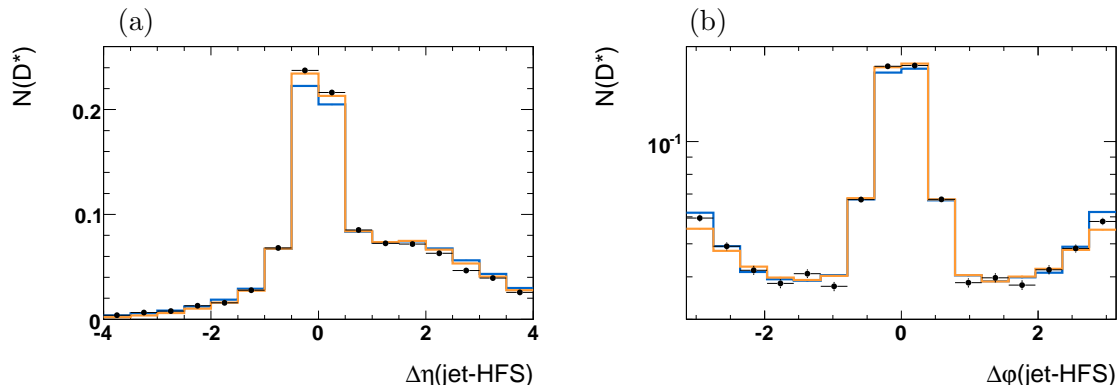


Figure 4.9: The jet profiles control plot $\Delta\eta$ (a) and $\Delta\phi$ (b). Data (black markers) are compared to simulations from PYTHIA massless (blue line) and CASCADE (orange line).

D_{jet}^* $\Delta\eta$ can be seen. A peak at positive values means that normally the Other jet is found more forward than the D_{jet}^* . The distribution is well modelled by the MCs, with the exception of the largest rapidity separation regions. In figure 4.10 (b) the azimuthal angle difference $\Delta\phi$ between the Other jet and D_{jet}^* is shown. After the reweighting procedure described in section 4.4.3 the distribution is very well described. In figure 4.10 (c) the x_γ of the event can be seen. It has a peak at 1, with a tail towards 0. It is fairly well described by PYTHIA with exception in the lowest bin. CASCADE provides satisfactory description and provides the best description in the central bin. In figure 4.10 (d) the invariant mass of the remnant M_X is shown. The distribution has its maximum at values between 50 GeV and 100 GeV and has a large tail towards larger value. The description of the data by the MCs is fairly good with exception in the largest bin where the MCs underestimate the data. There PYTHIA is only factor of 2 below the data, while CASCADE is a factor of three below the data. In figure 4.10 (e) the transverse momentum of the di-jet pair p_t^{jj} is displayed. The two models exhibit very different shapes in comparison to data, PYTHIA is above at small values of p_t^{jj} while CASCADE fits the data very well, and PYTHIA is below the data at high values, while CASCADE is above. Still the control distribution for this quantity is satisfactory. The invariant mass of the di-jet system M_{jj} can be seen in figure 4.10 (f). The distribution is very well reproduced by the MC models.

4.5 Purity and Detector resolution

In this section the detector response is studied with the help of fully simulated Monte Carlo (MC) samples. Quantities like resolution and purity are defined and investigated in different variables relevant for the final cross sections. On hadron level, it could be that the number of D^* decaying in the golden decay channel is at most two. But on the reconstruction level MC

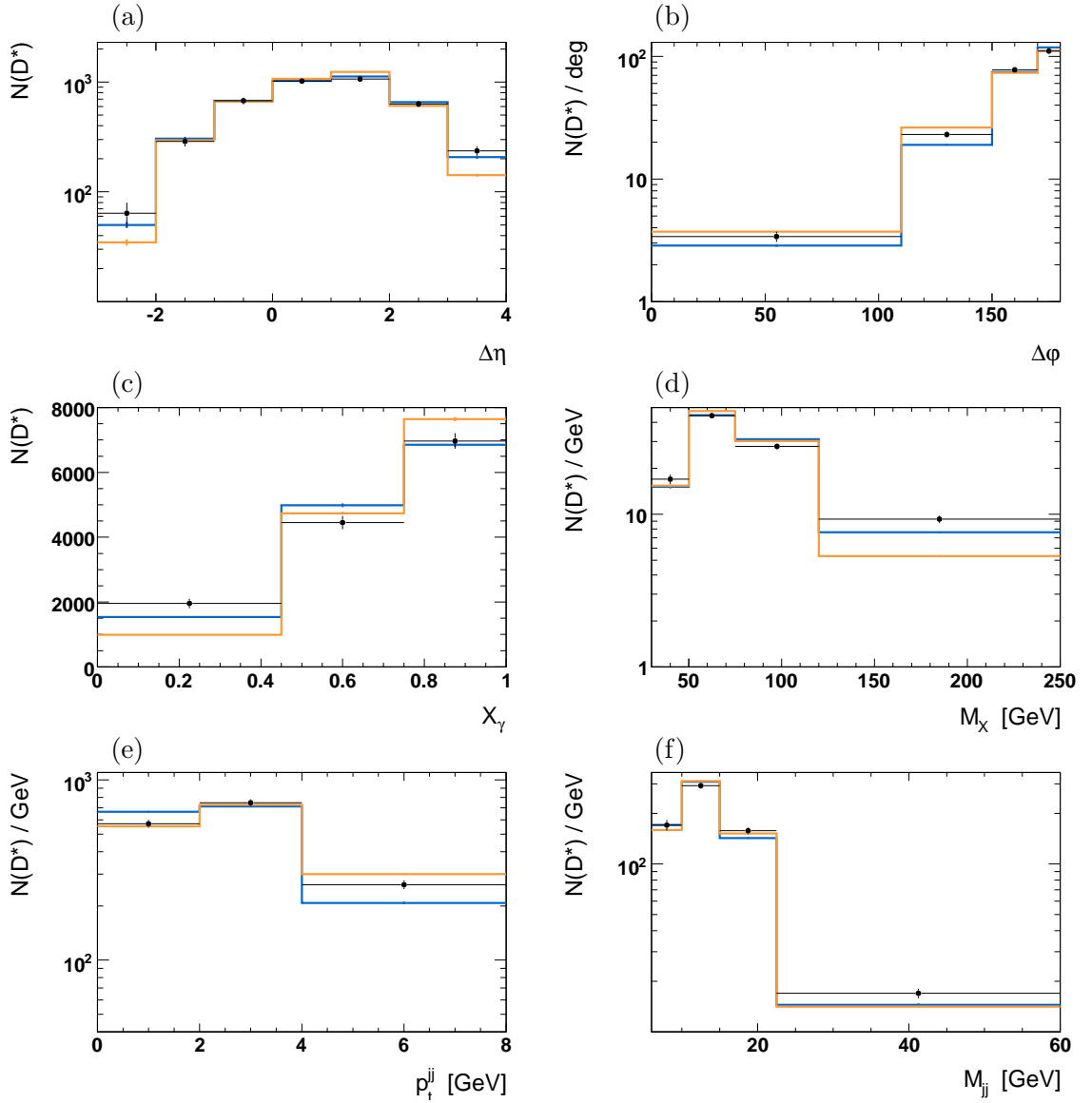


Figure 4.10: The control plots for the final observables measured in the differential cross sections. Data (black markers) are compared to simulations from PYTHIA massless (blue line) and CASCADE (orange line).

it could be that random combinations of charged particle fulfil the requirements for the K , π and π_{slow} such to form a D^* candidate. In order to estimate the proper detector response the correspondence between the D^* on both levels has to be known. Therefore the D^* on hadron level is matched to the D^* candidate on reconstruction level using the charge of the D^* and the angle between π_{slow} . All reweighting procedures defined in the section above are also applied here. The purity is obtained from a MC sample where all the reconstruction level selection cuts were applied while the hadron level selection is released. Hence possible

migrations from outside the phase space of the measurement are also included. None of the photoproduction, D^* and jet visibility cuts are applied on hadron level. The visibility cuts are those cuts defining the final visible range of the measurement. They are summarised in table 7.2.

4.5.1 Purity and Reconstruction Efficiency

A good measure for the detector response is the quantity called *purity*. It is defined as the fraction of events generated on hadron level and reconstructed on reconstruction level in a data interval (or bin) with the total number of events reconstructed in the same bin:

$$\mathcal{P} = \frac{N_{\text{rec}} \wedge N_{\text{had}}}{N_{\text{rec}}} \quad (4.3)$$

In other words it gives a measure of the migration effects due to inefficiencies or resolution problems in the reconstruction procedure. In the ideal case this quantity would be flat at 1. The bin sizes were adjusted such that the purity is relatively flat and is above 60% with rare exception where the migrations from non-neighbouring bins are sizable (e.g $\Delta\varphi$). In order to have a realistic idea of the migration effects in the reconstruction level, all visibility cuts on hadron level were released, in order to allow migrations from regions excluded from the measurement.

The correction to hadron level is done with the *bin-by-bin* method [105]. The technical realization of this method is carried by the *reconstruction efficiency*⁵ derived from a Monte Carlo sample which has been passed through full detector simulation. The reconstruction efficiency is defined as the fraction of events reconstructed after all reconstruction cuts $N_{\text{rec}}^{\text{full}}$, including technical all cuts (like the f quantity cut reducing background, or the electron candidate energy reducing DIS background contributions) over the total number of events generated in the same bin within the visibility range of the measurement $N_{\text{had}}^{\text{vis}}$.

$$\epsilon^{\text{rec}} = \frac{N_{\text{rec}}^{\text{full}}}{N_{\text{had}}^{\text{vis}}} \quad (4.4)$$

In the following the reconstruction efficiencies will be shown together with the purity. For the current study only the PYTHIA massless Monte Carlo sample will be shown, since the difference with CASCADE was minimised in the reweighting procedures described above (section 4.4 of the current chapter). In figure 4.11 the purity and reconstruction efficiency for $p_t(D^*)$ (a), $\eta(D^*)$ (b), p_t and η for the D_{jet}^* ((c) and (d)), p_t and η for the other jet ((e) and (f)) and the invariant mass of the photon proton system are displayed. The D^* purities are very high and close to one. The D^* are reconstructed from the tracks. The tracking information is much more precise than the information from the calorimeter and

⁵Often the reconstruction efficiency in this work is also referred as correction factors, which is the inverse of the reconstruction efficiency.

this leads to minimal mismatch between the hadron and reconstruction level quantity. In addition the D^* were matched on both levels, therefore the migrations for the D^* quantities are minimal. Contrary the jet purities are not so good. However in figure 4.11 (c) and (d) it can be seen that the D_{jet}^* transverse momentum and rapidity are influenced by the purity of the D^* leading to relatively high purity. This is not the case for the other jet. It can be seen that the purity as a function of the rapidity of the other jet, drops down to 60% in the most forward bins. This could be explained with the fact that the other jet's phase space is extended towards the forward region where the tracker information is no longer in use for the determination of the hadronic final state (HFS) four-vectors. There the migration effects from extreme forward particles on hadron level, which on reconstruction level escape detection restricted by the beam pipe is most sizable (see next section).

The reconstruction efficiency as a function of the D^* transverse momentum drops towards small values. The D^* transverse momenta and kinematics in general are driven by the kinematics of the π_{slow} . Towards low momenta, the π_{slow} is more and more difficult to identify. In addition the relatively high transverse momentum cut on the π_{slow} enlarges the possibility that the slow pion on reconstruction level is cut away from the measurement. These two effects cause the drop of the efficiency towards small values of $p_t(D^*)$. As a function of $\eta(D^*)$ the reconstruction efficiency is flat with a drop in the last two bins, towards the edges of the CJC chambers. In these regions the probability that one of the decay products is outside the acceptance of the tracker is high. Both reconstruction efficiencies, $\varepsilon(p_t)$ and $\varepsilon(\eta)$ of the D^* are also reflected in the reconstruction efficiencies of the D_{jet}^* . The ε^{rec} as a function of the other jet rapidity is relatively flat in the central region with a rise toward forward rapidity. This is explained with the fact that the HFS particles are boosted into the forward direction which in general means higher particle multiplicity in the forward direction. The reconstruction efficiency of the $W_{\gamma p}$ is dropping towards large values.

Other purities and reconstruction efficiencies are displayed in figure 4.12. In general the purities are found to be flat, with few exceptions. As a function of the rapidity separation between the jets, the purity drops for the extreme case, where the other jet is found in the most forward direction and the D_{jet}^* is found in the backward direction. Here the phase space is large enough for a third soft jet, and it could be easily misidentified as the other jet. The lowest purity is found in the $\Delta\varphi$ distribution where the purity is slightly below 50%. In this distribution the migration effects from non-neighbouring bins is sizable.

4.5.2 Correlations and Detector Resolutions

In order to estimate how reliable the measured quantities are often correlation plots of the relevant quantity on hadron level and reconstruction level are used. The D^* mesons were matched with the procedure described above (page 57), and the corresponding jet is taken on both levels. The other jet in both cases is the highest non- D_{jet}^* jet. In order to have a

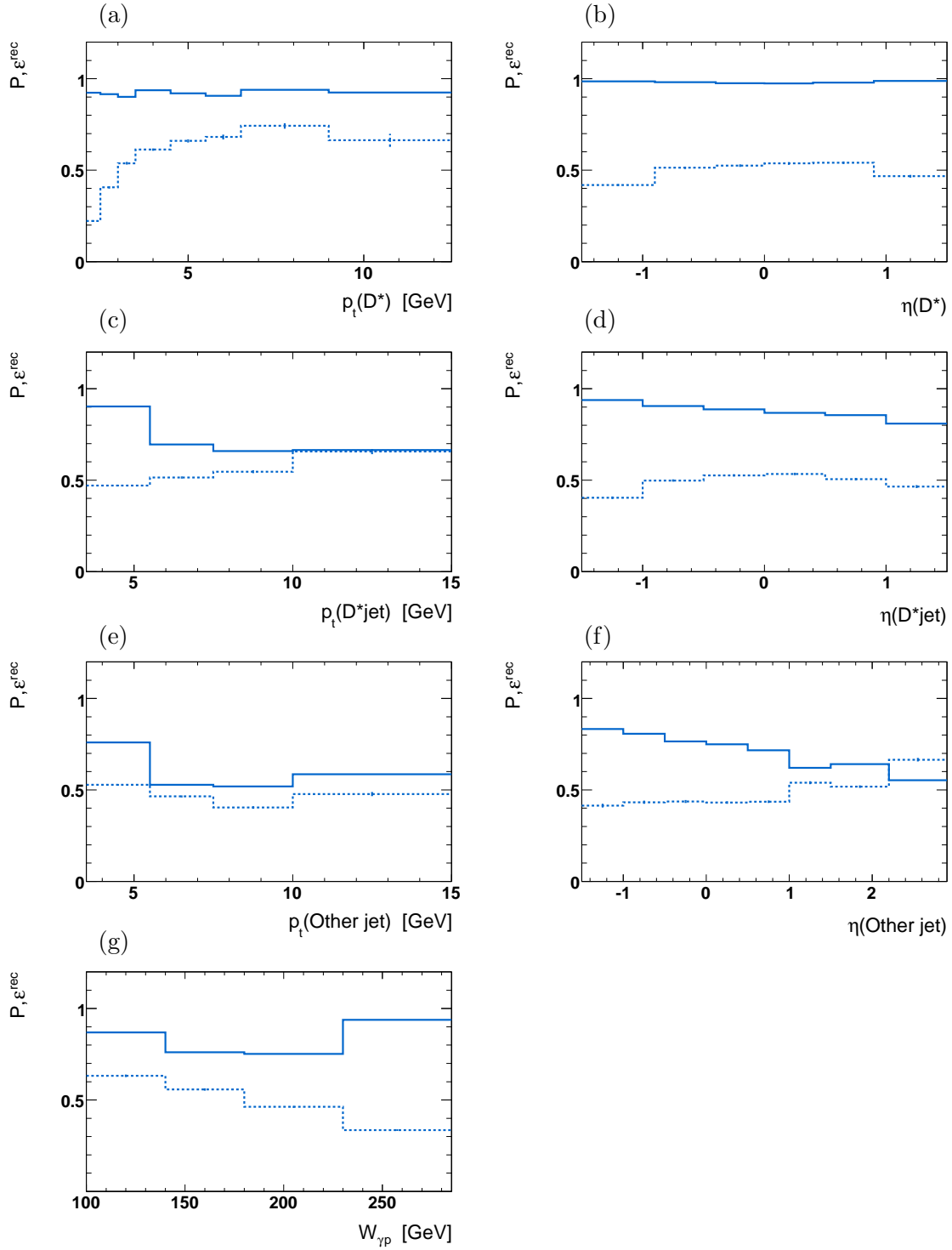


Figure 4.11: The purity (solid line) and the reconstruction efficiency ε^{rec} (dashed line) for the D^* ((a) and (b)), D_{jet}^* ((c) and (d)), Other jet ((e) and (f)) transverse momentum and rapidity respectively and the $W_{\gamma p}$ of the event (g) obtained by PYTHIA.

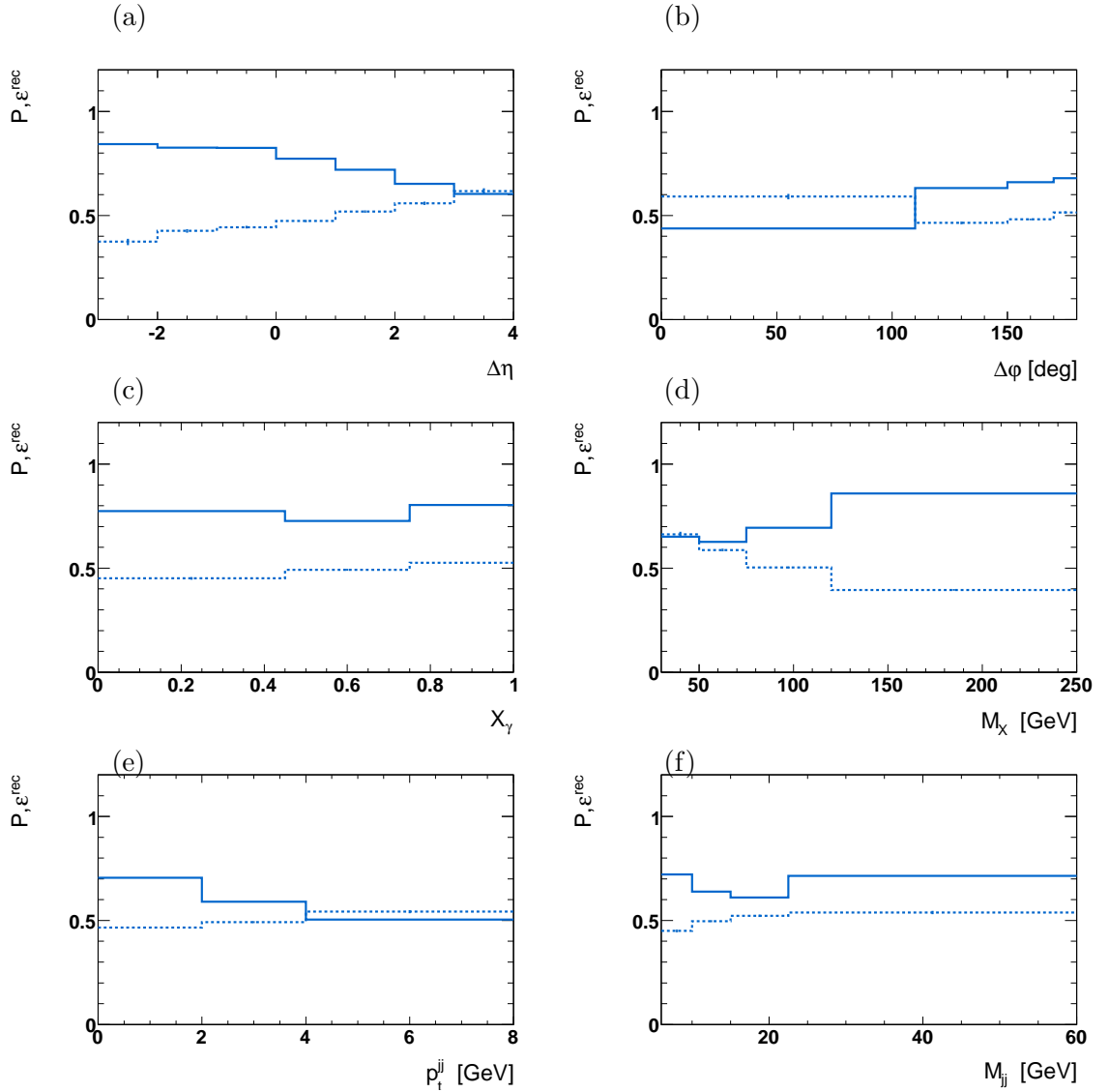


Figure 4.12: The Purity (solid line) and the reconstruction efficiency ε^{rec} (dashed line) as a function of $\Delta\eta$, $\Delta\phi$, x_γ , M_x , p_t^{jj} and M_{jj} from PYTHIA.

realistic estimate on the contributions from outside the measurement all hadron level cuts were released while the full selection on reconstruction level is kept. The resolution is defined as:

$$res = \frac{N_{rec} - N_{had}}{N_{had}} \quad (4.5)$$

In figure 4.13 the correlation between hadron and reconstruction level as well as the resolution as a function of the D_{jet}^* and the other jet η and p_t are shown. As it was discussed before, the D_{jet}^* is well correlated with the D^* meson, in addition the mesons were matched on both levels. This leads to very good correlations for the D_{jet}^* transverse momentum and rapidity. In the same figure it can be seen that the correlation for the other jet is slightly worse.

The correlation matrix for the transverse momentum is more smeared but still diagonal. Here there are sizable migrations from below the measurement cut at 3.5 GeV. The rapidity for the other jet is also fairly well correlated. The biggest decorrelations are found to be in the most forward bin from 2.2-2.9 in η . The resolutions follow a Gauss function only in the ideal case. For example the transverse momentum of a track, what really is measured is the curvature. For that quantity the resolution truly follows a Gaussian distribution. But the transverse momentum of the track is the inverse curvature, therefore deviations from a Gaussian distribution are expected. The limited acceptance of the detector further smears the Gauss distribution. However, a Gauss function is a fairly good approximation. The resolutions were fit with a Gauss function and the mean and the width were obtained. These values are displayed in figure 4.13 right column. According to the MC simulation the η and p_t for the D_{jet}^* are reconstructed 0.1% too high with resolutions of 9% and 11% respectively. The resolutions for the other jet quantities are worse. The other jet rapidity is reconstructed $\sim 1.4\%$ too low with a resolution of 12%. The transverse momentum of the other jet is reconstructed 2.5% too high with a resolution of 25%. In general the resolution and correlations are found to be good.

In figure 4.14 the correlations and resolutions for the x_γ , p_t^{jj} , the rapidity separation between the other jet and the D_{jet}^* and the azimuthal angle difference $\Delta\varphi$ are shown. It can be seen that all distributions are well correlated with the hadron level quantity. An exception is the $\Delta\varphi$ distributions, where the correlation is found to be good only in the region where $\Delta\varphi^{\text{rec/had}} > 120^\circ$. At small $\Delta\varphi$ correlation is smeared and is worse here, but in that region the sample runs out of statistics and no strong conclusions can be drawn. In analogy for the kinematic variables for the jets, the resolutions for the event observables were also checked. In figure 4.14 right column the total resolutions for the x_γ , M_X , p_t^{jj} , and $\Delta\varphi$ are displayed. The x_γ is reconstructed on average 3% too low with a resolution of about 12%. This could be explained with the complex topology of the resolved event. The worst resolution is found to be for the p_t^{jj} of about 31%, where the quantity is reconstructed on average 7% too low.

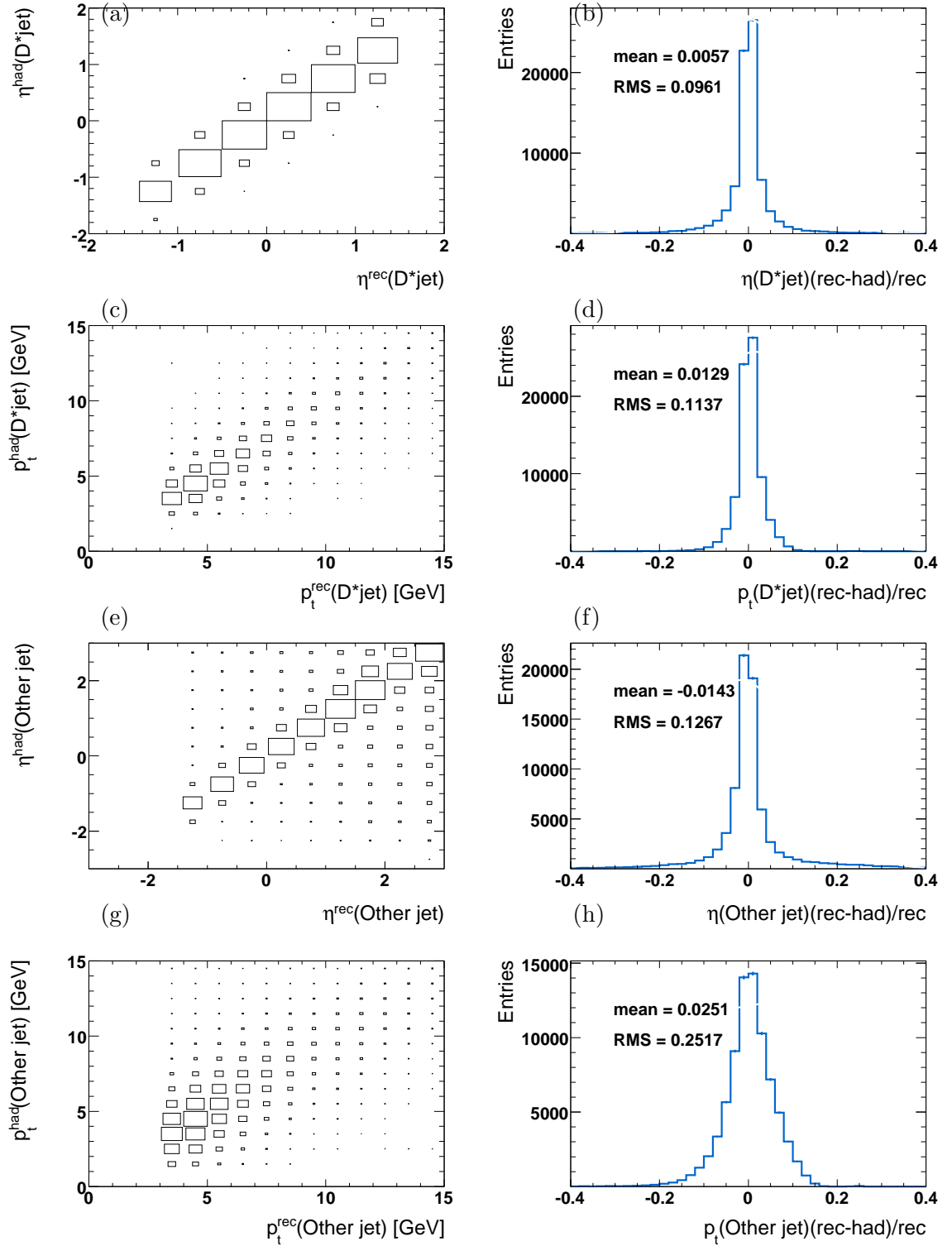


Figure 4.13: The correlation between the hadron level and reconstruction level quantities (left column) and the total resolutions (right column) for η and p_t for the $D^*\text{jet}$ and for the other jet.

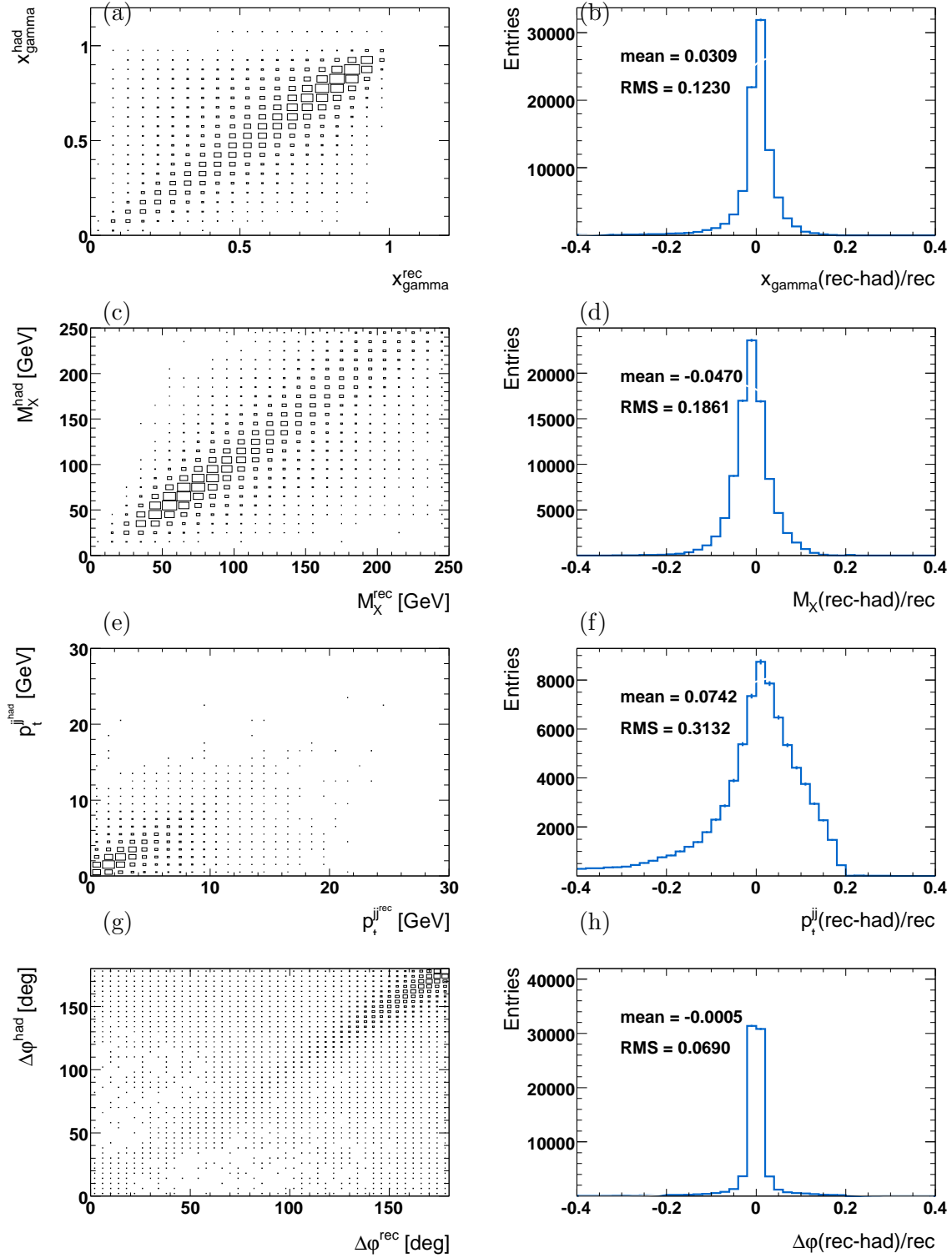


Figure 4.14: The correlation between the hadron level and reconstruction level quantities (left column) and the total resolutions (right column) for x_γ , M_X , p_t^{jj} , $\Delta\eta$ and $\Delta\varphi$.

Chapter 5

Trigger Efficiency

In *untagged photoproduction* (see section 4.2) the electron escapes detection. To trigger an event, an online reconstruction of a D^* meson candidate is performed by the third level of the *Fast Track Trigger* (FTT). The principle of operation of the FTT is described in section 2.2.4.1 and here the studies for understanding of the trigger efficiency and the estimation of the systematic uncertainty due to the trigger efficiency will be presented. There were in total three sub-triggers (ST) devoted to a D^* measurement with three different p_t thresholds. The combination of these ST, the trigger efficiency determination and comparison to a trigger simulation will be discussed in this chapter. The concept of prescale factors used in H1 and terminology on the different levels and trigger bits used in this chapter are given in section 2.2.4.

5.1 Analysis Strategy

The inclusive ep cross section increases towards small virtuality with $\sigma^{tot} \sim 1/Q^4$. This leads to high event rates, which would cause a high dead time in the detector. In addition, the rising $p_t(D^*)$ spectrum towards small transverse momentum and rising combinatorial background, leads to a further increase of the event rates. Therefore, the ST used here were prescaled. There were three ST devoted to a measurement of D^* in photoproduction, namely s55, s53 and s122. The basic difference between them is the cut on the transverse momentum of the D^* candidate applied on the third level. The low-s55 and medium-s53 p_t ST were optimised for stable rate reduction rather than high efficiency while the high p_t s122 ST was optimised for high efficiency. This leads to average prescale factors (PF) of $P(s55) = 2.01$, $P(s53) = 1.33$ and $P(s122) = 1.21$. When only one sub-trigger is used, the correction for the prescale factors in the number of events is done with event weights. The events are weighted with the corresponding PF, at the end the total event weight is calculated by summing the individual weights and hence the total number of events is known:

$$W = \sum_{i=0}^{N_{events}^{recorded}} w_i, \quad N_{events}^{tot} = W$$

In the case of two sub-triggers the determination of the total event weight is done in analogous way in the case when the two ST do not overlap (visualisation of two overlapping triggers is sketched in figure 5.1). When they overlap there are two ways for calculating the total event weight. Commonly used in H1 for such cases [106], referred as the inclusive method and an exclusive method. In the case of combining two overlapping triggers, the principle of the two procedures will be introduced in the following. In figure 5.1 a schematic picture of two overlapping sub-triggers is shown. The area of the two circles represent the event samples where each of the triggers has fired, s1 (region A) and s2 (region B). The overlapping region is denoted as region C. The events from regions A and B are treated as described above. The calculation of the prescale factor for the event sample where both triggers have fired, represented by region C in the figure, is the issue discussed in the following. For the inclusive method, s1 and s2 are ordered in priority. For that case the highest priority is given to the sub-trigger with the lower prescale factor. If the event has been triggered by the higher priority trigger in the overlapping region, then the prescale factor of that trigger is taken as an event weight. But if the trigger's actual bit is zero, then the event is discarded. The lower priority trigger plays a role only for the case when the higher priority trigger is excluded (region B on figure 5.1, if $PF(s1) \ll PF(s2)$). The exclusive method treats the sub-triggers in an equal way, but the events from the overlapping region are always taken no matter which trigger has the actual bit. In both cases the sum of the weights is preserved and is same. But the exclusive method leads to lower statistical uncertainty. Details for the two methods are given in [107].

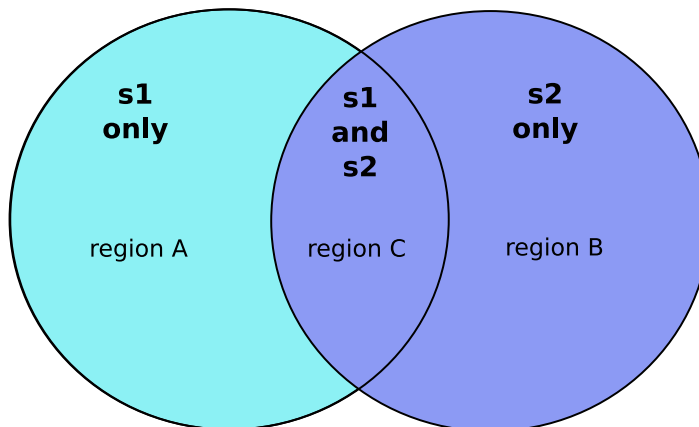


Figure 5.1: An overlap between two triggers.

However in the basis of these methods the two sub-triggers are expected to fire independently of each other and also they are supposed to have the same running periods and

time of operation. As will be described in the following section, this is not applicable here since the three sub-triggers have the same condition on level 1. In a previous inclusive D^* measurement at H1 the phase space was divided into three independent regions of the transverse momentum of the D^* such that none of the triggers overlap [95] (see figure 5.2). The triggering of the event is provided by one of the triggers according to the $p_t(D^*)$ range. This method was approved by the H1 Collaboration and results on inclusive D^* photoproduction were presented at the DIS conference 2008 [108]. Therefore this method was adopted also here and extensive studies were performed. In figure 5.2 the trigger efficiency as a function of the D^* transverse momentum is presented for the three sub-triggers, s55 (purple triangles), s53 (orange circles) and s122 (blue boxes). The efficiency was obtained in the corresponding running periods relevant for the three sub-triggers. The full analysis selection criteria for D^* candidate and a 2-jet pair is required. The inelasticity y_h range was also kept. In addition, a low Q^2 electron with an energy of $E_e > 8$ GeV was required too. No background subtraction was done.

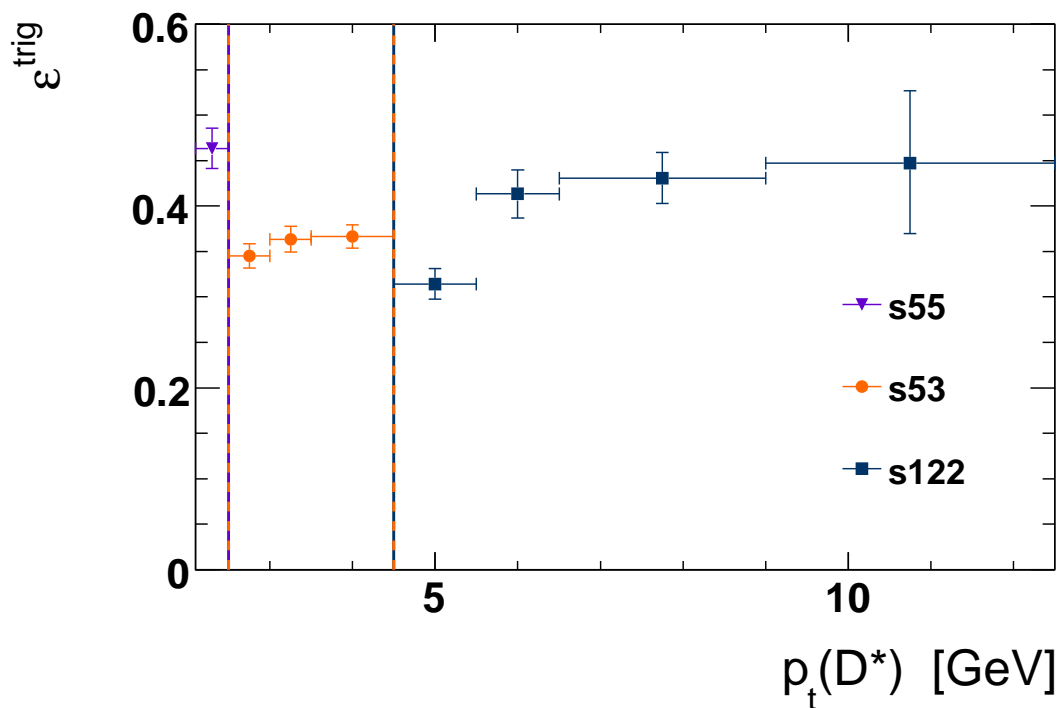


Figure 5.2: The trigger efficiency as a function of the transverse momentum of the D^* for s55 (purple triangles), s53 (orange circles) and s122 (blue boxes). The lines represent the border between the three different sub-triggers.

5.2 Trigger Efficiency Determination

In order to calculate the total cross section of a certain physics process, the total number of events within a given amount of luminosity, has to be known. However, due to various reasons the detector is not expected to record all the events from the process of interest that occurred. By definition, the *trigger efficiency* is the fraction of events that the detector recorded from the total number of the events that happened:

$$\varepsilon^{trig} = \frac{N_{\text{recorded}}}{N_{\text{happened}}} \quad (5.1)$$

The number of events N_{recorded} is provided by a fired sub-trigger (ST)¹. Since the N_{happened} is unknown, the trigger efficiency has to be estimated in a different way. Instead a *monitored data sample* is normally used. If a completely independent ST, built from trigger elements which do not contain any information from the detector components used to build ST definition that *recorded* the sample N_{recorded} is used, then for the relation (5.1) the following is valid:

$$\varepsilon^{trig} = \frac{N_{\text{recorded}}}{N_{\text{happened}}} = \frac{N_{\text{recorded}} \wedge \text{monitored}}{N_{\text{monitored}}} \quad (5.2)$$

where the *monitored* data sample **must** be recorded with an independent sub-trigger. Considering that this measurement is in photoproduction, the event rates do not allow the design of an inclusive photoproduction monitor sub-trigger. Instead a data sample with similar event topology can be used. Good candidates are low Q^2 DIS events. The scattered electron is detected under small scattering angle, but the distribution of the particles in the central part of the detector is similar to the one in photoproduction.

In order not to misinterpret the effects from the prescaling as an inefficiency the *triggered* sample was defined by the *raw* trigger bit. The event was kept by the monitored sub-trigger anyhow since the monitor sub-triggers were taken in their *actual* bit. The trigger efficiency in this measurement was defined as:

$$\varepsilon^{trig} = \frac{raw^{ana} \wedge ac^{moni}}{ac^{moni}} \quad (5.3)$$

The efficiencies at the different levels were determined as follows. For the monitor sample for L1 an independent DIS data sample was used. For the L2 (L3 respectively) the data sample from L1 (or L2 respectively for L3) was used as a monitor sample such that the pure efficiency of the investigated level can be studied. Such way, the total trigger efficiency is then defined as the multiplication of the three levels.

¹The definition of the term sub-trigger as well as the concept of the H1 triggering is given in section 2.2.4.

5.2.1 Sub-trigger Definitions

A typical D^* event is characterised with many tracks in the central region. Therefore already, on L1, online track reconstruction is performed and the track multiplicity is calculated for given transverse momentum thresholds. The three sub-trigger used here have the same L1 condition, explicitly:

$$\text{FTT_mul_Ta} > 5 \ \&\& \ \text{FTT_mul_Tc} > 2 \ \&\& \ \text{FTT_mul_Td} > 1 \ \&\& \ \text{FTT_mul_Te} > 0 \ \&\& \quad (5.4)$$

$$\text{CIP_sig} > 2 \ \&\& \ \text{CIP_mul} > 4 \quad (5.5)$$

where all trigger elements are combined with a logical AND.

The CIP trigger element, `CIP_sig` provides an information about the amount of tracks pointing to the interaction vertex. The requirement `CIP_sig > 2` means that the number of tracks pointing to the interaction vertex is at least two times larger than the number of tracks pointing to the backward or forward direction. The `CIP_mul` is the multiplicity of tracks as seen by the CIP. More details for the CIP trigger can be found in [73]. In addition to the CIP trigger conditions a number of `FTT_mul` conditions are required. All of them mean track multiplicities with different thresholds of the tracks transverse momenta and are listed in table 5.1. For example `FTT_mul_Td > 1` means that there are at least two tracks with $p_t > 900$ MeV seen on L1.

L1 name	threshold/description
<code>FTT_mul-Ta</code>	100 MeV
<code>FTT_mul-Tc</code>	400 MeV
<code>FTT_mul-Td</code>	900 MeV
<code>FTT_mul-Te</code>	1800 MeV
<code>CIP_sig</code>	$2 \cdot (N(fwd) + N(bwd)) < N(cen)$
<code>CIP_mul</code>	$N(cen) + N(fwd) + N(bwd) > 10$

Table 5.1: Definitions of the trigger elements on level 1.

On the second level (L2) the time for decision is significantly larger compared to L1, which allows better momentum reconstruction, therefore it is used for validation of the L1 condition but with more precise information provided by the L2FTT. It is also used for further rate reduction.

The trigger requirements on the L2 are:

$$\text{FTT_et_20} > 0 \ \&\& \ \text{FTT_mul_Te} \geq 2 \ \&\& \ \text{FTT_zvtx_hist} \geq 2 \ \text{for s55} \quad (5.6)$$

$$\text{FTT_et_26} > 0 \ \&\& \ \text{FTT_mul_Te} \geq 2 \ \&\& \ \text{FTT_zvtx_hist} \geq 2 \ \text{for s53} \quad (5.7)$$

$$\text{FTT_mul_Te} \geq 2 \ \&\& \ \text{FTT_zvtx_hist} \geq 2 \ \text{for s122} \quad (5.8)$$

where the `FTT_mul_Te` TE has a different p_t threshold than at L1, here 800 MeV is used. The `FTT_zvtx_hist` condition, provides information for the z_{vtx} position reconstructed from extrapolating the L2 tracks to their origin. The event is kept if the *quality* of the vertex found is satisfactory (in this case given by the digit 2, `FTT_zvtx_hist`>=2, for details see [89]). The condition `FTT_et` provides the scalar sum of transverse momenta of all the tracks seen in the online track reconstruction. This condition was applied in order to provide reasonable input rates for L3, considering the low transverse momentum and rising combinatorial background towards small $p_t(D^*)$ for the ST s55 and s53. All the L2 trigger elements with their thresholds are summarised in table 5.2.

L2 name	threshold/description
<code>FTT_mul_Te</code>	800 MeV
<code>FTT_et_20</code>	5 GeV
<code>FTT_et_26</code>	6.5 GeV

Table 5.2: Definitions of the trigger elements on level 2.

On the third level (L3), the tracks are combined into D^* candidates, using the charge and momentum information from L2. Masses are assigned to the tracks (mass hypothesis) and a D^* candidate is selected if its Δm falls in the corresponding window (see table 5.3). In addition, different p_t cuts were applied on the D^* candidate. The main L3 cuts are listed in table 5.3.

ST name	threshold	Δm Cut	Run Number
s55	$p_t > 1.5 \text{ GeV}$	$\Delta m \leq 180 \text{ MeV}$	489125
s53	$p_t > 2.5 \text{ GeV}$	$\Delta m \leq 180 \text{ MeV}$	482535
s122	$p_t > 4.5 \text{ GeV}$	$\Delta m \leq 280 \text{ MeV}$	477240

Table 5.3: p_t thresholds of the different sub-triggers and the Δm cuts applied on the third level.

5.2.2 Monitor Trigger Definitions

The trigger efficiency is determined using an independent data sample. For that purpose events with similar topology but triggered with a completely independent ST were used. A good candidate for such events are low Q^2 events containing D^* meson candidates triggered by the electron candidate in the backward calorimeter of H1 SpaCal. In this measurement the s0 and s3 ST were used. They fire if an electron candidate with energy above a certain energy threshold (6 GeV and 9 GeV correspondingly for s0 and s3) is detected in the SpaCal. This information is provided by the `SPCLe_IET` trigger elements. In addition a radius cut around the beam pipe of 30 cm and 20 cm, respectively, was applied to reduce the event rates. Details on the inclusive electron trigger are given in [109]. These trigger conditions are free of

any information from the central tracker, therefore they can be used to determine the trigger efficiency of the D^* triggers.

5.3 Trigger Efficiency Description

The goal of this study was to achieve satisfactory agreement between the trigger efficiency obtained from data and from the FTT simulation `fttemu`. `fttemu` is a software emulation of the FTT trigger elements and was implemented in the official H1 detector simulation. With the `fttemu`, a fired trigger can be required also for the MC events. Using the trigger simulation, the trigger efficiency can be taken into account when calculating the correction factors to hadron level from the MC directly (see section 7.1). For these studies, a D^* signal RAPGAP MC is used in the DIS kinematic range, in order to be able to compare trigger efficiency from data, obtained with a DIS monitor sample. All reconstruction cuts were applied and an electron is reconstructed with $E_e > 8 \text{ GeV}$ and the photon virtuality was explicitly required to be larger than $Q_{\text{rec}}^2 > 0 \text{ GeV}$. Since the three sub-triggers s55, s53 and s122, are devoted to untagged D^* photoproduction and D^* meson candidates are explicitly required on the trigger level, the trigger efficiency is expected to depend on the kinematics of the D^* meson candidate, $p_t(D^*)$ and $\eta(D^*)$. In addition on L2, a cut on the scalar sum of the transverse momenta of the tracks is also required E_T^{sum} , therefore in the following all efficiencies will be shown for these particular quantities.

- **Level 1**

As a start, the first level (L1) will be considered. The trigger efficiency obtained from data is compared to the trigger efficiency obtained from the MC as shown in figure 5.3 for different quantities. In figure 5.3 (a) and (b) the transverse momentum and rapidity of the D^* meson candidate, the sum of the momenta of all central tracks as seen in the offline reconstruction² (c) and by the online track reconstruction (d) are shown. As a function of the D^* quantities $p_t(D^*)$ (a) and $\eta(D^*)$ (b), the efficiency obtained from data is well above 80% and relatively flat. A discrepancy is observed only in the very backward η where the difference between data and MC is of the order of 7%. However, agreement between data and MC for these two quantities is satisfactory. As a function of E_T^{sum} , a rising trigger efficiency towards large E_T^{sum} is observed where the efficiency drops down to 60% for values of $E_T^{\text{sum}} \approx 7 \text{ GeV}$. This effect is also seen in the online $E_T^{\text{sum}} < 7 \text{ GeV}$ although not so well pronounced. This dependence of the trigger efficiency could be explained with the fact that in the L1 condition (see equation (5.4)) tracks with at least a total transverse energy of 2.4 GeV in the trigger elements `FTT_mu1` are required. This leads to an indirect requirement on the sum of the tracks. Note that

²Offline track in this analysis are the classified central tracks which are fitted to the primary vertex as provided from the [100] class `H1PartSelTracks`. The online tracks are the one provided by the online track reconstruction, the information was taken directly from the data bank `TT2T`.

the L1 conditions of the three triggers are the same and therefore the comparison, for $\eta(D^*)$ and E_T^{sum} is possible. The comparison between trigger efficiency obtained from the data and MC is satisfactory.

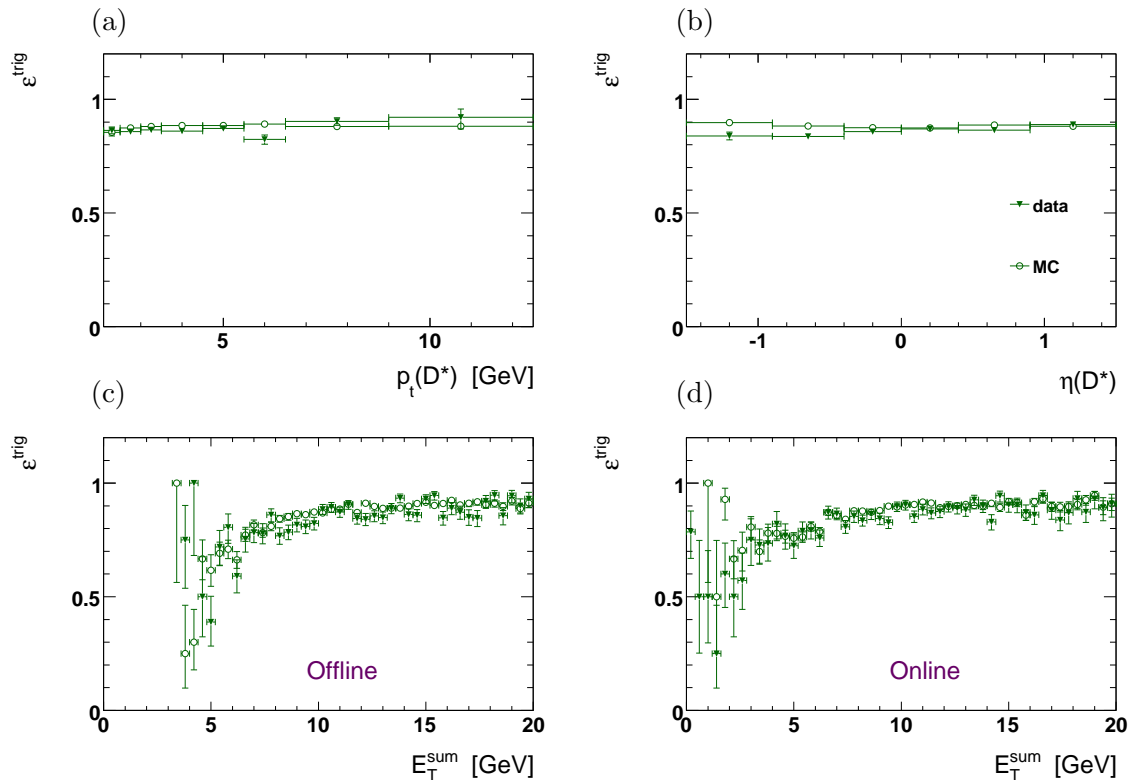


Figure 5.3: The L1 trigger efficiency from data (filled triangles) and from MC (open circles) as a function of $p_t(D^*)$, $\eta(D^*)$, the sum of the tracks momentum E_T^{sum} (offline, left and online right).

- **Level 2**

Since the three ST have the same trigger elements (FTT_mul_Te and FTT_zvtx_hist, see equation (5.7)-(5.8)) these elements will be shown together for the three triggers. In figure 5.4 the trigger efficiency of the trigger elements FTT_mul_Te (a-d) and FTT_zvtx_hist (e-h) as a function of $p_t(D^*)$, $\eta(D^*)$ and E_T^{sum} (online and offline) is presented. For the $p_t(D^*)$ (histogram (a)) and $\eta(D^*)$ (histogram (b)) the trigger efficiency is nearly flat and above 90%. The `fttemu` simulation reproduces the trigger efficiency almost perfectly. The trigger efficiency as a function of E_T^{sum} for the FTT_mul_Te trigger element (figure (c) and (d)), rises towards large E_T^{sum} , where in contrast to the efficiency at L1, the rise is better visible in the online case. The maximum of the efficiency is reached at $E_T^{\text{sum}} \approx 8$ GeV. All trigger efficiencies for the FTT_zvtx_hist trigger element are flat, close to 100% and well described by the MC.

In figure 5.5 the trigger efficiency of the trigger elements FTT_et is shown for the sub-

triggers s55 (FTT_et_20 figures (a-d)) and s53 (FTT_et_26 figures (e-h)). For s55 (or FTT_et_20), the difference between data and MC is of the order of 2-5%, best visible as a function of the D^* transverse momentum $\varepsilon(p_t)$ (a). For the pseudorapidity, histogram (b), the efficiency is approximately flat with a slight increase towards the forward direction. Due to the limited p_t range of this sub-trigger as well as the short running period, the statistical uncertainties here are significant. The discrepancy between data and MC in $\eta(D^*)$ (for example) is consistent with statistical fluctuations. For E_T^{sum} (in the online case) the trigger efficiency follows a step function with a threshold at 5 GeV, which is also the trigger threshold. The offline distribution is smeared due to a better offline track reconstruction. A similar behaviour is also visible for the s53 (or FTT_et_26). The difference between the data and MC efficiency is about 5%. The online E_T^{sum} efficiency is a step function with a threshold at 6.5 GeV. In the offline case, discrepancies at $E_T^{\text{sum}} < 10$ GeV are observed.

The low efficiency at small offline E_T^{sum} and the strong rise of the efficiency at the threshold region motivate new offline E_T^{sum} cuts for the sub-triggers s55 at 5.5 GeV and s53 at 7 GeV (500 MeV more with respect to the online trigger condition– see table 5.2) in order to avoid the critical threshold regions. For consistency the E_T^{sum} cut was also applied on the s122 with a value of 6 GeV. Here the offline definition of E_T^{sum} is used. The resulting trigger efficiency is shown in figure 5.6. It can be seen that the difference between data and MC is smaller and the quantities are now better described (e.g the offline E_T^{sum} for s53, histogram (g)). For completeness the effect of the new E_T^{sum} cut is also shown for L1 in figure 5.7 (a)-(d) and the overall L2 in figures (e)-(h).

- **Level 3**

The third level trigger efficiency was calculated after applying the E_T^{sum} cuts as discussed above. In figure 5.8 the L3 efficiency is presented. It can be seen that the p_t regions of s55 and s122 the efficiency obtained from data and MC is smaller, while for the s53 the efficiency obtained from the MC is significantly larger than obtained from the data. The difference goes up to 15%. A similar tendency is also seen in the first bin for the s122 sub-trigger. The difference can be due to missing combinatorial background in the MC simulation while this background is significant in the data. Of particular interest is the trigger efficiency for signal events only. But the statistics in the monitor sample is very low and any signal extraction procedure is insufficient. One option would be to use a fully inclusive MC simulation including the background. Within the H1 collaboration, an estimate on how much the statistic for such MC would be, was done [110]. It was argued that the large statistics needed would require too much computing time and resources.

- **Overall**

The overall trigger efficiency was taken from the product of the three levels. The discrepancy between the trigger efficiency on L3 for the s53 is transferred to the overall trigger efficiency. The total trigger efficiency from data compared to the FTT simulation can be seen in figure 5.8. Since this is the efficiency which is finally used to correct the data for trigger efficiency, the focus of the study is on describing this level.

5.3.1 Reweighting in $\eta(D^*)$ for s53

Since the difference between the trigger efficiency obtained from data and MC for the sub-trigger s53 is not acceptable, a reweighting procedure was introduced, in order to downscale the MC such that it fits the trigger efficiency obtained from data. The FTT hit efficiency depends on the polar angle of the tracks [111]. Charged particles with polar angle away from 90° deposit more charge in the CJC chambers. The size of the effect on the efficiency depends on many parameters (e.g gas gain) which is difficult to model in the detector simulation and might be not fully sufficient in the MC. It was found that the `fttemu` inefficiency depend on the polar angle of the particles. Therefore a variable which is appropriate to reweight the MC is the pseudorapidity $\eta(D^*)$. The function to reweight the detector level MC was derived from the ratio between the trigger efficiency obtained from data divided with the trigger efficiency obtained from the MC. The ratio was fitted with a polynomial function of the first order (figure 5.9 (a)). The factor is applied to the MC and a comparison with the trigger efficiency in data was performed again. In figure 5.9 (b-e) the trigger efficiency obtained from data and from MC is compared for the reweighted MC sample. It can be seen that the differences between data and MC are now small and only for the p_t bin 4.5–5.5 GeV (belonging to s122) a difference remains. The trigger efficiency as a function of the variables used for the differential cross sections were also estimated. In figure 5.10 the trigger efficiency as a function of different variables (see section 1.3) obtained from data and MC is shown. After reweighting the overall the trigger efficiencies are flat and the agreement between data and MC is very good.

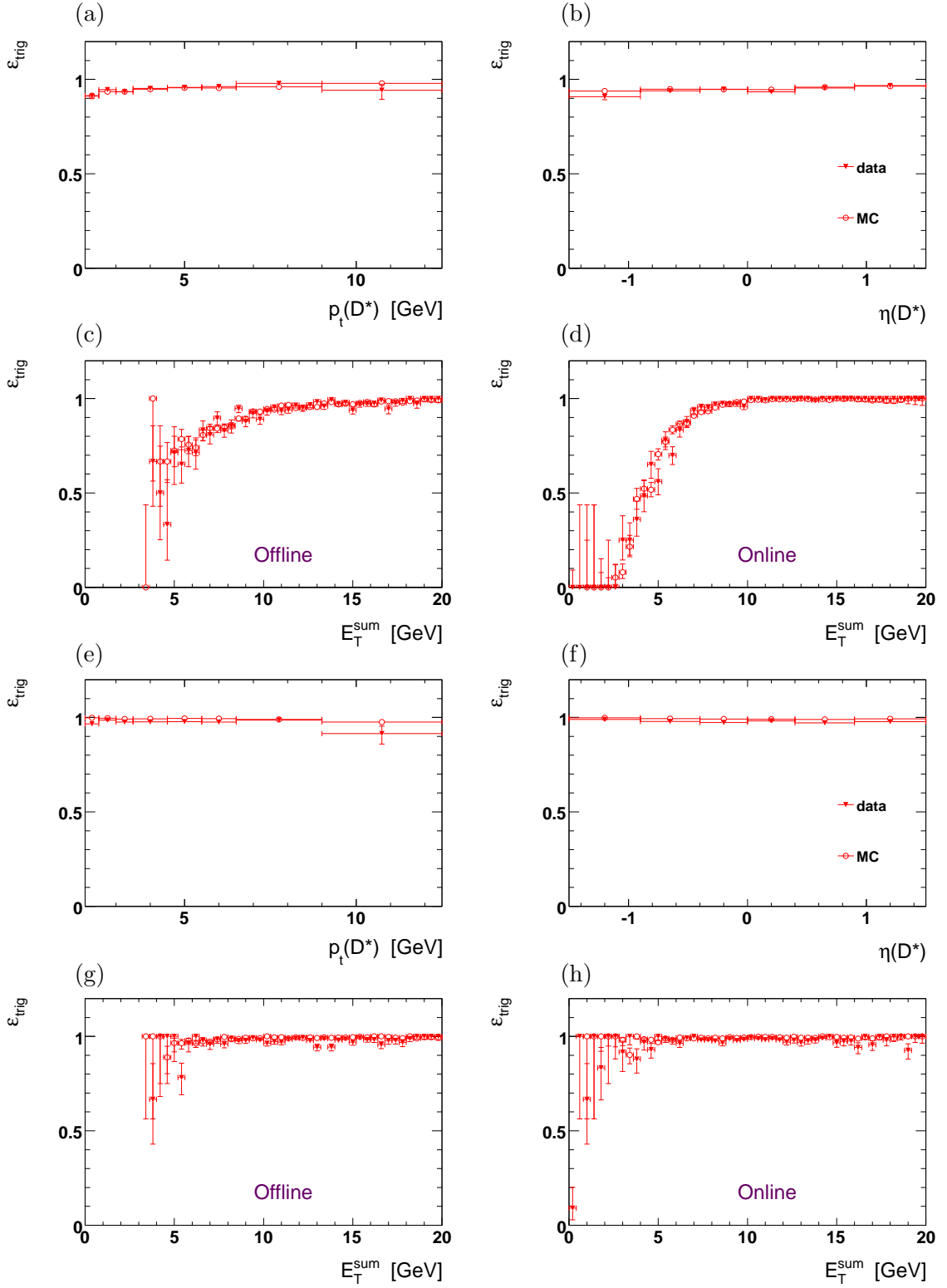


Figure 5.4: The trigger efficiency of fttmulte (a-d) and zvtxhist (e-h) as a function of $p_t(D^*)$, $\eta(D^*)$ and the online and offline values for E_T^{sum} .

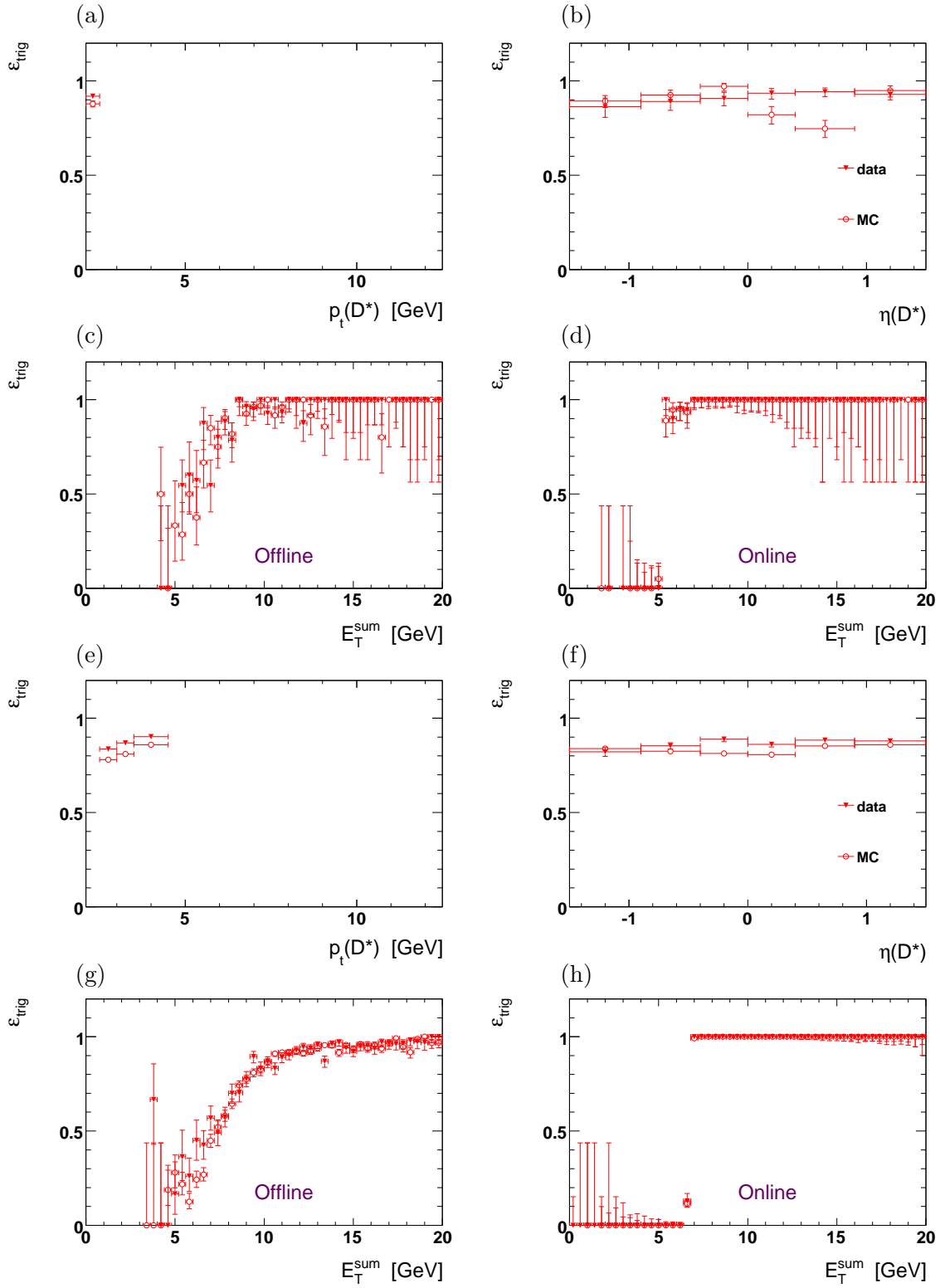


Figure 5.5: The trigger efficiency of et20 (a-d) and et26 (e-h) as a function of $p_t(D^*)$, $\eta(D^*)$ and the online and offline values for E_T^{sum} .

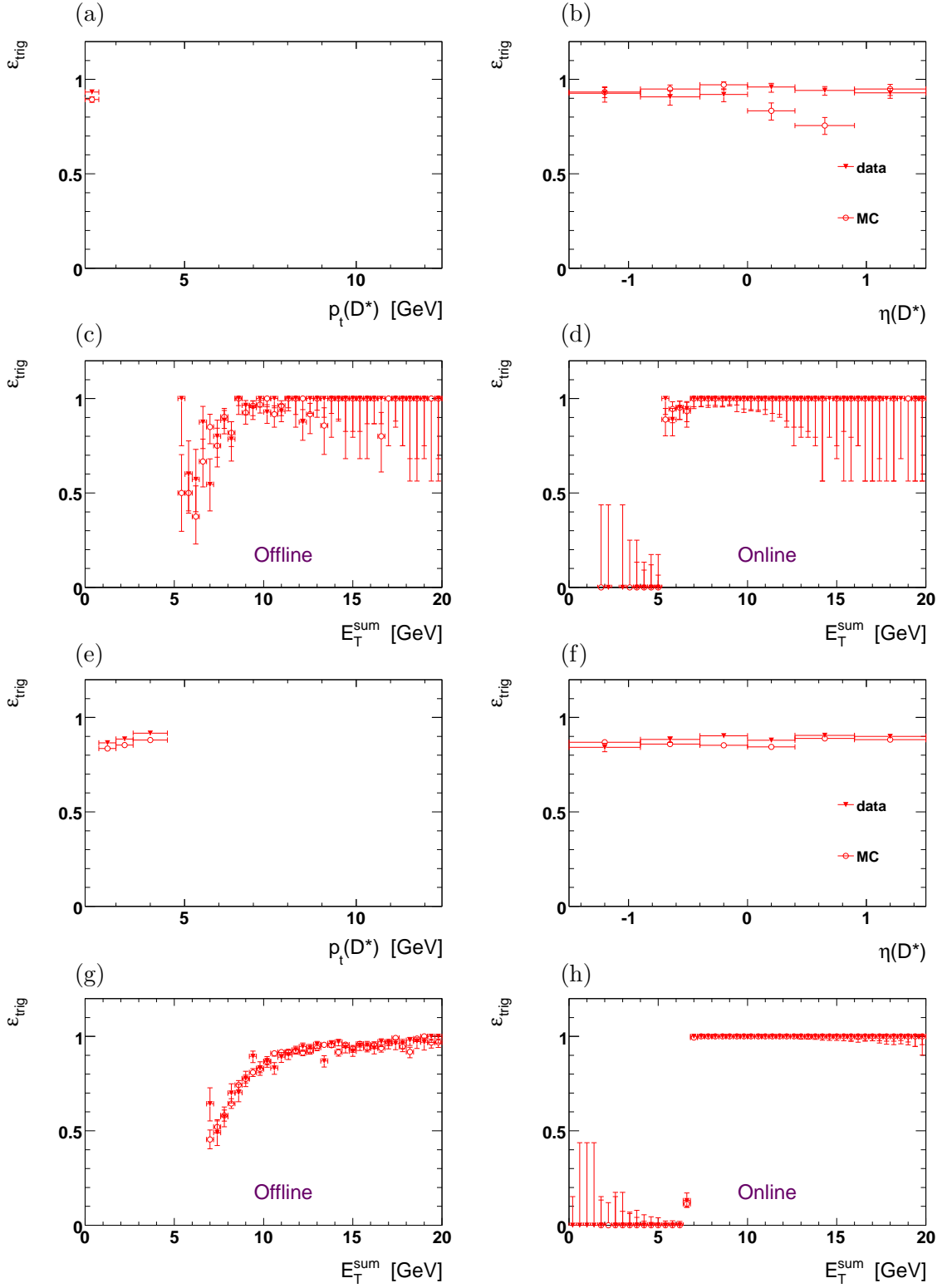


Figure 5.6: The trigger efficiency of et20 (a-d) and et26 (e-h) as a function of $p_t(D^*)$, $\eta(D^*)$ and the online and offline values for E_T^{sum} after applying the offline E_T^{sum} cuts.

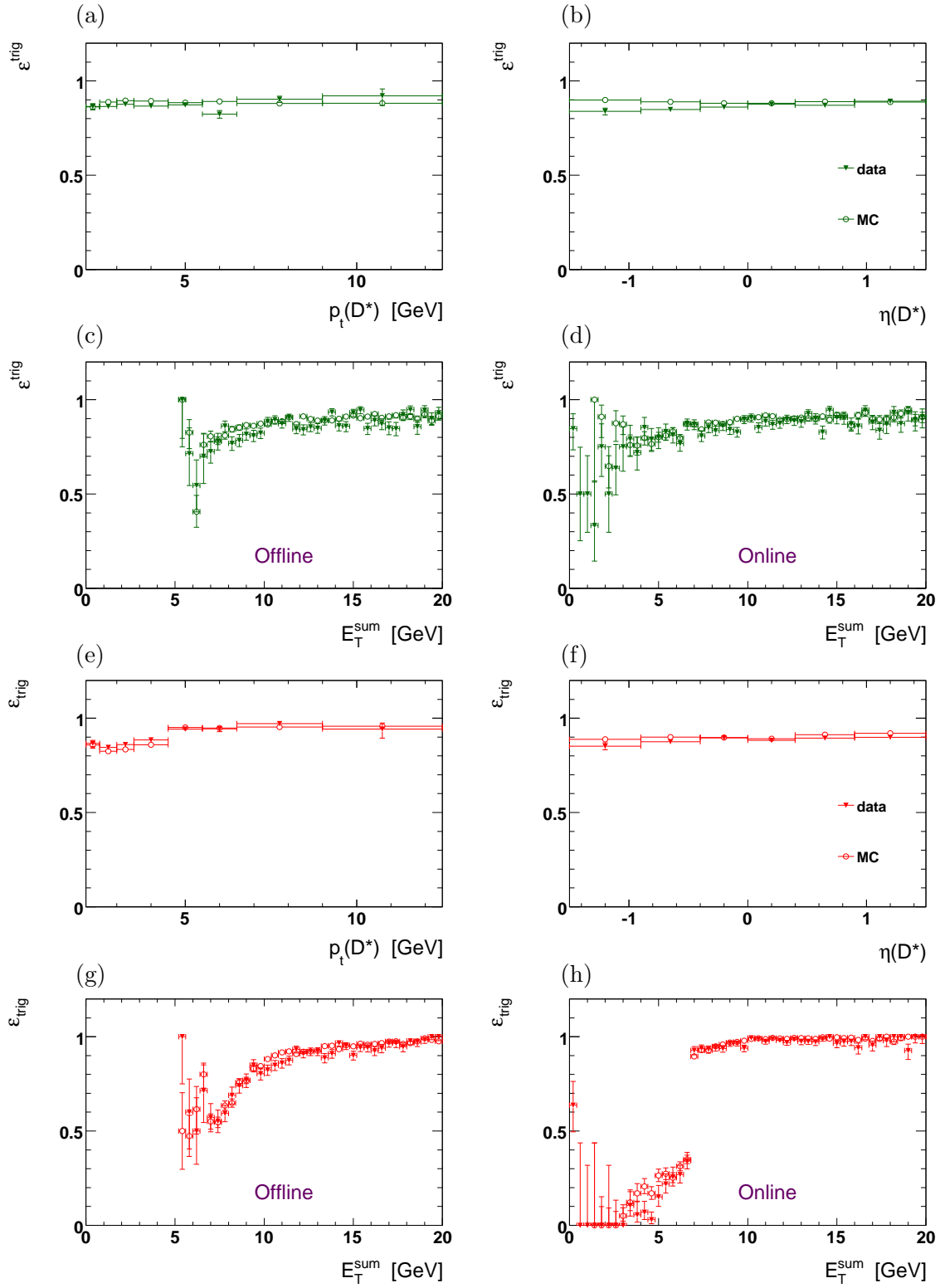


Figure 5.7: The trigger efficiency of L1 (a-d) and overall L2 (e-h) as a function of $p_t(D^*)$, $\eta(D^*)$ and the online and offline values for E_T^{sum} after applying the offline E_T^{sum} cuts.

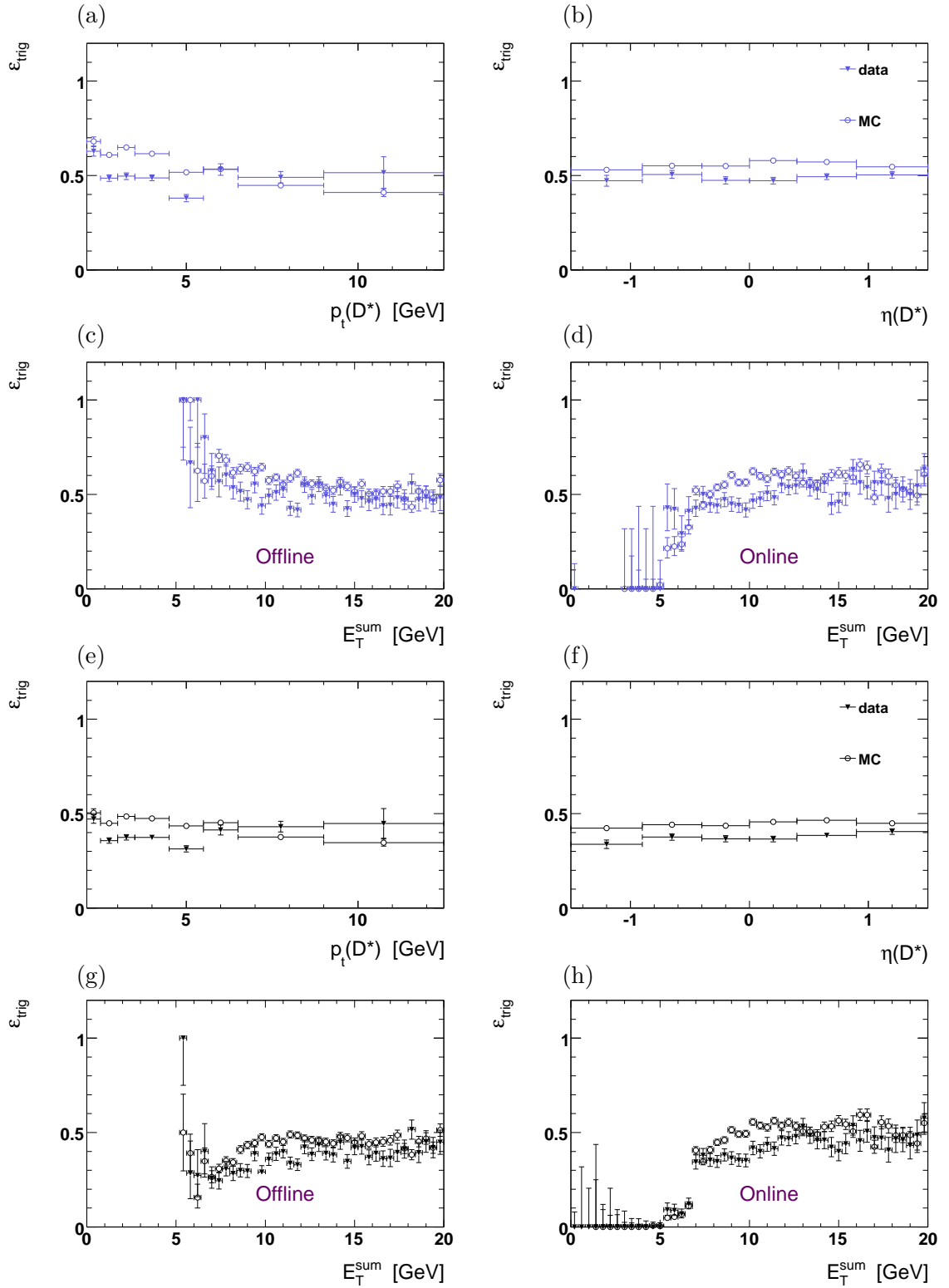


Figure 5.8: The L3 trigger efficiency (blue markers) (a-d) and the overall trigger efficiency (black markers) (e-h) from data (filled triangles) and from MC (open circles) as a function of $p_t(D^*)$, $\eta(D^*)$, the sum of the tracks momentum E_T^{sum} .

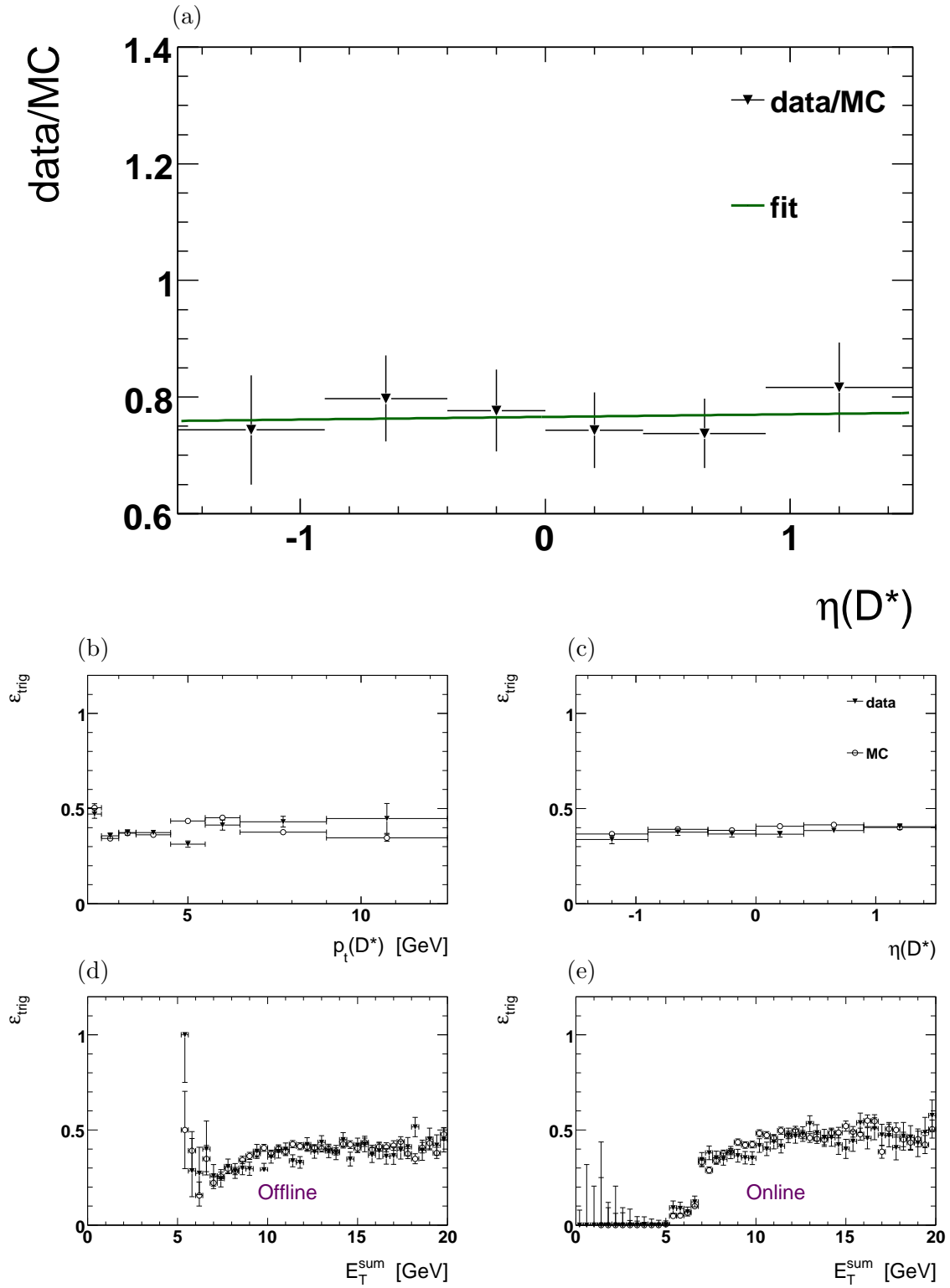


Figure 5.9: The reweighting function for the trigger efficiency (a) and the total trigger efficiency for the reweighted s53 region, comparison between data (filled triangles) and MC (open circles).

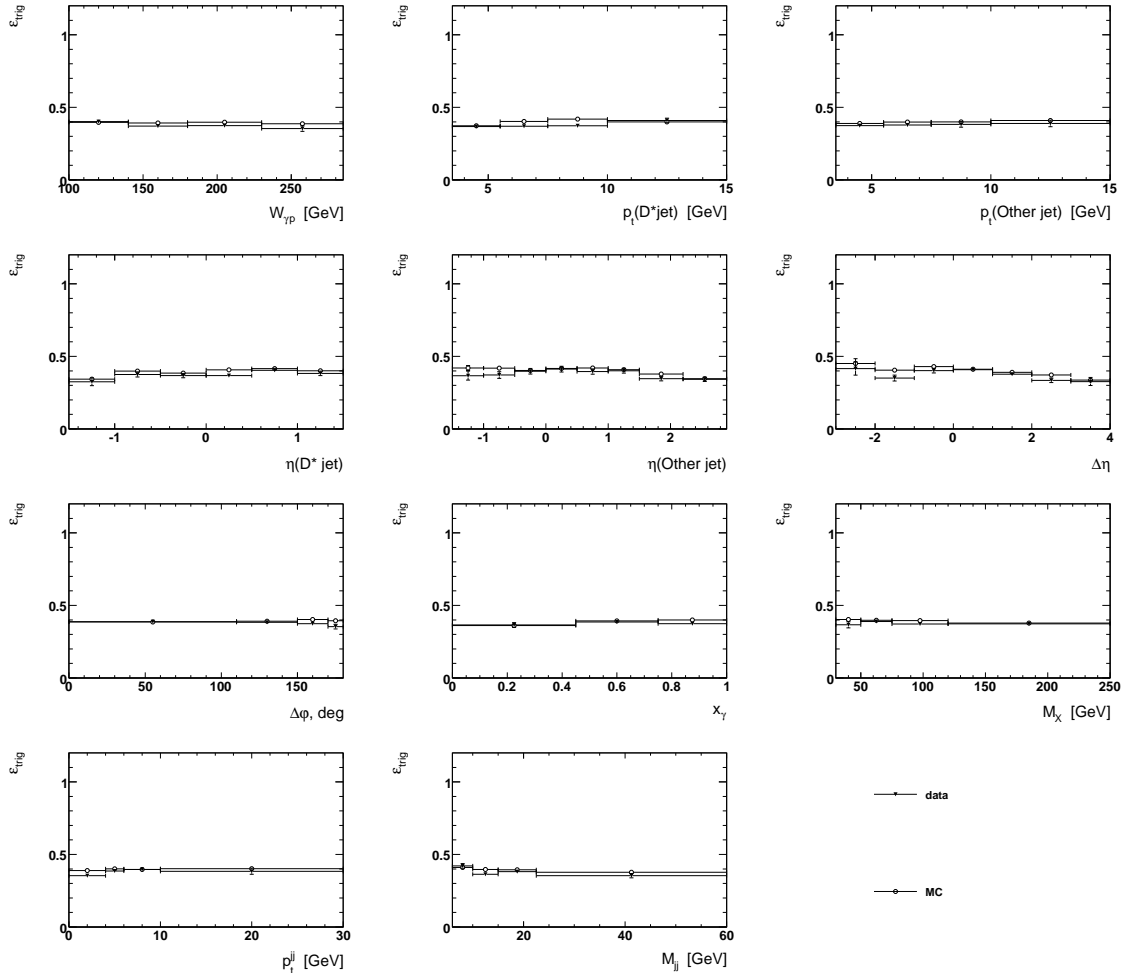


Figure 5.10: Comparison between the total trigger efficiencies of different quantities relevant for the final differential cross section measurement as obtained by data and reweighted for the s53 region MC.

Chapter 6

Systematic Uncertainties

The systematic uncertainties of the measured cross section in this measurement were estimated by varying the Monte Carlo (MC) simulations or with dedicated studies with data. The systematic uncertainties were studied separately for the bin-to-bin correlated and bin-to-bin uncorrelated case and were measured for each bin of the differential cross sections. The resulting uncertainties were added in quadrature together with the statistical uncertainties to obtain the total uncertainty of the measurement. In the following the correlated and the uncorrelated systematics will be presented.

6.1 Uncorrelated Systematic Uncertainties

- **Track Finding**

During the track reconstruction process it happens that a track is not identified by the algorithms used for the reconstruction. The track finding uncertainty is one of the largest systematic uncertainties of this measurement. At high momentum of the tracks, the LAr calorimeter part of the detector can be used for further information. A dedicated study with MC was performed [91] and it was found that the difference between data and MC at high momenta is known up to 2% per track or 6% per D^* candidate.

At low momenta the track reconstruction relies only on one detector component, the CJC. For the uncertainty determination another detailed study was performed [112]. It was shown that the measurement of the tracks at low momenta is known to a precision of 2% per track. A global uncertainty of 6% in total for the whole phase space for the tracks was assigned.

- **Primary Vertex Fit**

The reconstruction of the position of the track origin has a direct influence on the measured distributions. Therefore the efficiency of vertex finding has to be taken into account. A detailed study with data and MC was performed in [113].

To estimate this efficiency two types of data and MC samples were used. The Δm histogram is filled with tracks which are fitted to the primary vertex and tracks which were not fitted to the primary vertex. From these two samples the primary vertex fit efficiency is estimated $\varepsilon^{\text{vtx}} = N(D^*)_{\text{vertex}}/N(D^*)_{\text{non-vertex}}$ and a difference of 1% between data and MC is observed which is used in this analysis.

- **Luminosity Measurement**

The data in this analysis were taken in the 2006/2007 HERA running period. During this period an increase in the event yield was observed in all H1 analysis. Up to the present moment this increase is not understood and therefore a global uncertainty due to the luminosity measurement of 5% is assigned.

- **Branching Ratio**

To measure the inclusive D^* meson production cross section the measured cross section for the golden decay channel $D^* \rightarrow K\pi\pi_s$ was corrected with the branching ratio of 2.63% for this channel. The value was taken from the Particle Data Group (2008) [93] and is known to a precision of 1.5%.

- **Signal Extraction**

As discussed in section 3.2.2 the number of D^* mesons was determined with a fit of a function to the Δm distribution. This implies an assumption of the shape on the function used for the fit. Here, the *Crystal Ball* function was used for the signal and a power function for the background. The choice of these functions has a direct impact on the number of particles and therefore an uncertainty of the function choice has to be assigned. To estimate this uncertainty two different independent functions were chosen. In [95] this uncertainty was determined for inclusive D^* production in photoproduction and it was shown that this uncertainty is up to 1.2%.

- **Reflections**

The D^* meson was reconstructed in the golden decay channel $D^* \rightarrow D^0\pi_s \rightarrow K\pi\pi_s$. However there are various decay modes of the D^0 where it decays into other charged mesons (see table 3.2):

$$D^0 \rightarrow (K^\pm K^\mp, \pi^\pm \pi^\mp, \pi^\pm \pi^\mp \pi^0) \quad (6.1)$$

These decay products also contribute to the Δm distribution. These contributions are called *reflections*. To estimate the fraction of these contributions a separate MC sample was used in [91] where the golden decay channel was excluded from the MC sample and only reflections were used. It was shown that these contributions amount to 1% which was assigned as a global uncertainty in this analysis.

- **DIS Background**

Since this measurement is in the *untagged photoproduction* regime where the electron escapes detection in the beam pipe, the photoproduction event (see table 4.1) criteria might be not sufficient enough to reject all possible contributions from events with high virtuality ($Q^2 \gg 0 \text{ GeV}^2$). Such contributions have to be estimated and a systematic uncertainty has to be assigned.

The contribution from DIS background events to the photoproduction sample can be obtained with a DIS Monte Carlo (MC) sample. It was observed that the amount of DIS events which survive the photoproduction selection criteria is $\sigma_{DIS} = 26.15 \text{ pb}$ which leads to $\Delta\sigma_{DIS} = 0.3\%$.

- **The D^0 Mass Cut**

In order to reduce the combinatorial background and to be able to select the actual D^* mesons, a cut of 80 MeV around the mass of the D^0 candidate, $m_{D^0} = m(K\pi)$ was applied. In order to estimate the actual fraction of real D^* mesons lost due to this cut, the following study was done.

A cut around the nominal Δm position was applied and the cut on m_{D^0} was relaxed. Then the m_{D^0} was plotted in bins of $p_t(D^*)$. These mass resonances were fitted with a Gaussian function. Once the parameters σ and μ of the Gaussian are known, the integral of the function can be calculated. In figure 6.1 (a) the mean value and the width from the Gaussian fit to the m_{D^0} distribution is presented. It is observed that the mean position of the peaks are centred very well around the nominal mass of the D^0 meson $m_{D^0} = 1.86 \text{ GeV}$ (illustrated on the figure with a pink solid line). The widths are well within the 80 MeV cut which was applied (the dashed pink lines). The relative loss (L_{rel}) due to the cut can now be calculated according to equation (6.2) where erf is the error function which is encountered in the normal distribution integration. The obtained relative loss is presented in figure 6.1 (b). It is well below 1% except for the highest two $p_t(D^*)$ bins where the fit uncertainty also becomes sizable. Therefore a global uncertainty of 1% is applied.

$$L_{rel} = 1 - erf\left(\frac{1}{\sqrt{2}} \cdot \frac{80 \text{ MeV}}{\sigma \text{ MeV}}\right) \quad (6.2)$$

6.2 Correlated Systematic Uncertainties

- **Model Uncertainty**

The cross section measurement is directly influenced by the MC model which is used to determine the reconstruction efficiency. For the final cross sections the reconstruction efficiencies were varied between both, as obtained by PYTHIA and as obtained by CAS-

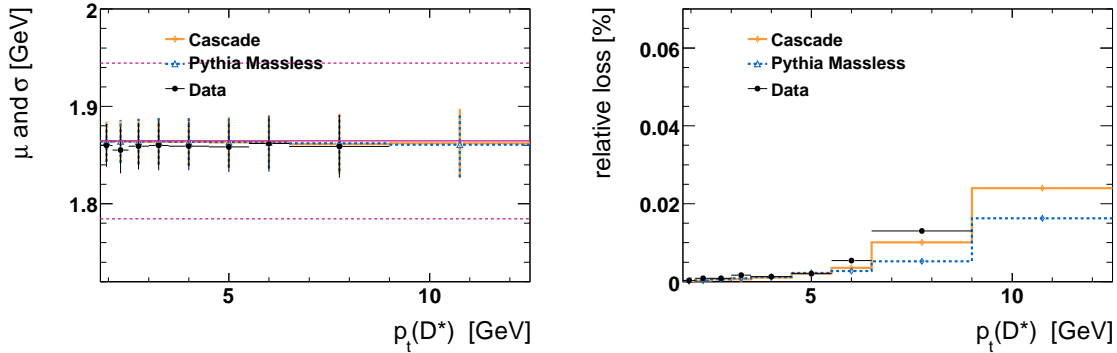


Figure 6.1: The width and the mean of the m_{D^0} in bins of $p_t(D^*)$. The central line presents the nominal position of the D^0 mass taken from the PDG and the dashed lines present the ± 80 MeV cut (a). The relative loss due to the cut of 80 MeV around the m_{D^0} as a function of $p_t(D^*)$ (b).

CADE (see section 7.1). To estimate the uncertainty due to the model the deviations of the final cross section from the cross sections obtained with PYTHIA and CASCADE independently were studied. In figure 6.2 the relative deviation from the measured cross section as a function of the variables important for the final differential cross sections are presented. The blue area presents the deviations of the measured cross section from the one obtained with CASCADE and the pink area is the one obtained from PYTHIA. For comparison the relative statistical uncertainty is also shown with black markers and a line at 5%. Typically the uncertainties are well below 5% and rarely they exceed the statistical uncertainty of the measurement.

- **Trigger Efficiency Uncertainty**

The uncertainty of the total cross section due to the trigger efficiency was estimated with the difference of the total trigger efficiencies between data and the FTT simulation $\Delta \varepsilon_{trig}^{tot} = \varepsilon_{trig}^{data} - \varepsilon_{trig}^{mc}$ and it amounts to $\Delta \sigma_{trig}^{tot} = 3.1\%$. However, the uncertainties of the measured trigger efficiency from data as a function of the cross section variables are very large and the agreement between data and MC cannot be used to estimate the differential uncertainties on the measured cross sections. Instead a more conservative approach was applied here. The uncertainty due to the trigger efficiency in the differential cross sections was taken as the relative uncertainty on the trigger efficiency itself as seen in data. In figure 6.3 the relative uncertainty on the cross sections as a function of the measured variables are presented. The blue area presents the negative error of the trigger efficiency, the pink area presents the positive error of the trigger efficiency and the violet line is at 5%. For comparison the relative statistical uncertainties are also shown with the black marker.

- **Energy Scale Uncertainty**

The so called *particle candidates* are measured in the LAr calorimeter and partly in the tracking system of the H1 detector. Matching between clusters and tracks is performed such that double counting of energies are avoided and best precision of the particle four-vector is achieved. These informations then goes into the event variables determination and in the jet finding procedure. The precision of the measured energy in the calorimeter after the calibration is known to level of 2% [103]. Therefore in order to estimate the uncertainty of the measurement due to the energy measurement, the four vectors of the particles were shifted with $\pm 2\%$. The effect of this procedure is that the cross section is increased when the four vectors are shifted by -2% and decreased when they are shifted by $+2\%$. In figure 6.4 the deviations from the cross sections are presented. The blue and pink filled area show the positive and negative shift of the particles respectively. For comparison the relative statistical uncertainty is also presented with black marker. The violet line is at 5%. It can be seen that the uncertainties are rarely exceeding 5%.

6.3 Summary

Various sources of systematic uncertainties were determined or taken from previous dedicated studies within the D^* measurements at H1 and are summarised in table 6.1. The dominant systematic errors are the track finding which is 6% and the luminosity 5%. The systematic uncertainty due to the trigger efficiency was significantly improved with respect to previous measurements in H1 [95]. The resulting total systematic uncertainty is 9.1%.

Source	$\Delta\sigma$
DIS Background	1%
D^0 Mass Cut	1%
Signal Extraction	1.2%
Luminosity	5%
Reflections	1%
Branching Ratio	1.5%
Primary Vertex Fit	1%
Track Finding	6%
Model Uncertainty	1.23%
Hadronic Energy Scale	-1.56% $+1.86\%$
Trigger Efficiency	3.1%
Total	$+9.13\%$ -9.07%

Table 6.1: A summary table of the systematic uncertainties on the measured cross section measurement.

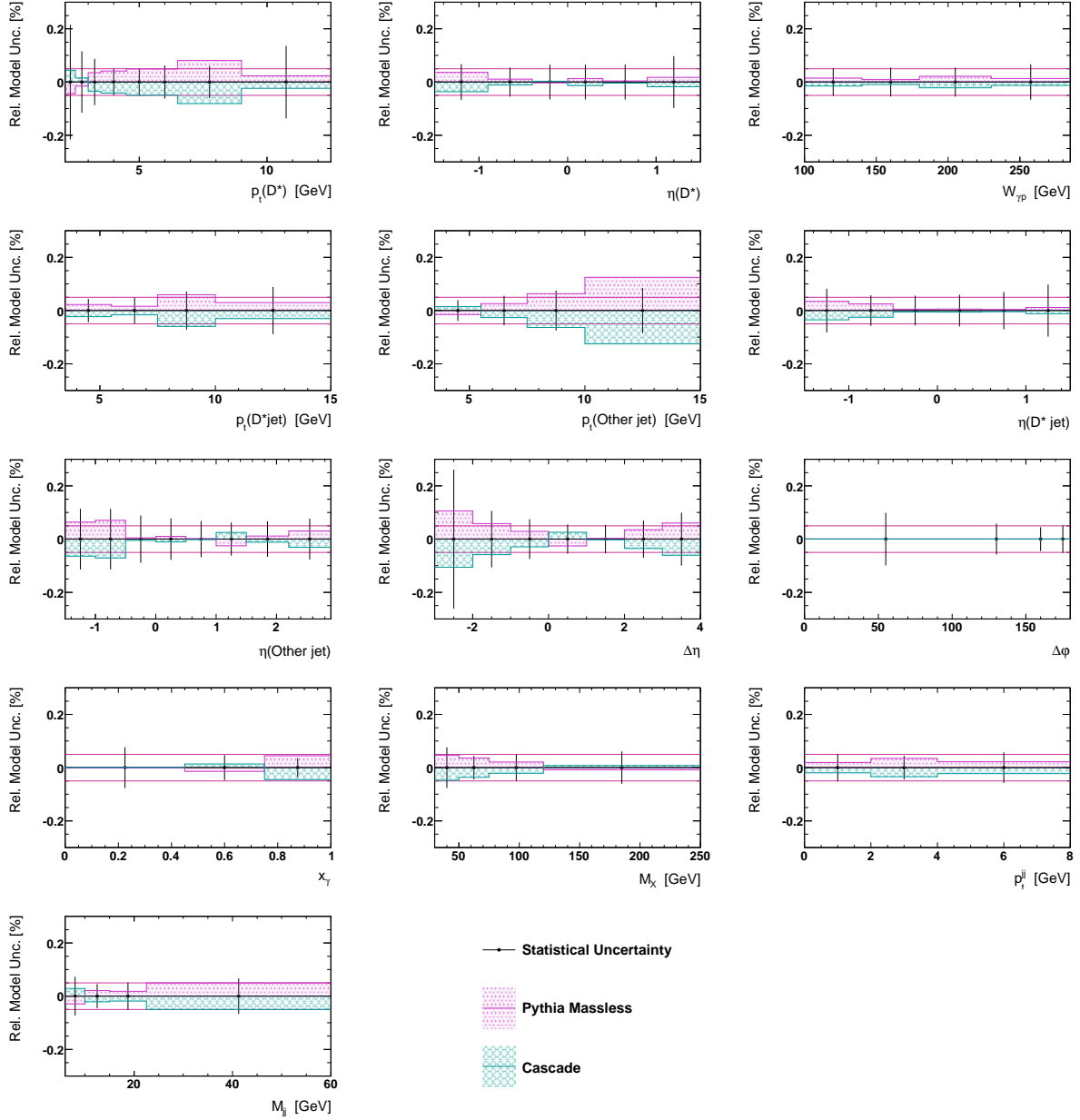


Figure 6.2: The relative uncertainty on the cross section due to the model used to correct the data as a function of number of variables. The blue area presents deviations from the cross sections when using CASCADE separately and the pink area is PYTHIA. The relative statistical uncertainty is presented with black markers. The line is at 5%.

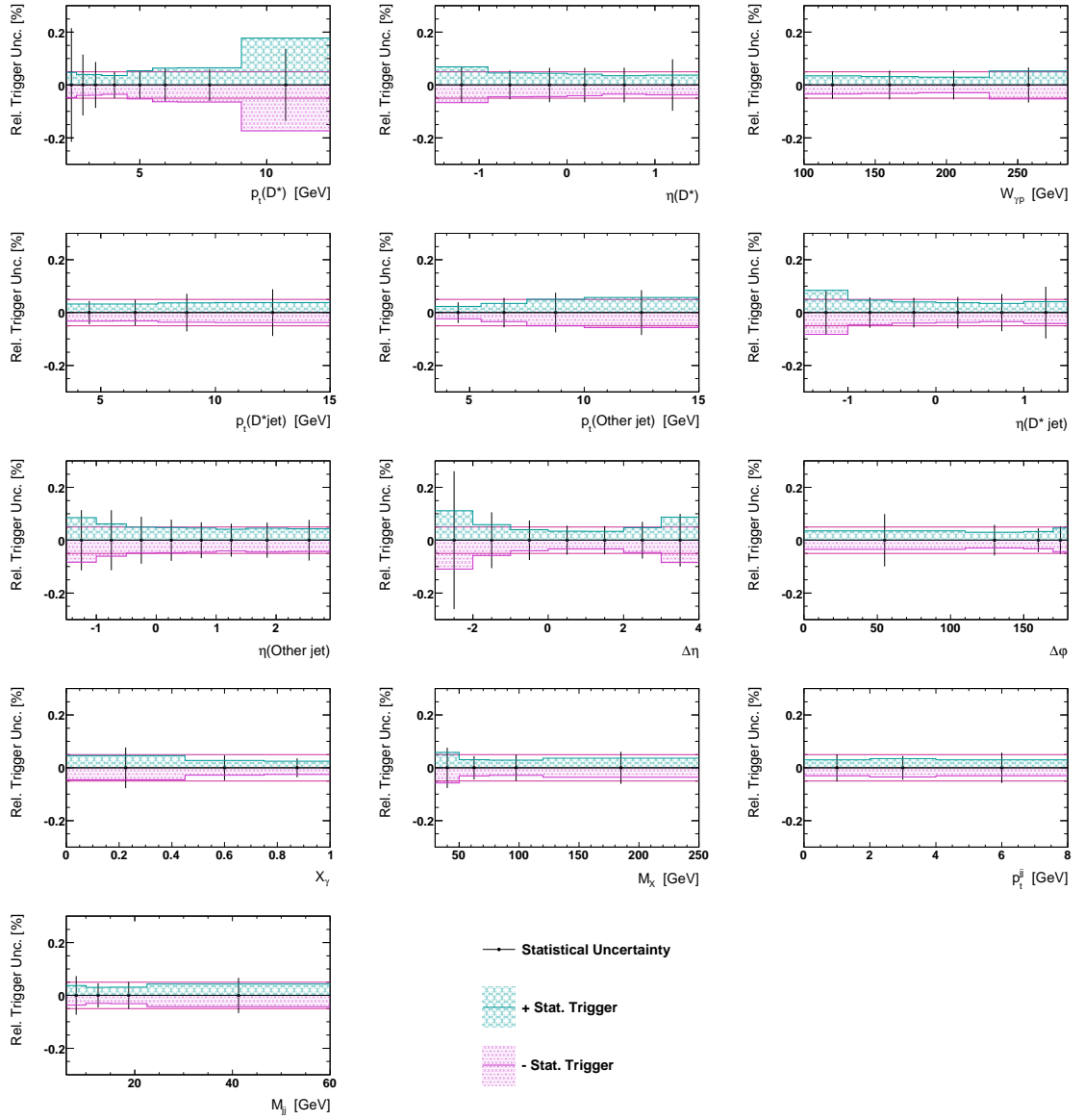


Figure 6.3: The relative uncertainty on the cross section due to the trigger efficiency determination differential in the variables important for the measurement. The blue and pink area presents the negative and positive uncertainty and the violet line is at 5%.

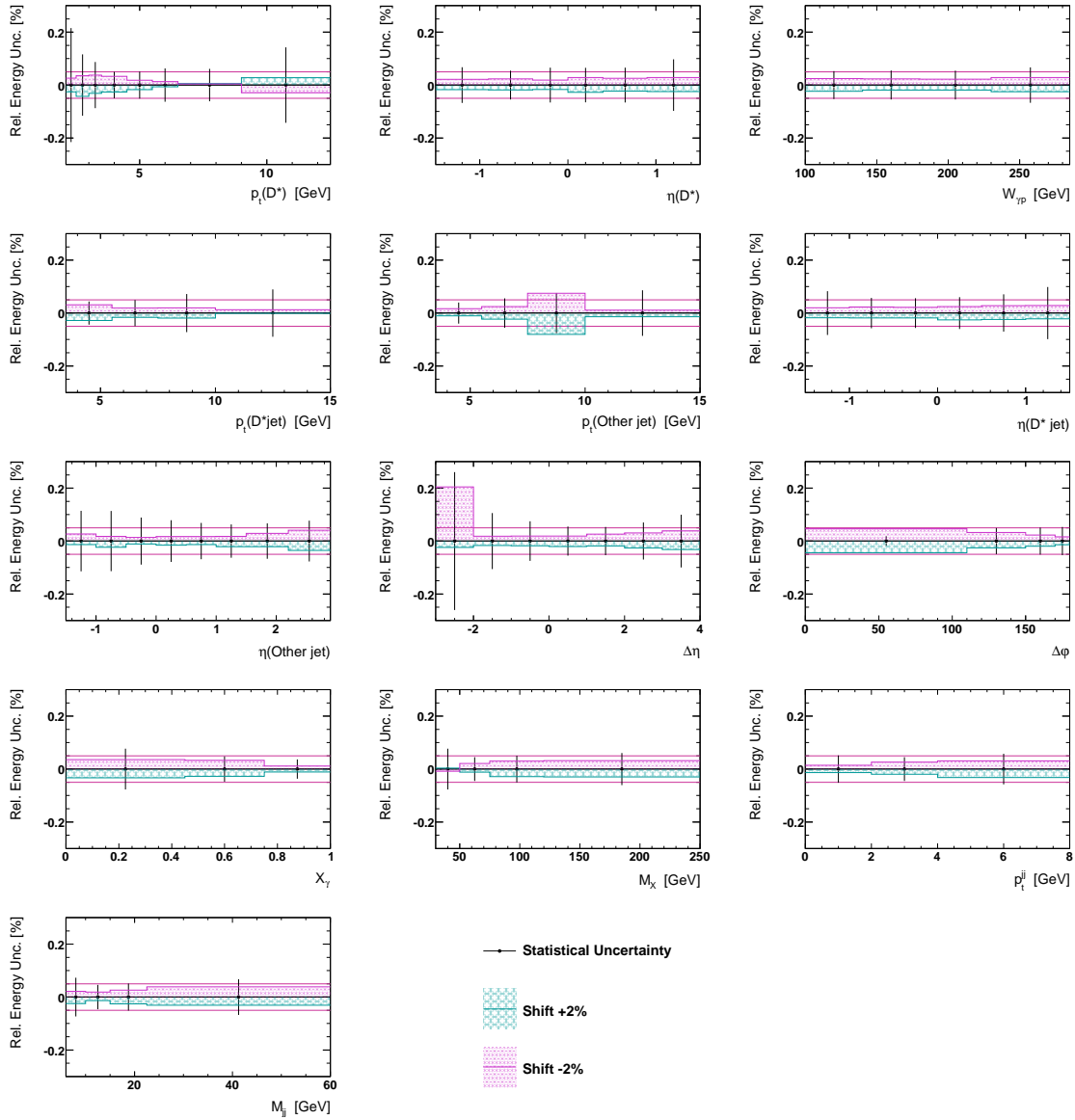


Figure 6.4: The relative uncertainty on the cross section due to energy scale uncertainty differential in the variables relevant for the analysis.

Chapter 7

Cross Section Determination and Results

7.1 $D^* + 2$ Jets Cross Section

The data were corrected to hadron level using the bin-by-bin method. For that purpose a Monte Carlo (MC) sample passed through the full detector simulation was used. The MC simulation was tuned with various reweighting procedures described in previous sections such that it describes the data. The trigger efficiency was taken into account via the trigger elements simulation in the MC. For the final cross section the following formula was used:

$$\sigma^{data} = \frac{N(D^*)^{data}}{\mathcal{L} \cdot \varepsilon^{rec} \cdot \mathcal{BR}(D^* \rightarrow K\pi\pi_{slow})} \quad (7.1)$$

where the \mathcal{L} is the luminosity. The reconstruction efficiency ε^{rec} is determined as follow:

$$\varepsilon^{rec} = \frac{N(D^*)_{w'}^{det}}{N(D^*)_w^{had}} \quad (7.2)$$

where w is the event weight calculated according to the description given in section 4.4. The event weight w' is $w \cdot \mathcal{L}$ where the \mathcal{L} was taken for each of the $p_t(D^*)$ bins (summarised in table 7.1).

In addition, in order to reduce the systematic uncertainty due to the model used for the correction of the data the final cross section was averaged between the cross sections obtained with correction factors by PYTHIA and CASCADE separately:

$$\sigma_{data}^{tot} = \frac{\sigma_{data}^{PYTHIA} + \sigma_{data}^{CASCADE}}{2} \quad (7.3)$$

The number of D^* mesons, $N(D^*)$ was determined from a fit to the mass difference Δm according to the description given in section 3.2.2. The statistical uncertainty of the measurement was obtained by applying the formula (7.1) to the uncertainty of $N(D^*)$ from the fit and then averaging the resulting uncertainty with equation (7.3). This leads to a total

cross section for D^* and two jets in photoproduction in the visible range (table 7.2) of:

$$\sigma^{tot} = 9.76 \pm 0.28(stat) \pm 0.89(syst) \text{ nb} \quad (7.4)$$

where the systematic uncertainties were taken into account as summarised in chapter 6 and the statistical uncertainty is the uncertainty of the fit of the Δm distribution.

Sub-trigger	p_t range	\mathcal{L}
s55	$2.1 \text{ GeV} < p_t(D^*) < 2.5 \text{ GeV}$	30.66 pb^{-1}
s53	$2.5 \text{ GeV} < p_t(D^*) < 4.5 \text{ GeV}$	68.21 pb^{-1}
s122	$4.5 \text{ GeV} < p_t(D^*) < 12.5 \text{ GeV}$	93.35 pb^{-1}

Table 7.1: The sub-trigger p_t ranges and the corresponding luminosity.

7.2 Differential Cross Sections

The differential cross sections were obtained in a similar way as the total cross section where formula (7.1) was applied in each bin of the measured variable. At the end, the cross sections were normalised to the bin size such that the integral of the differential cross section gives the total cross section. In the figures the data are represented by the black markers where the inner error bar gives the systematic uncertainty of the measurement and outer error bar is the total uncertainty which is quadratic sum of the statistical and systematic uncertainty.

The differential cross sections were compared to predictions from the MC generator PYTHIA run in the massive and massless mode, CASCADE and the next-to-leading order MC program MC@NLO. The features of the models are summarised in section 1.4.

In figure 7.1 the differential cross section as a function of the D^* transverse momentum $p_t(D^*)$, pseudorapidity of the D^* and the invariant mass of the photon-proton system is shown. The transverse momentum of the D^* is steeply falling distribution with an average value of 3 GeV is well described by the MC models. It can be seen that at high transverse momentum the CASCADE prediction is slightly better than the two calculations from PYTHIA, while at low p_t CASCADE is below the measurement. This could be explained with the fact

$0.1 < y_h < 0.8$
$Q^2 < 2. \text{ GeV}^2$
$2.1 \text{ GeV} < p_t(D^*) < 12.5 \text{ GeV}$
$ \eta(D^*) < 1.5$
$3.5 \text{ GeV} < p_t(D_{\text{jet}}^*, \text{ Other jet}) < 15. \text{ GeV}$
$ \eta(D_{\text{jet}}^*) < 1.5$
$-1.5 < \eta(\text{Other jet}) < 2.9$
$M_{\text{jj}} > 6 \text{ GeV}$

Table 7.2: The visible range of the measurement.

that in the CCFM parton shower approach (represented by CASCADE) in general harder partons are emitted in comparison to the DGLAP (represented by PYTHIA). The pseudo-rapidity distribution is also well modelled by the calculations. It can be seen that in the most forward bin the calculations are slightly below the data. This tendency was already observed before at H1 [108]. The $W_{\gamma p}$ distribution is smoothly falling towards large invariant masses and is well described by the MC models in the low invariant mass region. In the large $W_{\gamma p}$ region the models underestimate the data. The comparison between the measured differential cross sections and MC@NLO is shown in figure 7.1 below. The scale uncertainties of the calculation are represented by the pink band. It can be seen that the $p_t(D^*)$ spectrum is not described in the small p_t region. The predictions of MC@NLO are factor of ~ 2 below the data. This region dominates statistically the measurement and the discrepancy is then transferred to the $\eta(D^*)$ and $W_{\gamma p}$ as a normalisation factor. However the shapes for the $W_{\gamma p}$ and the rapidity of the D^* meson from MC@NLO is very well reproducing the shape of the data.

In figure 7.2 the differential cross sections for $ep \rightarrow D^* + 2\text{jets} + X$ as a function of the D_{jet}^* and the other jet transverse momentum and pseudorapidity are shown. The models exhibit a similar behaviour as for the D^* transverse momentum, CASCADE describes the high p_t region while the PYTHIA models describe well the low transverse momentum. The pseudorapidity for the D_{jet}^* follows the pseudorapidity spectrum of the D^* itself. The pseudorapidity for the other jet has a maximum at positive values. The distributions are well modelled by all approaches. The discrepancy of the low $p_t(D^*)$ region from MC@NLO (distributions shown in figure 7.2 below) transfers in the p_t spectra of the jets. Within the scale uncertainty the shapes of the pseudorapidities of the jets are well reproduced by the generator.

In figure 7.3 correlations between the jets, namely the azimuthal angle difference $\Delta\varphi$, the invariant mass of the remnant of the event M_X , the average transverse momentum of the di-jet pair p_t^{jj} and the longitudinal momentum fraction of the photon carried by the jets x_γ are shown. The $\Delta\varphi$ distribution exhibits a steeply falling spectrum going over two orders of magnitude with a significant tail towards small $\Delta\varphi$. The data and the MC models show significantly different shapes. It can be seen that in the back-to-back region where the jets are balanced in p_t the data are best described by the massive PYTHIA calculation. The data are overestimated by the massless approach of PYTHIA while CASCADE is a factor of two below the data. In the small $\Delta\varphi$ where the contribution of further gluon radiation is expected to play a significant role the data are best described by CASCADE. No significant difference between the two PYTHIA predictions is found, while both of them are factor of ~ 4 below the data. The M_X distribution is falling towards large values with a maximum at around 50 GeV. With the exception the highest M_X bin, where all three models are below the data, the distribution is well described. The average transverse momentum of the di-jet pair p_t^{jj} is falling towards large values. The behaviour of the distribution reveals similar dynamics as

the $\Delta\varphi$ distribution: the data are well described at small values, where the jets are balanced in p_t by the massive PYTHIA calculation, while at large values, where the balance is violated by further gluon radiation, the measurement is well described by CASCADE.

The longitudinal momentum fraction of the photon carried by the jets x_γ is a falling distribution towards small values. The high x_γ region where the jet pair takes only small fraction of the photon energy, and the photon enters the hard interaction as a pointlike particle (in other words direct photons), the measurement is well described by all the models and no significant difference is found within the uncertainty of the measurement. Towards small values, where the contribution of resolved photons becomes significant a deficit of the three models is found in the smallest x_γ bin. The CASCADE prediction is compatible with the prediction from the massive PYTHIA calculation. Closest to the data is the massless prediction of PYTHIA, but is still factor of ~ 2 below the data. In the same figure 7.3 below, the predictions from MC@NLO for the same distributions together with the data are shown. The normalisation problem from the low p_t region is transferred here too. The shapes of $\Delta\varphi$ and p_t^{jj} are also well reproduced. However, the shape of the M_X distribution is very different in comparison to the LO MC models. Here MC@NLO is above the data in the first bin while the other MC models are below. It is interesting to point out that the discrepancy of MC@NLO with the data is now located at low values of x_γ . In the highest x_γ bin, the prediction is very well reproducing the measurement while towards small values, MC@NLO is significantly below the data.

In order to understand the different shapes in $\Delta\varphi$ of the predictions and the data, two different regions of the x_γ were used. Usually this quantity is used to discriminate between resolved and direct photons. In figure 7.4 the differential cross section as a function of $\Delta\varphi$ in the two regions of x_γ is shown.

In the region $x_\gamma \in [0.75, 1)$ the distribution is even steeper than for the full $\Delta\varphi$ distribution (figure (a)). It can be seen that the predictions from PYTHIA and CASCADE are closer to the data in the back-to-back region. In the region of small $\Delta\varphi$ it can be seen that CASCADE is slightly above the data, but the difference is found to be smaller than a factor of two and is less than one sigma away from the data. In this region, the two PYTHIA predictions exhibit a very different shape: the massive calculation is found to be closer to the data than the massless calculation. The data are a factor of five above the PYTHIA prediction. This effect can be explained with the fact that in the DGLAP with LO matrix elements approach, high transverse momentum partons beyond the leading partons in the quark box are not expected. However those partons would be needed to violate the correlation. CCFM (represented by CASCADE) on the other hand allows emissions of partons with higher transverse momentum than the partons the matrix elements, and therefore can describe the decorrelation of the data. The MC@NLO prediction (see figure 7.4 (c)) is very well reproducing the differential cross section and is compatible with the predictions from CASCADE. Discrepancy is found only in

the lowest $\Delta\varphi$ bin, where the prediction is found to be one sigma above the measurement. In the region of $x_\gamma \in (0, 0.75)$ (figure 7.4 (b)) the data show a much flatter distribution ranging only over an order of magnitude. This region is resolved photons enriched. It can be seen CASCADE is factor ~ 3 below the data in the back-to-back region. The PYTHIA predictions reproduce the measurement nicely in that region. Towards small values of $\Delta\varphi$ the data and the CASCADE prediction come closer where in the smallest bin the agreement between the model and the data is perfect. In that bin both PYTHIA results are much closer together than for the direct photons case. The difference to data is smaller than in the $x_\gamma \geq 0.75$ region but is still significant. The comparison with MC@NLO (figure 7.4 (d)) the too small cross section in the resolved photon case is clearly visible here. However, the shape of the prediction is compatible with the one from the data.

In addition the invariant mass of the remnant is also investigated in two bins of x_γ and the resulting differential cross sections are shown in figure 7.5. For the high x_γ region the distribution is falling towards large values with a maximum at around 70 GeV. In the highest M_X bin, the uncertainty of the measurement goes up to 30% which is dominated by the trigger efficiency due to lack of statistics in this bin for the monitor sample. The three MC calculations reproduce the measurement nicely. For the low x_γ the distribution is shifted towards higher values. The distribution is flatter and has a maximum at 100 GeV. Here the measurement is also well reproduced by the models although the spread between the models is very large but the uncertainty of the measurement is also large so no strong conclusions can be drawn. However in the highest M_X bin the data are significantly above the CASCADE and the massive PYTHIA prediction. In this bin the best description is provided by the massless PYTHIA calculation. In the case of resolved photons the system M_X is build from partons radiated from the proton and photon side (see figure 1.9).

7.3 Summary and Discussion

From the measured differential distributions it can be seen that in general, the D^* meson kinematics as well as the jets kinematics are well reproduced by the MC models. However better agreement is found with the PYTHIA model in the low transverse momentum region while the high transverse regions are well reproduced by CASCADE. In addition several correlations between the di-jet pair were studied. It was shown that the $\Delta\varphi$ distribution is highly sensitive to the kinematics of the incoming gluon. It was shown that the data are well described by the DGLAP based MC model PYTHIA ran in the massive approach in the region where the jets are found to be back-to-back. However in the decorrelation region where the jets are found close in the transverse plane, the model is factor of ~ 4 below the data and a better description here is provided by the CCFM based MC model CASCADE. The predictions from MC@NLO are found to be below the data, however a very good agreement is found in the shapes of the measured cross section and the calculation.

Further it was shown that in the case of direct photons, the $\Delta\varphi$ reveals very different shapes for both PYTHIA predictions. Here the agreement between the data and CASCADE as well as the predictions from MC@NLO is found to be very good. In the region of resolved photons, the distribution is significantly underestimated by the CASCADE model in the back-to-back region while towards small values, the agreement between the data and the model is very good.

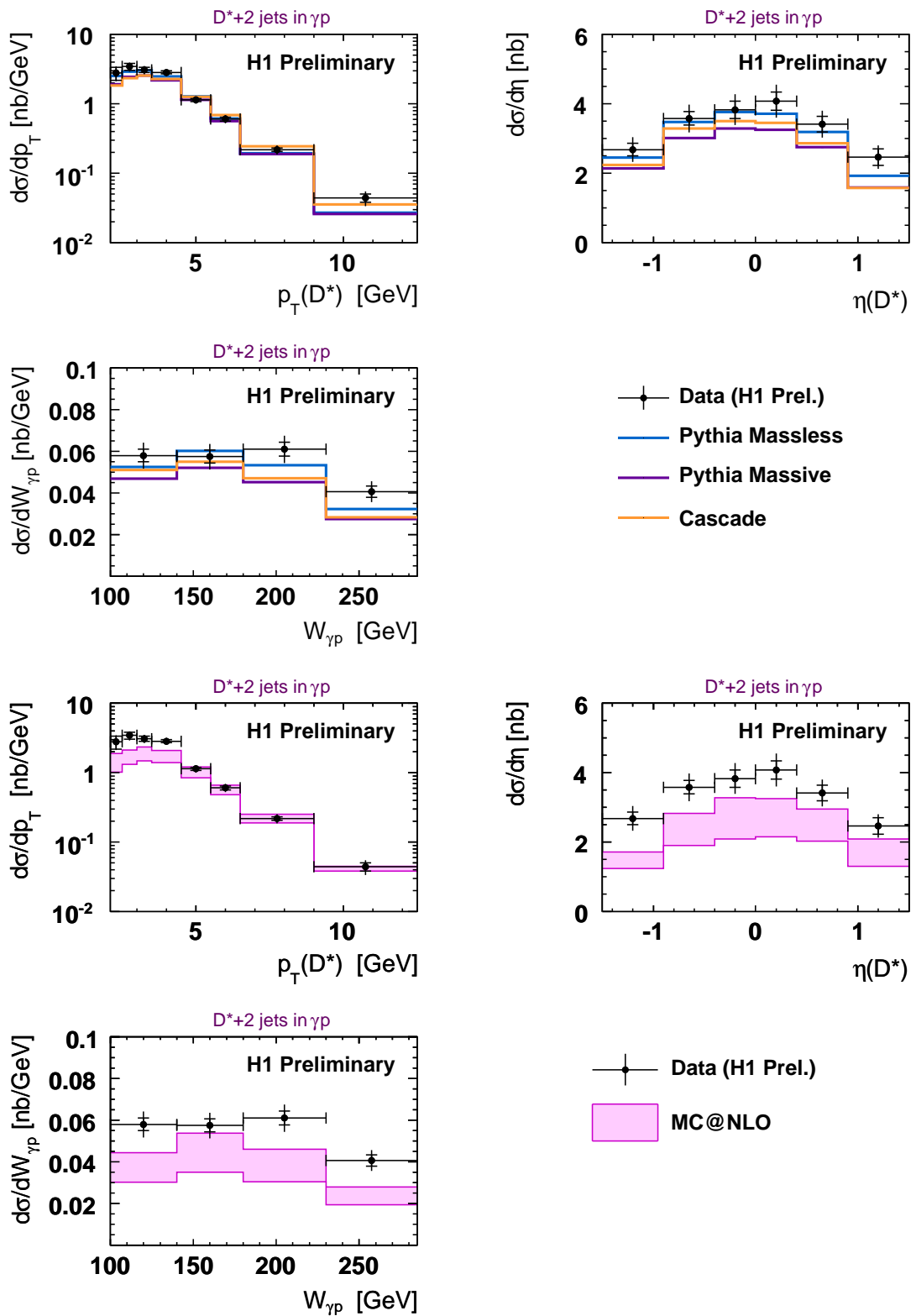


Figure 7.1: The differential cross section for $ep \rightarrow D^* + 2\text{jets} + X$ as a function of the D^* transverse momentum, rapidity and the invariant mass of the γp system $W_{\gamma p}$. Black dots represent the measurement, the blue line is PYTHIA massless, purple line PYTHIA massive and orange line CASCADE. The pink band are the predictions together with the scale uncertainty by MC@NLO.

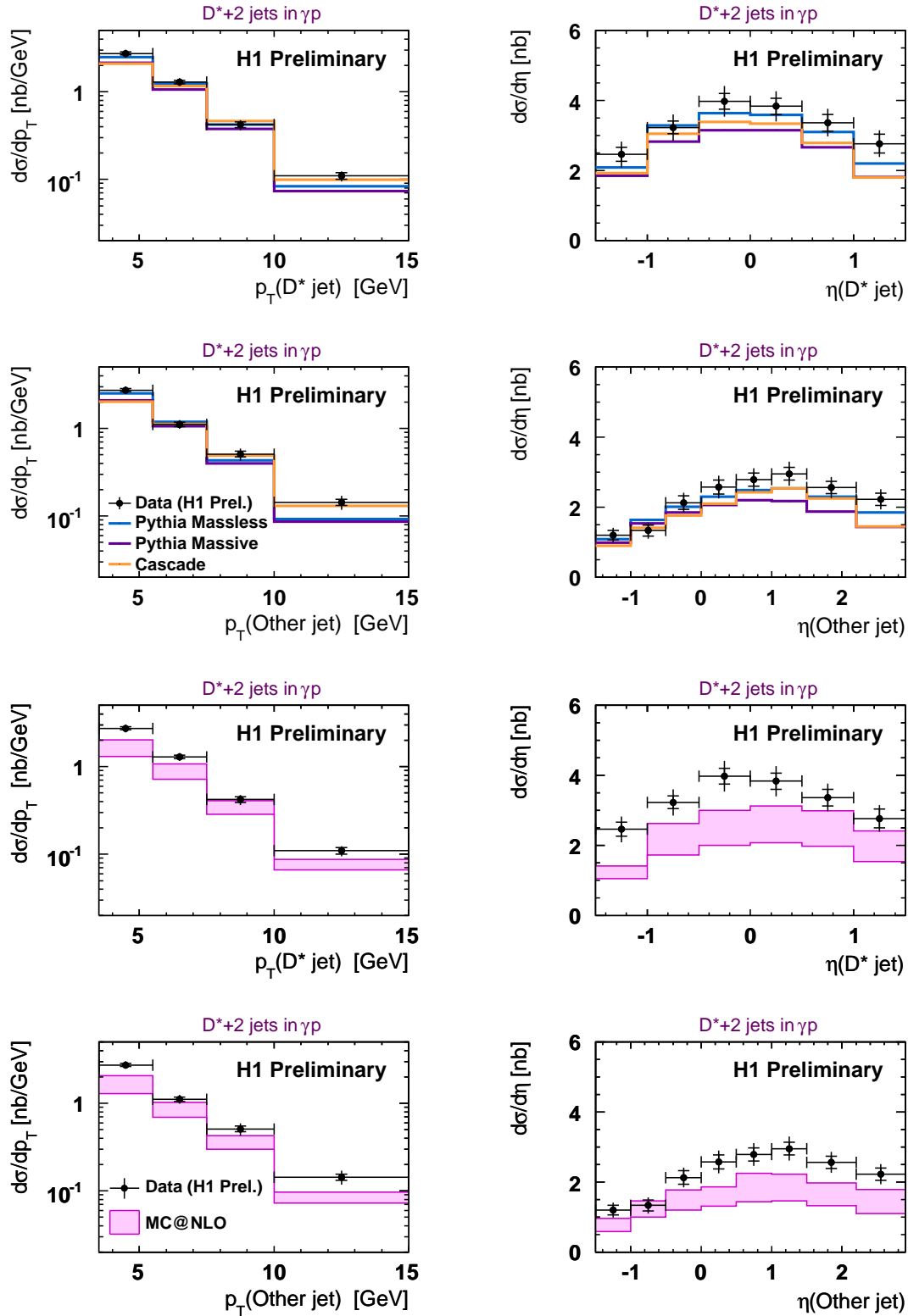


Figure 7.2: The differential cross section for $ep \rightarrow D^* + 2\text{jets} + X$ as a function of the jets transverse momentum and rapidity. Black dots represent the measurement, the blue line is PYTHIA massless, purple line PYTHIA massive and orange line CASCADE. The pink band are the predictions together with the scale uncertainty by MC@NLO.

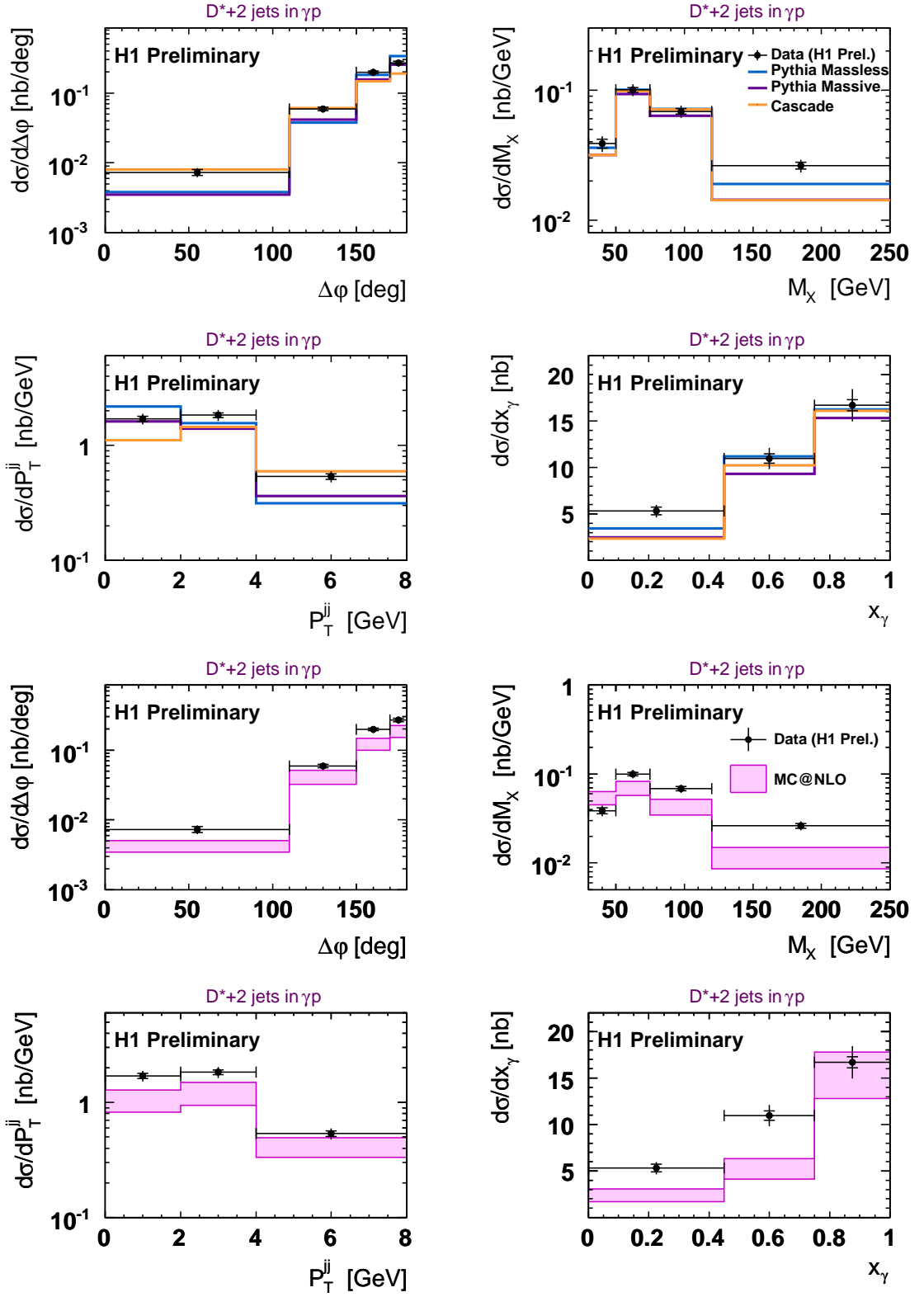


Figure 7.3: The differential cross section for $ep \rightarrow D^* + 2\text{jets} + X$ as a function of the $\Delta\phi$ between the jets, the M_X , p_t^{jj} and the x_γ . Black dots represent the measurement, the blue line is PYTHIA massless, purple line PYTHIA massive and orange line CASCADE. The pink band are the predictions together with the scale uncertainty by MC@NLO.

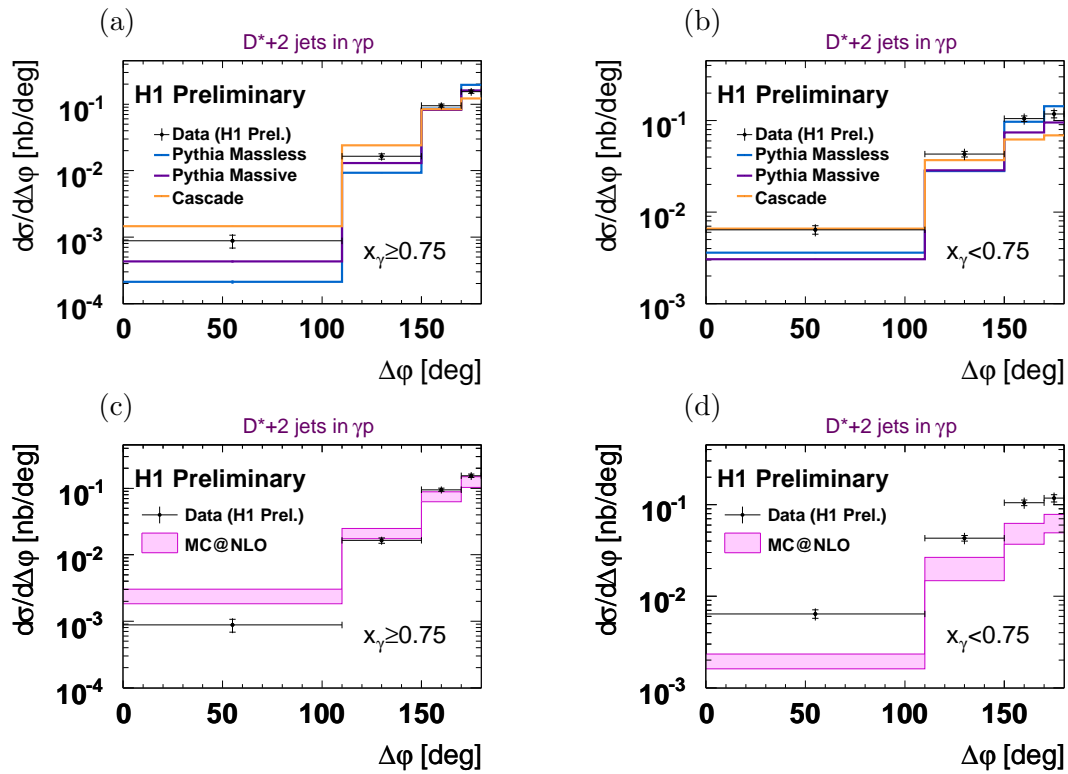


Figure 7.4: The differential cross section for $ep \rightarrow D^* + 2\text{jets} + X$ as a function of the $\Delta\varphi$ between the jets in two bins of x_γ . Black dots represent the measurement, the blue line is PYTHIA massless, purple line PYTHIA massive and orange line CASCADE. The pink band are the predictions together with the scale uncertainty by MC@NLO.

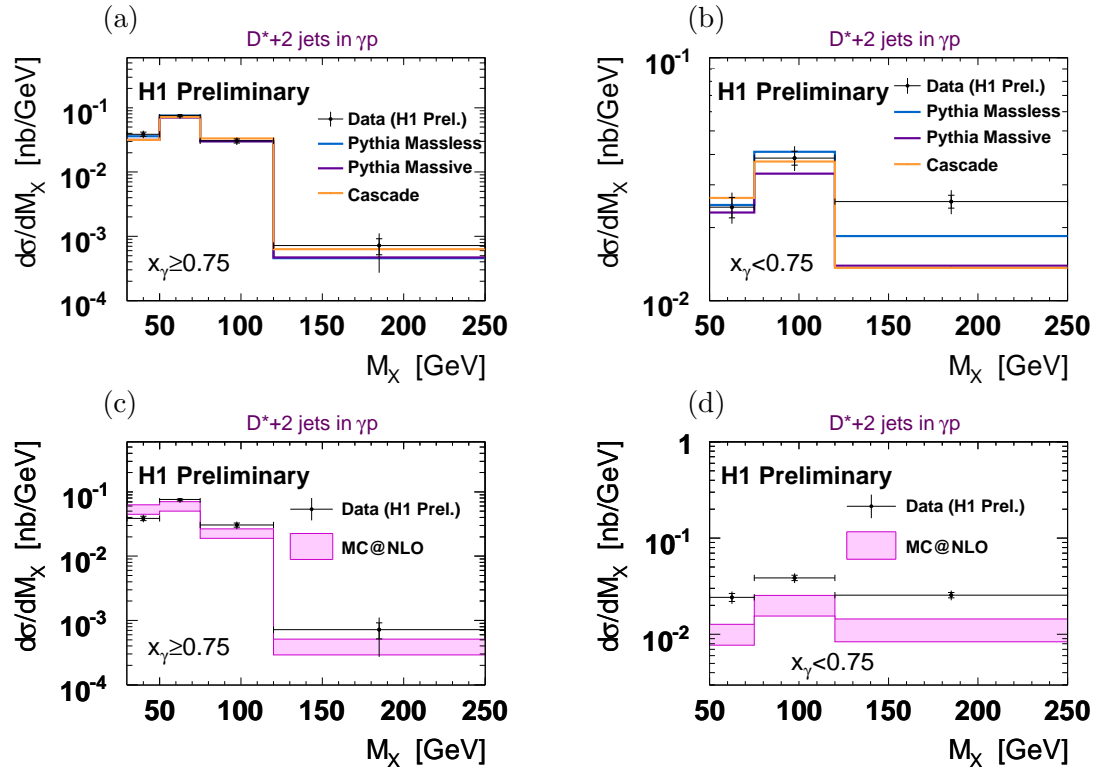


Figure 7.5: The differential cross section for $ep \rightarrow D^* + 2\text{jets} + X$ as a function of the M_X between the jets in two bins of x_γ . Black dots represent the measurement, the blue line is PYTHIA massless, purple line PYTHIA massive and orange line CASCADE. The pink band are the predictions together with the scale uncertainty by MC@NLO.

Conclusions

A measurement of D^* charmed mesons associated with two jets in untagged photoproduction using the HERA II data set of the H1 detector was presented. The statistics of the measurement is four times bigger than a previous measurement at H1. Detailed trigger efficiency studies were performed which have lead to a significant decrease of the systematic uncertainty.

The charm production mechanism is highly sensitive to the gluon content of the proton and by measuring differential cross sections as a function of different observables important information about the kinematics of the incoming gluon can be obtained. This has allowed different parton shower models to be tested.

Cross sections are measured as a function of the D^* meson and jet kinematics are reasonably well described by the Leading Order Monte Carlo models (LO MC) PYTHIA and CASCADE. Two new quantities, the invariant mass of the remnant in the event M_X and the average transverse momentum of the di-jet pair p_t^{jj} were introduced and measured. The M_X distribution is sensitive to the full kinematics of the incoming gluon and is fairly well described by the MC models. The difference between the data and the MCs was found only for the part of the phase space where the photon is resolved where the photon evolves a hadron like structure. For the direct case the distribution is well reproduced. None of the models are able to satisfactorily describe the average transverse momentum of the di-jet pair which is highly correlated to the azimuthal angle difference $\Delta\varphi$ between the jets. In general CASCADE gives a good description of the distribution at small values of $\Delta\varphi$ where contributions from higher order gluon radiation are important. In this region PYTHIA predicts too small a cross section. Conversely in the peak region of high $\Delta\varphi$ the data are best described by PYTHIA while CASCADE predicts too small a cross section.

A new MC at next-to-leading order MC, the MC@NLO was also compared to the data. It was found that the generator predicts too small a cross section at low transverse momentum of the D^* and in the low region of the longitudinal momentum fraction of the photon x_γ carried by the jets. However the shapes predicted by MC@NLO are very good.

The precision of the presented measurement is good enough to resolve significant differences between the data and the different parton shower models used for comparison. None of the models reproduces the measurement satisfactorily in quantities which are sensitive to

the kinematics of the incoming gluon in the photon gluon fusion process. Proper modelling of the kinematics of the incoming gluon is of particular importance in order to account for higher order hard gluon emissions which have a significant impact of heavy quark production in ep collisions. These can be even larger at higher energies such as at the LHC. The proper treatment of higher order emissions is important for any heavy quark measurement at the LHC, which is a main source of background for potential discoveries, emphasising the importance of the data provided by the HERA experiments.

Bibliography

- [1] E. Rutherford, *The scattering of α and β particles by matter and the structure of the atom*, Phil. Mag. **21** (1911), 669.
- [2] A. Aktas et al. (H1 Collaboration), *Inclusive D^{*+-} meson cross sections and D^{*+-} jet correlations in photoproduction at HERA*, Eur. Phys. J. **C50** (2007), 251, [hep-ex/0608042](#).
- [3] S. Chekanov et al. (ZEUS Collaboration), *Inclusive jet cross sections and dijet correlations in D^{*+-} photoproduction at HERA*, Nucl. Phys. **B729** (2005), 492, [hep-ex/0507089](#).
- [4] R. Devenish and A. Cooper-Sarkar, *Deep Inelastic Scattering*, Oxford University Press (2004).
- [5] F. D. Aaron et al. (H1 and ZEUS Collaboration), *Combined Measurement and QCD Analysis of the Inclusive ep Scattering Cross Sections at HERA*, JHEP **01** (2010), 109, [0911.0884](#).
- [6] R. K. Ellis, W. J. Stirling, and B. R. Webber, *QCD and Collider Physics*, Cambridge Monographs on Particle Physics, Nuclear Physics and Cosmology (2003).
- [7] D. J. Gross and F. Wilczek, *Ultraviolet Behaviour of Non-Abelian Gauge Theories*, Phys. Rev. Lett. **30** (1973), 1343.
- [8] M. Jimenez (H1 and ZEUS Collaboration), *Jets and alpha(s) measurements in DIS at HERA*, Nucl. Phys. Proc. Suppl. **184** (2008), 109.
- [9] J. C. Collins, D. E. Soper, and G. F. Sterman, *Factorization of Hard Processes in QCD*, Adv. Ser. Direct. High Energy Phys. **5** (1988), 1, [hep-ph/0409313](#).
- [10] V. N. Gribov and L. N. Lipatov, *Deep inelastic e p scattering in perturbation theory*, Sov. J. Nucl. Phys. **15** (1972), 438.
- [11] G. Altarelli and G. Parisi, *Asymptotic Freedom in Parton Language*, Nucl. Phys. **B126** (1977), 298.

- [12] Y. L. Dokshitzer, *Calculation of the Structure Functions for Deep Inelastic Scattering and $e^+ e^-$ Annihilation by Perturbation Theory in Quantum Chromodynamics. (In Russian)*, Sov. Phys. JETP **46** (1977), 641.
- [13] L. N. Lipatov, *The parton model and perturbation theory*, Sov. J. Nucl. Phys. **20** (1975), 94.
- [14] A. Aktas et al. (H1 Collaboration), *Forward jet production in deep inelastic scattering at HERA*, Eur. Phys. J. **C46** (2006), 27, [hep-ex/0508055](#).
- [15] S. Chekanov et al. (ZEUS Collaboration), *Forward jet production in deep inelastic $e p$ scattering and low- x parton dynamics at HERA*, Phys. Lett. **B632** (2006), 13, [hep-ex/0502029](#).
- [16] V. S. Fadin, E. A. Kuraev, and L. N. Lipatov, *On the Pomeron Singularity in Asymptotically Free Theories*, Phys. Lett. **B60** (1975), 50.
- [17] E. A. Kuraev, L. N. Lipatov, and V. S. Fadin, *The Pomeron Singularity in Non-abelian Gauge Theories*, Sov. Phys. JETP **45** (1977), 199.
- [18] M. Ciafaloni, *Coherence Effects in Initial Jets at Small q^{*2} / s* , Nucl. Phys. **B296** (1988), 49.
- [19] S. Catani, F. Fiorani, and G. Marchesini, *QCD Coherence in Initial State Radiation*, Phys. Lett. **B234** (1990), 339.
- [20] S. Catani, F. Fiorani, and G. Marchesini, *Small x Behavior of Initial State Radiation in Perturbative QCD*, Nucl. Phys. **B336** (1990), 18.
- [21] G. Marchesini, *QCD coherence in the structure function and associated distributions at small x* , Nucl. Phys. **B445** (1995), 49, [hep-ph/9412327](#).
- [22] C. F. von Weizsacker, *Radiation emitted in collisions of very fast electrons*, Z. Phys. **88** (1934), 612.
- [23] E. J. Williams, *Nature of the high-energy particles of penetrating radiation and status of ionization and radiation formulae*, Phys. Rev. **45** (1934), 729.
- [24] T. H. Bauer, R. D. Spital, D. R. Yennie, and F. M. Pipkin, *The Hadronic Properties of the Photon in High-Energy Interactions*, Rev. Mod. Phys. **50** (1978), 261.
- [25] J. J. Sakurai, *Vector meson dominance and high-energy electron proton inelastic scattering*, Phys. Rev. Lett. **22** (1969), 981.
- [26] H. Fraas and D. Schildknecht, *Vector Meson Dominance and Polarisation* DESY-68-4.

- [27] E. Witten, *Anomalous Cross-Section for Photon - Photon Scattering in Gauge Theories*, Nucl. Phys. **B120** (1977), 189.
- [28] R. J. DeWitt, L. M. Jones, J. D. Sullivan, D. E. Willen, and H. W. Wyld, Jr., *Anomalous Components of the Photon Structure Functions*, Phys. Rev. **D19** (1979), 2046.
- [29] T. Ahmed et al. (H1 Collaboration), *Hard scattering in gamma p interactions*, Phys. Lett. **B297** (1992), 205.
- [30] M. Derrick et al. (ZEUS Collaboration), *Observation of hard scattering in photoproduction at HERA*, Phys. Lett. **B297** (1992), 404.
- [31] M. Erdmann, *Proton and Photon Structure* (2001), [Talk given at Lepton Photon Conference, Rome, Italy](#).
- [32] B. A. Kniehl, *Hadron production in hadron hadron and lepton hadron collisions* (2002), [hep-ph/0211008](#).
- [33] B. Andersson, G. Gustafson, and B. Soderberg, *A General Model for Jet Fragmentation*, Z. Phys. **C20** (1983), 317.
- [34] B. Andersson, G. Gustafson, G. Ingelman, and T. Sjostrand, *Parton Fragmentation and String Dynamics*, Phys. Rept. **97** (1983), 31.
- [35] M. G. Bowler, *$e^+ e^-$ Production of Heavy Quarks in the String Model*, Zeit. Phys. **C11** (1981), 169.
- [36] T. D. Gottschalk, *An Improved Description of Hadronization in the QCD Cluster Model for $e^+ e^-$ Annihilation*, Nucl. Phys. **B239** (1984), 349.
- [37] B. R. Webber, *A QCD Model for Jet Fragmentation Including Soft Gluon Interference*, Nucl. Phys. **B238** (1984), 492.
- [38] G. Dissertori, I. Knowles, and M. Schmelling, *Quantum Chromodynamics*, Oxford University Press (2003).
- [39] G. P. Salam and G. Soyez, *A practical Seedless Infrared-Safe Cone jet algorithm*, JHEP **05** (2007), 086, [0704.0292](#).
- [40] S. D. Ellis and D. E. Soper, *Successive combination jet algorithm for hadron collisions*, Phys. Rev. **D48** (1993), 3160, [hep-ph/9305266](#).
- [41] J. M. Butterworth, J. P. Couchman, B. E. Cox, and B. M. Waugh, *KtJet: A C++ implementation of the $K(T)$ clustering algorithm*, Comput. Phys. Commun. **153** (2003), 85, [hep-ph/0210022](#).

- [42] J. E. Augustin et al. (SLAC-SP-017 Collaboration), *Discovery of a Narrow Resonance in $e^+ e^-$ Annihilation*, Phys. Rev. Lett. **33** (1974), 1406.
- [43] J. J. Aubert et al. (E598 Collaboration), *Experimental Observation of a Heavy Particle J* , Phys. Rev. Lett. **33** (1974), 1404.
- [44] L. Marti Magro, *Multiple parton interactions in photoproduction at HERA- H1* DESY-THESIS-2009-007.
- [45] J. Collins and H. Jung, *Need for fully unintegrated parton densities* (2005), [hep-ph/0508280](#).
- [46] L. Loenblad, *Monte Carlo techniques and physics* (2008), [Talk given at Terascale Monte Carlo School, Hamburg](#).
- [47] T. Sjostrand et al., *High-energy-physics event generation with PYTHIA 6.1*, Comput. Phys. Commun. **135** (2001), 238, [hep-ph/0010017](#).
- [48] H. Jung and G. P. Salam, *Hadronic final state predictions from CCFM: The hadron- level Monte Carlo generator CASCADE*, Eur. Phys. J. **C19** (2001), 351, [hep-ph/0012143](#).
- [49] H. Jung, *The CCFM Monte Carlo generator CASCADE*, Comput. Phys. Commun. **143** (2002), 100, [hep-ph/0109102](#).
- [50] S. Kretzer, H. L. Lai, F. I. Olness, and W. K. Tung, *CTEQ6 parton distributions with heavy quark mass effects*, Phys. Rev. **D69** (2004), 114005, [hep-ph/0307022](#).
- [51] J. Pumplin et al., *New generation of parton distributions with uncertainties from global QCD analysis*, JHEP **07** (2002), 012, [hep-ph/0201195](#).
- [52] G. A. Schuler and T. Sjostrand, *Parton Distributions of the Virtual Photon*, Phys. Lett. **B376** (1996), 193, [hep-ph/9601282](#).
- [53] M. Gluck, E. Reya, and A. Vogt, *Parton structure of the photon beyond the leading order*, Phys. Rev. **D45** (1992), 3986.
- [54] J. Wagner, *Charm and Beauty Production at HERA with $D^* - \mu$ Events* DESY-THESIS-2004-022.
- [55] M. Hansson and H. Jung, *Status of CCFM: Un-integrated gluon densities* (2003), [hep-ph/0309009](#).
- [56] T. Toll, *MC@NLO for heavy flavour photoproduction at HERA* DESY-THESIS-2010-004.

- [57] S. Frixione, M. L. Mangano, P. Nason, and G. Ridolfi, *Total Cross Sections for Heavy Flavour Production at HERA*, Phys. Lett. **B348** (1995), 633, [hep-ph/9412348](#).
- [58] M. Martisikova, *Jet shapes in charm photoproduction at HERA* DESY-THESIS-2005-047.
- [59] G. Flucke, *Photoproduction of D^* Mesons and D^* Mesons Associated with Jets at HERA*, DESY-THESIS **380** (2005).
- [60] G. Corcella et al., *HERWIG 6.5: an event generator for Hadron Emission Reactions With Interfering Gluons (including supersymmetric processes)*, JHEP **01** (2001), 010, [hep-ph/0011363](#).
- [61] R. Brun, F. Bruyant, M. Maire, A. C. McPherson, and P. Zancarini, *GEANT3* CERN-DD-EE-84-1.
- [62] B. H. Wiik, *HERA: The Accelerator and the Physics*, Acta Phys. Polon. **B16** (1985), 127.
- [63] T. Nishikawa, *Electron - Positron Colliders: Opportunities and Prospects* Invited talk at Int. Conf. on Physics in Collision: High Energy ee/ep/pp Interactions, Blacksburg, Va., May 28-31, 1981.
- [64] F. D. Aaron et al. (H1 Collaboration), *The H1 Experiment* (2010), URL <http://www-h1.desy.de/>.
- [65] H. Abramowicz et al. (ZEUS Collaboration), *The ZEUS Experiment* (2010), URL <http://www-zeus.desy.de/>.
- [66] A. Airapetian et al. (HERMES Collaboration), *The HERMES Experiment* (2010), URL <http://www-hermes.desy.de/>.
- [67] I. Abt et al. (HERA B Collaboration), *The HERA B Experiment* (2010), URL <http://www-hera-b.desy.de/>.
- [68] J. Grebenyuk (ZEUS and H1 Collaboration), *Combined measurement of the Inclusive $e+p$ Scattering Cross Sections at HERA for Reduced Proton Beam Energy Runs and Determination of the Structure Function F_L* Prepared for 18th International Workshop on Deep Inelastic Scattering and Related Subjects (DIS 2010), Florence, Italy, 19-23 Apr 2010.
- [69] I. Abt et al. (H1 Collaboration), *The H1 detector at HERA*, Nucl. Instrum. Meth. **A386** (1997), 310.

- [70] J. Burger et al., *The Central jet chamber of the H1 experiment*, Nucl. Instrum. Meth. **A279** (1989), 217.
- [71] A. Aktas et al. (H1 Collaboration), *Tests of QCD factorisation in the diffractive production of dijets in deep-inelastic scattering and photoproduction at HERA*, Eur. Phys. J. **C51** (2007), 549, [hep-ex/0703022](#).
- [72] D. Pitzl et al., *The H1 silicon vertex detector*, Nucl. Instrum. Meth. **A454** (2000), 334, [hep-ex/0002044](#).
- [73] M. C. Urban, *The new CIP2k z-vertex trigger for the H1 experiment at HERA* (2004), DESY-THESIS-2004-044.
- [74] M. Cuje et al., *H1 High Luminosity Upgrade 2000 CIP and Level 1 vertex Trigger* (1998), h1-0198-535 (H1 Internal Note).
- [75] V. Blobel, *New developments in track finding and fitting* (2005), [Talk given at the Tracking Group Meeting](#).
- [76] B. Andrieu et al. (H1 Calorimeter Group Collaboration), *The H1 liquid argon calorimeter system*, Nucl. Instrum. Meth. **A336** (1993), 460.
- [77] B. Andrieu et al. (H1 Calorimeter Group Collaboration), *Results from pion calibration runs for the H1 liquid argon calorimeter and comparisons with simulations*, Nucl. Instrum. Meth. **A336** (1993), 499.
- [78] R. D. Appuhn et al. (H1 SPACAL Group Collaboration), *The H1 lead/scintillating-fibre calorimeter*, Nucl. Instrum. Meth. **A386** (1997), 397.
- [79] H. Collaboration (H1 Collaboration), *Proceedings to the 28th International Conference on High Energy Physics*, paper pa17-026 (1996).
- [80] H. Bethe and W. Heitler, *On the Stopping of Fast Particles and on the Creation of Positive Electrons*, Proc. Roy. Soc. Lond. **A146** (1934), 83.
- [81] R. A. Eichler, *Triggering With Short Bunch Distances: The H1 Trigger at HERA as an Example* Invited talk given at 5th Int. Conf. on Instrumentation for Colliding Beam Physics, Novosibirsk, USSR, Mar 15-21, 1990.
- [82] E. Elsen, *Aspects of the H1 trigger and data acquisition system* Prepared for 2nd Annual Conference on Electronics for Future Colliders, Chestnut Ridge, N.Y., 19-21 May 1992.
- [83] J. Naumann, *Development and testing of the third level trigger for H1. (In German)* DESY-THESIS-2003-009.

- [84] J. K. Köhne et al., *Realization of a second level neural network trigger for the H1 experiment at HERA*, Nucl. Instrum. Meth. **A389** (1997), 128.
- [85] P. Uelkes, *A Topological trigger for the H1 detector. (In German)* Aachen Tech. Hochsch. - PITHA-93-21 (93/06,rec.Aug.) 101 p.
- [86] A. Schöning (H1 Collaboration), *The Fast Track Trigger at the H1 experiment design concepts and algorithms*, Nucl. Instrum. Meth. **A566** (2006), 130.
- [87] A. Dubak, *Jet trigger in the H1 experiment at HERA*, AIP Conf. Proc. **899** (2007), 573.
- [88] K. Krastev, *Multijets in photoproduction at HERA* DESY-THESIS-2008-038.
- [89] N. E. Berger, *Measurement of diffractive phi meson photoproduction at HERA with the H1 fast track trigger* DISS-ETH-17169.
- [90] Y. H. Fleming, *The H1 first level fast track trigger* DESY-THESIS-2003-045.
- [91] A. Jung, *Measurement of D^* Mesons Cross Section and Extraction of the Charm Contribution, $F_2^c(x, Q^2)$, to the Proton Structure in Deep Inelastic ep Scatterubg with the H1 Detector at HERA* DESY-THESIS-2009-001.
- [92] C. Wissing, *Development of a simulation program and implementation of fast track fit algorithms for the new H1 drift chamber trigger. (In German)* DESY-THESIS-2003-003.
- [93] C. Amsler et al. (Particle Data Group Collaboration), *Review of particle physics*, Phys. Lett. **B667** (2008), 1.
- [94] G. J. Feldman et al., *Observation of the Decay $D^{*+} \rightarrow D0 \pi^+$* , Phys. Rev. Lett. **38** (1977), 1313.
- [95] K. Urban, *Measurement of Inclusive and DiJet D^* Meson Photoproduction at the H1 Experiment at HERA* DESY-THESIS-2009-010.
- [96] M.-O. Boenig, *Messung des D^* Meson-Produktions-querschnitts in gtiefinelastischer Streuung mit dem H1-Experiment* DESY-THESIS-2007-457.
- [97] J. Gaiser, *Charmonium Spectroscopy from Radiative Decays of the J/Ψ and Ψ'^** SLAC-0255.
- [98] W. Verkerke and D. Kirkby, *The RooFit toolkit for data modeling* (2003), [physics/0306116](#).

- [99] R. Brun, F. Rademakers, and S. Panacek, *ROOT, an object oriented data analysis framework* Prepared for CERN School of Computing (CSC 2000), Marathon, Greece, 17-30 Sep 2000.
- [100] R. Kogler et al. (H1 Collaboration), *The H1 OO Analysis Project* (2007), [Reference manual](#).
- [101] F. Jacquet and A. Blondel, *Proceedings of the Study of an ep facility for Europe*, DESY 79/48 (1979).
- [102] M. Peez. et al., *An Energy Flow Algorithm for Hadronic Reconstruction In OO: Hadroo2* (2005), h1-0105-616 (H1 Internal Note).
- [103] S. Osman, *Multiple parton interactions in deep inelastic ep- scattering at HERA* DESY-THESIS-2008-048.
- [104] M. Cacciari and G. P. Salam, *Dispelling the N^3 myth for the k_t jet-finder*, Phys. Lett. **B641** (2006), 57, [hep-ph/0512210](#).
- [105] G. Cowan, *Statistical data analysis* Oxford, UK: Clarendon (1998) 197 p.
- [106] S. Egli et al., *Calculating Event Weights in Case of Downscaling on Trigger Levels 1-4* (1997), h1-0497-517 (H1 Internal Note).
- [107] K. Urban, *Studies on a trigger for the measurement of the proton structure function F_2 at H1. (In German)* .
- [108] A. W. Jung (H1 Collaboration), *D^{+-} meson production in DIS and photoproduction with the H1 detector at HERA* Prepared for 16th International Workshop on Deep Inelastic Scattering and Related Subjects (DIS 2008), London, England, 7-11 Apr 2008.
- [109] V. Boudry et al., *The Inclusive Electron Trigger for the SpaCal: Design and CERN-test results* (1995), h1-0395-430 (H1 Internal Note).
- [110] E. Hennekemper, *Status Report* (2010), [Talk given at the Heavy Flavour Working Group](#).
- [111] R. M. Weber, *Diffractional ρ^0 photoproduction at HERA* DISS-ETH-16709.
- [112] M. Brinkmann, *Measurement of the D^{*+-} meson production cross section and $F_{c\bar{c}}^2$, at high Q^2 , in $e p$ scattering at HERA* DESY-THESIS-2010-016.
- [113] F. D. Aaron et al. (H1 Collaboration), *Measurement of D^* Meson Production and Determination of F_2^c at low Q^2 in Deep-Inelastic Scattering at HERA* To be published in 2010.

Acknowledgements

This work would have not been possible without the help and support of many. With the risk to miss someone I will try express my gratitude to the most significant contributions:

I am very grateful to Carsten Niebuhr for the opportunity to work at DESY and for his care and support during all those years. For the financial support in the last months of the work, the first to introduce me to H1, Dr. Daniel Pitzl, Dr. Max Klein and Dr. Ivan Tsakov and Prof. Yordan Stamenov from the Bulgarian Academy of Science.

To my supervisor Dr. Hannes Jung for his entire support, his nearly twenty four hours help, his emotional support, his trust in me, his patience, his professional knowledge in experimental and theoretical physics. For him being the greatest supervisor I can imagine. A million Thank you, Hannes!!!

To Prof. Joachim Meyer, reading the draft of the thesis and giving very useful advices and comments.

To my colleagues in the heavy flavour working group: Karin Daum for her excellent and sharp answers. Katja Krueger for her super clear way to explain the secrets of triggering, reconstruction and all these. To Peter Truoel and Mira Kraemer who were the referees of the measurement. To my colleagues Andreas Jung, Klaus Urban and Eva Hennekemper for their help, cross checks, discussions. Specially to Andy without whose help the trigger efficiency studies would have been impossible.

To Tobias Toll for providing the MC@NLO calculations. To Kaloyan Krastev for helping me start the analysis chain and his immense help concerning programing. To Dave South for his help improving my English. To Mira Kraemer for her help in almost everything during the writing period.

To my office mates for the friendly environment: Tobias Toll, Axel Cholewa, Lluís Martí, Nina Loktionova, Mira Kraemer and Pavel Belov.

To many other colleagues for discussions, advices, solutions: Sasha Glazov, Tim Namsoo, Voica Radescu, Roman Kogler, Guenter Grindhammer, Joerg Geyley, Stefan Schmitt, Alberto Martínez de la Ossa.

To all the people in the Physics and Cookies seminar.

To my dear family who have always been supporting me: my parents Dima and Georgi for raising me, educating me, trusting me, loving me... for everything! To my brother Lazar, his wife Margarita and my little niece Vihra for being always there for me and being my best friends!!! To my grand parents Lazar, Maria, Dimo and Zlatka, for giving me faith in the human beings in a long term. To all my cousins, aunts and uncles. I do have you all in my thoughts!

To my friends here, there and everywhere, before, now and forever for sharing: MUSIC, DANCES, LOVE, TEARS, LAUGHTER and SUN!!!

yours, Zlatka!!!